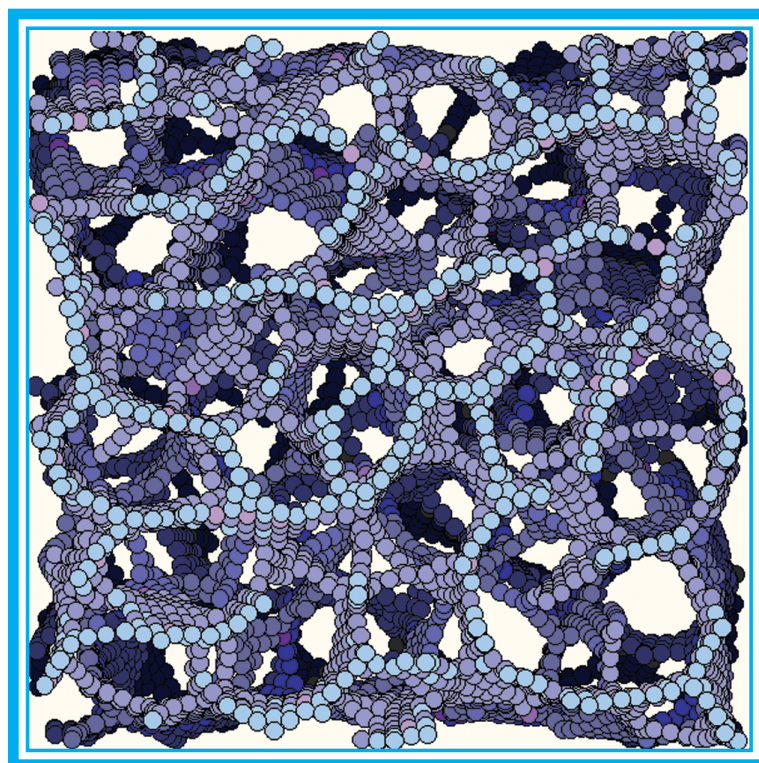# Physical and Chemical Sciences Center

Research Briefs

2002

Sandia National Laboratories
Albuquerque, New Mexico

A Department of Energy Multiprogram Laboratory

Cover Page: Simulation of a particle composite synthesized in a triaxial field during polymer gelation. The particles form roughly randomly oriented sheets. See Fig. 1 (upper right) on page 65.

Message from the Director

The Physical and Chemical Sciences Center provides new scientific knowledge in support of Sandia's mission areas–nuclear weapons, energy and critical infrastructure, nonproliferation and materials control, and emerging threats. We provide science-based solutions for the mission needs of our parent agency, the National Nuclear Security Administration (NNSA), particularly in areas where we have unique expertise. Of equal importance, we also perform focused long-term research in areas that are most likely to have impact on future Sandia missions and national security, particularly in the physical, chemical, and biological sciences that will enable future microsystems. To this end, we focus on five technical thrusts: optical sciences, nanosciences, compound semiconductors, biotechnology, and collective hierarchical systems. This volume reports on representative research in all of these areas of emphasis.

The activities of the Physical and Chemical Sciences Center are supported by a diverse set of funding sources that reflect the broad impact of our work, both scientifically and programmatically. The research described in this volume illustrates the importance of a strong science base in the physical and chemical sciences for the success of the Department of Energy's various missions. Throughout this work, we have benefited immeasurably from our partnerships with colleagues across the labs, in universities, and in industry. We gratefully acknowledge their collaboration.

We appreciate your interest in our work and welcome your comments and inquiries.

Julia M. Phillips
Director

Table of Contents

Table of Contents

Table of Contents

Table of Contents

Table of Contents

Table of Contents

Science-Based Solutions for NNSA Mission Needs

High Linear Energy Transfer (LET) Single Event Update (SEU) Testing Using the Ion Beam Materials Research Lab (IBMRL) RFQ-Van de Graaff System

by G .Vizkelethy, F. D. McDaniel, B. L. Doyle, P. Rossi, and P. E. Dodd

Motivation—Single Event Upsets (SEUs) caused by high energy cosmic radiation present a serious problem in satellites and other spacecraft. The same problem can affect weapons systems, as well. As more radiation hardened electronics are developed, higher Linear Energy Transfer (LET) ion beams are needed for the tests. The Ion Beam Materials Research Lab (IBMRL) took an active role in testing the SNL-developed radiation hardened Integrated Circuits (ICs) and helped to discover weaknesses of these parts in the design phase, thereby saving hundreds of thousand of dollars and many staff hours. The hardness of these ICs has now reached a level where the charge deposition density or LET of ions provided by our tandem Van de Graaff accelerator is not enough to cause upsets. An alternative is to go to the Brookhaven SEU facility where higher LET ions can be produced. In order to realize an SNL high LET system and to do high LET Radiation Effects Microscopy (REM), we employed a Radiofrequency Quadroupole (RFQ) Linear Accelerator (LINAC) as a booster on our Van de Graaff. This combined system can provide the highest LET beams and thereby the most ionizing form of radiation in Nature.

Accomplishment—RFQs are usually used as injectors for large accelerators such as the particle colliders at Fermilab, GSI, and CERN. Our unconventional approach used the tandem Van de Graaff accelerator as an injector for the two stage RFQ system. The ions are injected at 0.25 MeV/amu energy into the RFQ system. The first stage of the RFQ accelerates the ions to 1.3 MeV/amu; the second stage accelerates them to the final 1.9 MeV/amu, which is 374 MeV for gold ions. Since these Au ions are near their maximum electronic stopping power, they have nearly the highest possible LET. Since this RFQ system is designed for ions with $m/q < 8$, we installed a stripper foil just before the RFQ entrance aperture. Figure 1 shows the m/q vs. cavity field for various ion species. From this we see that the high charge states required for heavy ions cannot be produced by the tandem accelerator. The RFQ operates in pulsed mode, producing 50 μs pulses at 100 Hz repetition rate. This is a unique system; some of its operational characteristics were new even for the manufacturer of the RFQ. Recently we produced several ions with 1.9 MeV/amu, among them [65]Cu, [127]I and [197]Au with energies of 123, 241 and 374 MeV, respectively. These ions were used to SEU test the SNL TA788 CMOS6r SRAM and some of the first CMOS7-SOI memory chips manufactured in the Microelectronics Development Laboratory (MDL). Figure 2 shows the measured SEU cross sections for the TA788 chip. One-half of the memory on this chip is radiation soft; the other half is radiation hard. The SEU cross sections measured by the new SNL Tandem-RFQ agree well with the Brookhaven measurements.

Significance—It is important to carry out SEU tests in the design phase of radhard ICs to minimize development time. SNL designers will now be able to conduct quick SEU tests on prototype ICs locally at SNL using the Tandem-RFQ system. Furthermore, the Ion Electron Emission Microscope (IEEM) is currently being connected to the RFQ to perform high LET radiation effects microscopy (REM) of new ICs.
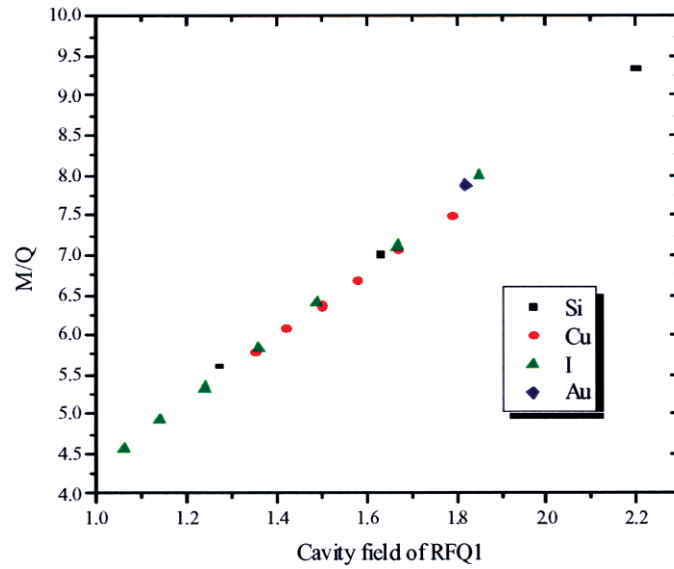
Figure 1. *m/q* (mass to charge) vs. cavity field (proportional to RFQ vane tip voltages) for Si^{+5}-Si^{+7}, Cu^{+12}-Cu^{+19}, I^{+17}-I^{+20}, and Au^{+25} ions accelerated by the tandem accelerator and RFQ1. The high charge states of these ions (required for the RFQ) were achieved by using a stripper foil. The resonance in beam transmission observed as a function of cavity field was not expected.
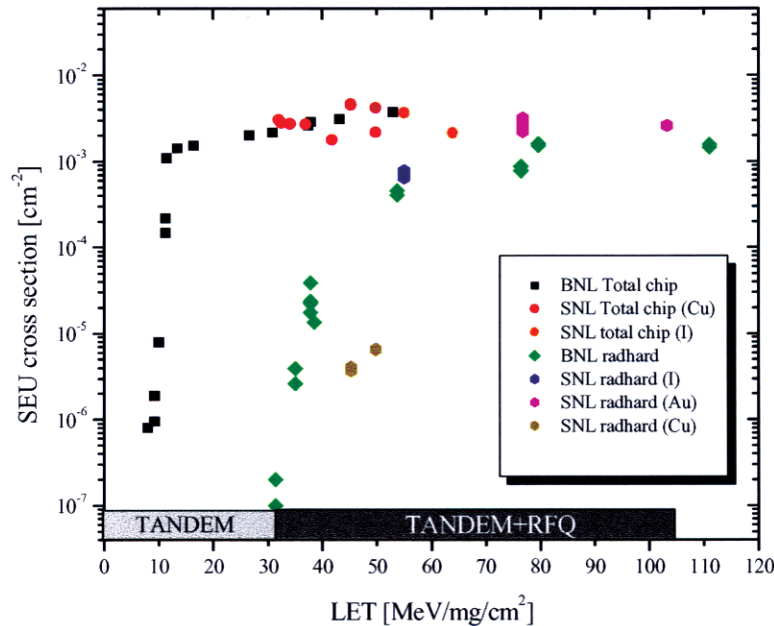
Figure 2. SEU cross-section of TA788 measured at BNL and SNL (ion species used in SNL tests are indicated in parentheses). Such data are collected by exposing an IC such as this SRAM to a known fluence (Φ) of ions and using an IC tester to determine the number (N) of upsets which result. The cross section is then just N/Φ. Good agreement between the SNL and BNL results were obtained except at the LET threshold for the radhard memory field, which could have resulted from manufacturing variability of the parts.

Temperature Effects in the Shock Response of PZT 95/5 and ALOX Encapsulant

by R. E. Setchell, M. U. Anderson, and D. E. Cox

Motivation—Shock-induced depoling of the ferroelectric ceramic PZT 95/5 is utilized in pulsed power devices. Ceramic elements are encapsulated in an alumina-filled epoxy (ALOX), and shock waves are generated through the detonation of a small explosive charge adjacent to the assembly. The actual stress-strain history experienced at any point in a PZT 95/5 element depends on the shock properties of both the ceramic and the encapsulant, and on the shock interactions that occur on their boundaries. These devices are typically required to operate over a broad temperature range. In practice, outputs at the highest initial temperature are significantly reduced compared to outputs at the lowest temperature. This temperature sensitivity dictates that devices be designed to meet minimum output requirements during high-temperature operation, resulting in excess performance at lower temperatures. More design flexibility and improved design margins could possibly result from new insights into the source of the temperature sensitivity.

Accomplishment—In recent years we have added the capability for conducting gas gun experiments over the full temperature range of interest for Sandia applications. Initial experiments at non-ambient conditions were conducted on unfilled epoxy samples to examine temperature dependencies in their viscoelastic behavior. More recently, we have utilized this capability to independently examine temperature effects in both poled PZT 95/5 samples and in ALOX samples. VISAR measurements of transmitted waveforms were made in all experiments, and currents generated from shock-induced depoling into a short-circuit load were measured in the PZT 95/5 experiments. Figure 1 shows currents measured during the transit of 2.6 GPa shocks in samples at 75, 20, and −60 °C. The individual current levels will differ slightly due to differences in remanent polarizations, but the high-temperature case is still somewhat low. The most noticeable feature is the extended rise and fall times for the high-temperature experiment, which was found to be repeatable in a subsequent, identical experiment. At this temperature the PZT likely starts from a different FE phase (F_{R2} instead of F_{R1}), and may pass through multiple phase boundaries during shock compression. Under these circumstances, the phase transition kinetics may be slower than in the other cases. Corresponding transmitted waveforms do not show significant differences. Figure 2 shows transmitted waveforms and the arrival of release waves in ALOX samples at different initial temperatures. Wave rise times increase markedly with decreasing temperature in this highly dispersive material, while corresponding release wave velocities decrease. The high ALOX release speed at elevated temperatures could result in lower shock pressures in PZT 95/5 elements during power supply operation.

Significance—Our experiments are identifying how changes in initial temperature alter the shock wave behavior of PZT 95/5 and ALOX independently. The only apparent effect in PZT 95/5 may be associated with different phase transition kinetics at the highest temperature. ALOX, however, shows a continuous change in mechanical constitutive properties with temperature. The results to date suggest that the temperature sensitivity in pulsed power devices is primarily due to the ALOX encapsulant, although additional studies are certainly needed.
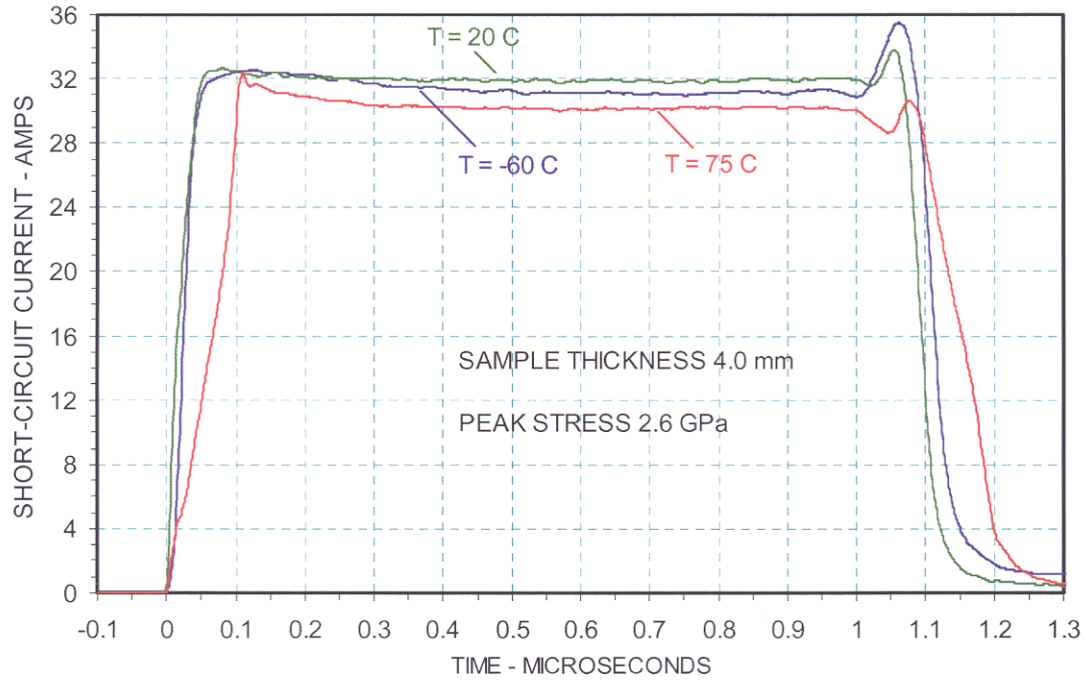
Figure 1. Short-circuit currents generated by 2.6 GPa shocks propagating through normally poled PZT 95/5 samples at different initial temperatures.
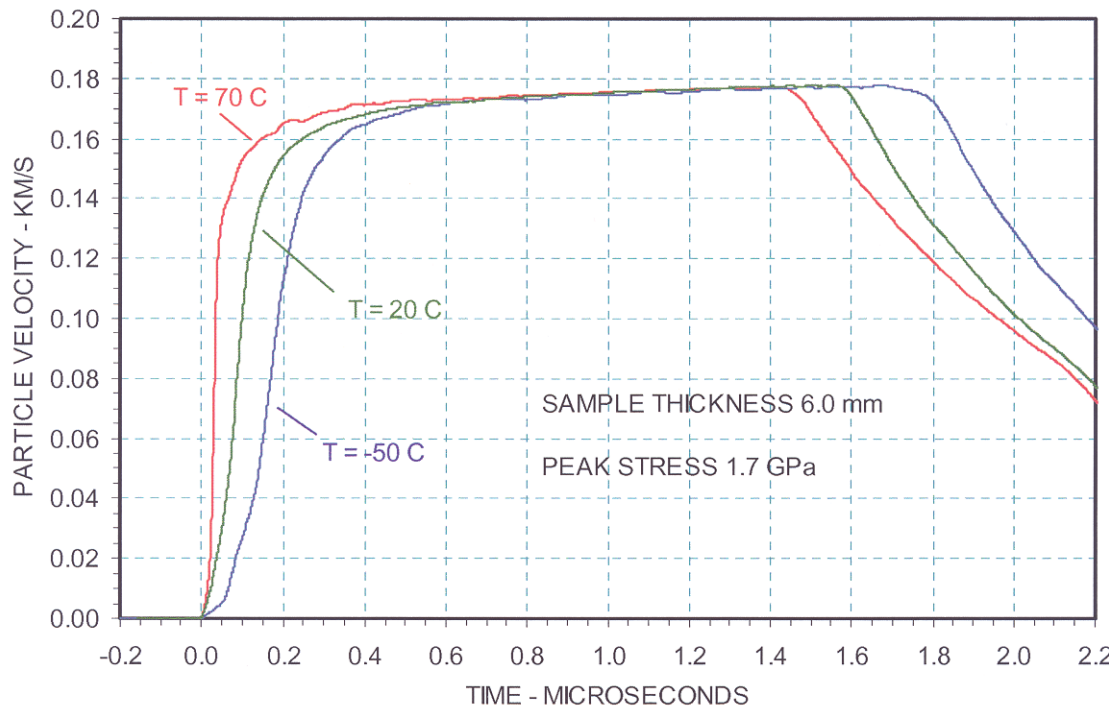
Figure 2. VISAR-measured particle velocity profiles of 1.7 GPa transmitted waves in ALOX samples at different initial densities. Differences in release-wave arrival times correspond to release speeds decreasing with decreasing temperature.

Optical Sciences

RISTRA: A Rotated Image, Singly Resonant, Twisted Rectangle, Optical Parametric Oscillator

by A. V. Smith and D. J. Armstrong

Motivation—Optical parametric oscillators (OPOs) provide a means of shifting wavelengths of lasers from wavelengths that are convenient for good laser performance to wavelengths that are desired for applications. The challenges are to achieve good spatial coherence, or beam quality, good temporal coherence, or bandwidth, and good conversion efficiency. These goals are especially elusive for high-energy nanosecond lasers and OPOs.

Accomplishment—OPOs use the nonlinear response of transparent crystals to split a laser (pump) photon into two lower energy photons (signal and idler). Although the photon energies of the signal and idler must sum to that of the pump, their energies are determined by the characteristics of the crystal, providing the potential for broad tunability. The photon splitting process yields gain at the signal and idler wavelengths, so feedback of one of these beams can lead to optical parametric oscillation.

Based on extensive numerical modeling of nanosecond OPOs, we developed a set of criteria for optimizing various OPO properties. In particular we showed that rotating the image of the resonating beam by 90° on each round trip of the optical cavity provides good beam quality, even for large diameter beams where beam quality usually is exceptionally poor. Several mechanisms contribute to this improvement. The most important is birefringent walk-off between the signal and idler beams inside the crystal, a mechanism normally considered detrimental, that we have harnessed to improve beam quality. A second mechanism is averaging over spatial variations in the pump beam, which allows the signal beam quality to surpass that of the pump beam. A third mechanism is mirror alignment stability. An image-rotating cavity has a unique optical axis. If one of the mirrors is slightly perturbed this axis shifts a small amount, but there is still a unique axis. The signal beam follows this axis, in sharp contrast to non-rotating cavities where a similar mirror perturbation completely misaligns the cavity, suppressing oscillation or strongly distorting the signal beam.

Many image-rotating cavity designs are possible, but we have invented one that we think is ideal for OPOs. It is based on four planar mirrors arranged as shown in Fig. 1. Its primary attractions are short cavity length, large beam diameters, and convenient polarization control using a half-wave plate. We demonstrated excellent beam quality and good conversion efficiency from an OPO of this design. Based on these results we engineered the monolithic version shown in Fig. 2. Because of the inherent alignment stability, the mirrors are fastened directly to the machined cylindrical body. The result is a mechanically robust, vibration resistant, easy to use cavity. We think this OPO will prove valuable to Sandia's remote sensing program and in meeting NASA's requirements for a full-earth ozone mapping LIDAR satellite.

Significance—Our new OPO design can simultaneously improve beam quality, efficiency, and bandwidth of nanosecond OPO's. This will make it possible to further expand the tuning range using additional nonlinear optical stages. It should benefit Sandia's and NASA's remote sensing programs, and it will improve laser sources available for many other applications.
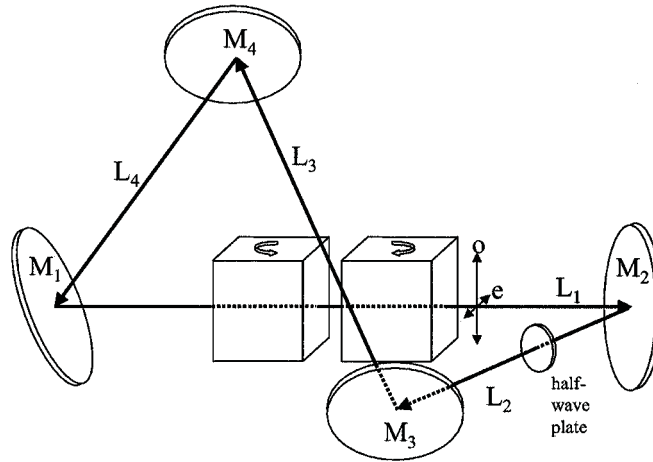
Figure 1. RISTRA cavity comprising four planar mirrors, M1-M4, nonlinear crystals, and a half-wave plate to control the polarization direction. The pump beam enters through M_1 and exits through M_2. The idler is transmitted by each mirror while the signal is totally reflected by all mirrors except the output coupler, M_2, which partially transmits it. Nonlinear crystals can go in leg L_1 or L_3 or both.

Figure 2. One-crystal version of the RISTRA OPO showing beam paths in light blue, and a pico-motor to rotate the crystal in red. The flat plate on top covers a second crystal bay in leg L_3 that is used for two-crystal versions.

Efficient Algorithm for Region of Influence and VERI Clustering

by J. W. Bartholomew and G . C. Osbourn

Motivation—Clustering determines (or imposes) an order, based on some measure of similarity, on a data set. The resulting clusters can be used for pattern recognition of new data points. Our Visual Empirical Region of Influence (VERI) clustering algorithm uses a Region of Influence (ROI)–determined empirically from human visual perception studies–to determine if each pair of data points groups. The resulting connected graphs form the clusters in the data set.

The current $O(n^2)$ algorithm was practical for modest data set sizes (~10^5). To handle larger data mining problems (>10^6), two approaches to reduce the runtime were proposed: 1) reduce the current $O(n^2)$ algorithm to $O(n \log n)$, and 2) implement a parallel version of the algorithm. The first approach has been achieved and is described here.

Accomplishment—We have developed an algorithm for computing the VERI graph, and graphs for a related class of ROIs, in $O(n \log n)$ time for arbitrary dimensionality. The method is based both on a combination of a particular version of the Well-Separated Pair Decomposition (WSPD) data structure proposed in Paul B. Callahan's PhD thesis, and a previous $O(n^2)$ VERI algorithm developed by the authors. Experimental results from artificial and chemical sensor array data show that the algorithm is efficient for the modest dimensionalities that are useful for VERI pattern recognition. Storage requirements are practical, as well. We further find that the proven asymptotic $O(n \log n)$ behavior at larger dimensionalities only occurs for n that is much larger than practically achievable. In this regime of high dimensionality (d >10), the experimental runtimes are generally rapidly increasing functions of d and n and are less favorable. This is consistent with other experimental studies of the failure to achieve $O(n \log n)$ computation of the WSPD data structure itself at large d, and is a natural

consequence of the so-called "curse of dimensionality". Euclidean distance measures tend to become ineffective at large d, and the ROI/VERI graphs also generally degenerate in this regime, i.e., all points tend to have edges with all others. This is also the reason that VERI feature set optimization tends to produce the best results using a modestly sized subset from feature sets of arbitrary size. Thus, we find that the limitation of $O(n \log n)$ asymptotic behavior to data sets of modest d is not a serious issue for practical VERI problems since the VERI pattern recognition technique itself is most effective using feature subsets in this same d regime.

Figure 1 shows a comparison of the runtimes of the previous $O(n^2)$ VERI algorithm with the new $O(n \log n)$ VERI algorithm based on WSPD for uniformly random artificial data with d = 3. The results were obtained from a 2.0GHz Pentium IV PC running Linux 7.2. A data set of 10^7 points (d = 3) can now be processed in 40 <u>minutes</u> vs. 116 <u>days</u> for the previous algorithm.

A simple post-processing of the algorithm's clustering results produced the leave-one-out algorithm used for feature optimization, with little impact on the run time. Developing a method of discriminating new data points and producing parallel implementations of the algorithms are the next steps in supporting the goal of handling large data mining problems.

Significance—This breakthrough paves the way for applying VERI to a host of massive data mining problems such as results from Accelerated Strategic Computing Initiative (ASCI) simulations in support of the Stockpile Stewardship Program (SSP) for the National Nuclear Security Administration (NNSA). The WSPD has efficient parallel implementations – work has begun on implementing a parallel VERI algorithm based on them.
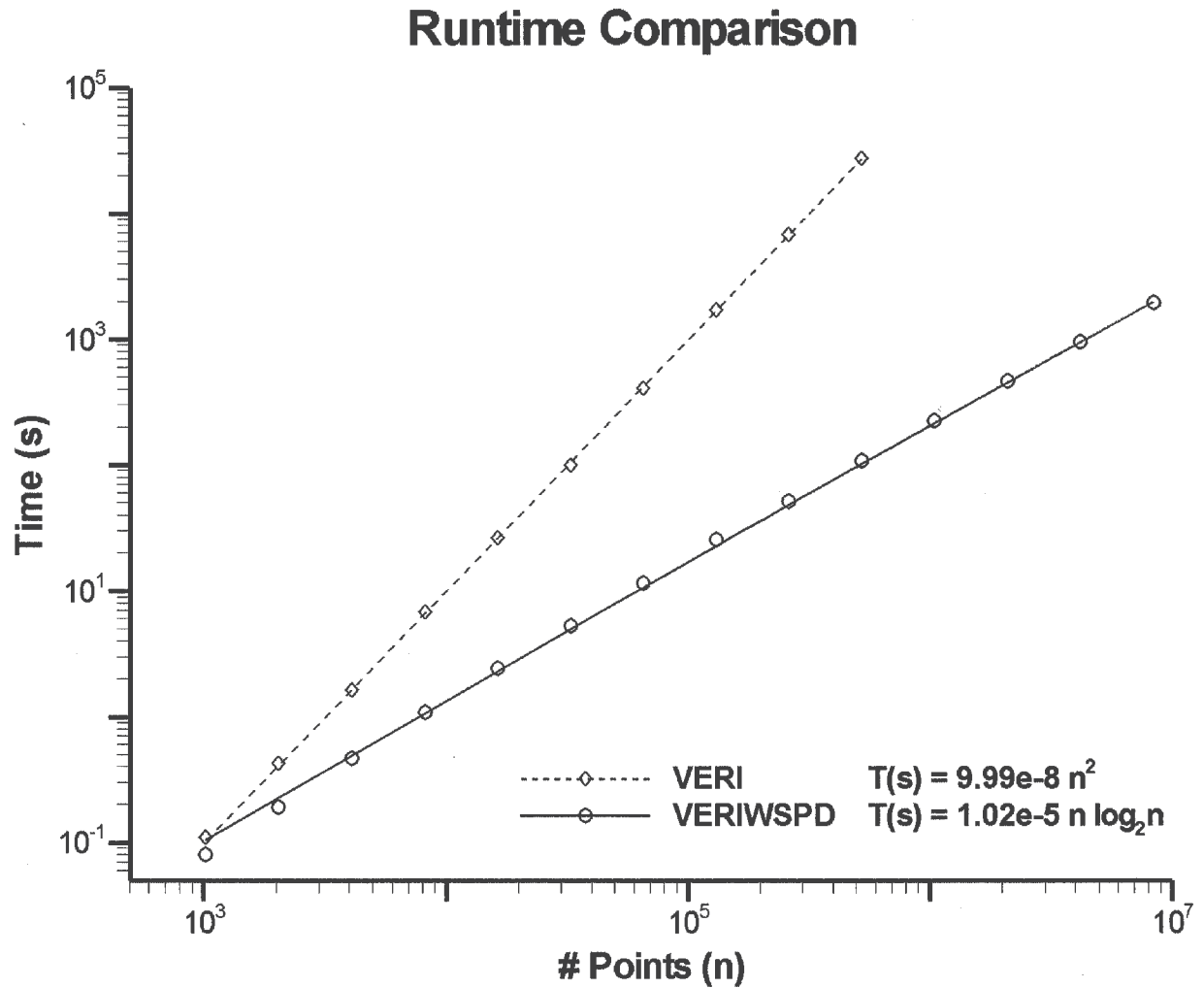
Figure 1. Comparison of the runtimes of the previous $O(n^2)$ VERI algorithm (dashed line) with the new $O(n\ log\ n)$ VERI algorithm based on WSPD for uniformly random artificial data (solid line) with $d = 3$. The results were obtained from a 2.0GHz Pentium IV PC running Linux 7.2.

Anomalous Carrier-induced Dispersion in Semiconductor Quantum Dots

by H. C. Schneider and W. W. Chow

Motivation—Improvements in sample quality are motivating more detailed investigations of the physics and applications of quantum-dot systems. It is now clear that the idealized 'atom-like' description used in early predictions of the benefits of quantum dots is not entirely accurate. Surprisingly, in some cases, the real quantum-dot system may be even more advantageous for laser operation. This is what was found in recent experimental and theoretical investigations on the dispersive properties of quantum-dot laser structures. The real part of the optical susceptibility, which determines the carrier-induced refractive index change δn, is important because it contributes to the fundamental laser linewidth, as well as to the noise properties and achievable single-mode power of quantum-dot lasers.

Accomplishment—Our calculations indicate that because of the Coulomb coupling between bound and continuum states, the dispersive behavior of a quantum-dot active medium differs in several important aspects from that expected from an 'atom-like' quantum-dot picture, as well as from that observed in bulk or quantum-well structures. Specifically, Coulomb renormalizations lead to a positive differential refractive index $\partial \delta n / \partial N$ and, consquently, a *negative* linewidth enhancement (or antiguiding) factor $\alpha \propto -\partial \delta n / \partial N [\partial g / \partial N]^{-1}$ at gain peak (see Fig. 1). Here, N is the carrier density and g is the gain. In contrast, the 'atom-like' picture predicts that δn spectra for different carrier densities cross at the gain peak, so that both the differential refractive index and α vanish there. For bulk and quantum well gain media, δn decreases with carrier density whenever gain is present, so that α is always positive.

Since direct measurement of the refractive index is very difficult, the theoretical predictions were verified indirectly by experimentally examining the filamentation tendency in quantum dot lasers. This narrowing of lateral beam filaments with increasing excitation in running semiconductor lasers is due to the focusing effect of the index guide introduced by a positive differential refractive index. The experiment was performed in the group of P. Smowton and P. Blood at Cardiff University, UK, using quantum dot lasers consisting of InGaAs quantum dots embedded in GaAs quantum well layers. To remove any complications due to thermally induced self focusing, the devices were operated pulsed. Figure 2 shows the near-field lateral intensity profile for currents from twice to eight times the threshold value. The curves show decreasing intensity variation, i.e., decreasing filamentation, with increasing excitation. The experimental result is consistently explained by our calculation on the basis of a negative α factor.

Significance—Our result shows that the anomaly in the dispersive behavior of a quantum dot structure eliminates the long-standing problem of beam-filamentation, which presently limits high-power single-mode operation in semiconductor lasers.
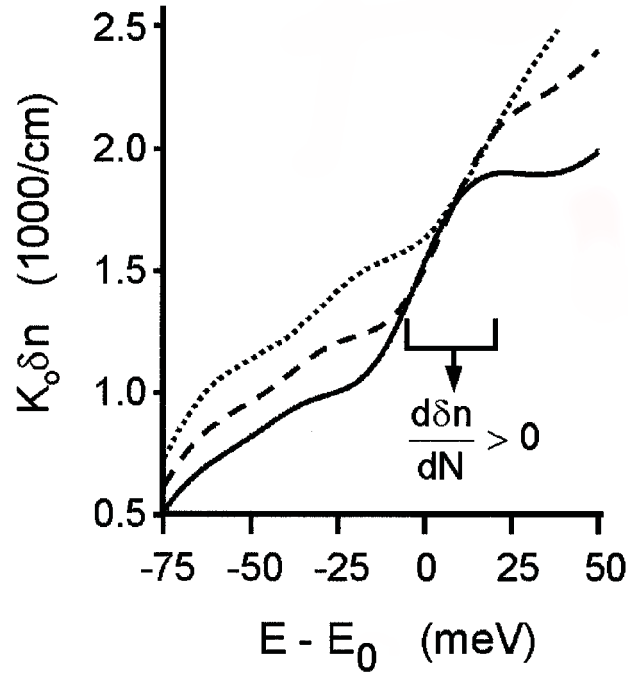
Figure 1. Carrier-induced refractive index change vs. energy for carrier densities 6 x 10″ cm^{-2} (dotted curve), 8 x 10″ cm^{-2} (dashed curve) and 10^{12} cm^{-2}. Gain is present within the energy range plotted. E_0 is the unexcited quantum dot ground-state resonance.
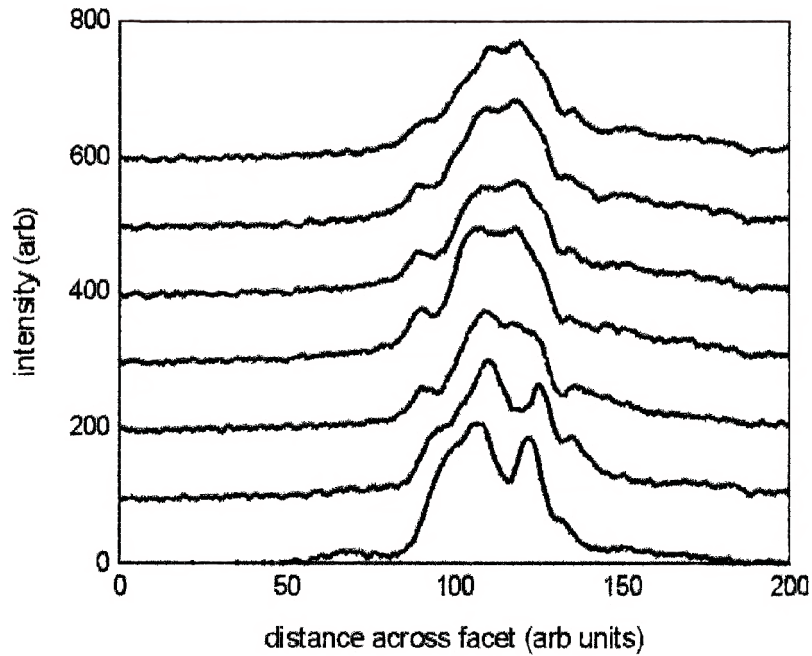
Figure 2. Linescan of intensity through the center of a near field image of an InGaAs quantum dot laser for increasing current density (300 to 1200 A cm^{-2}), showing the increase in filament width with increasing excitation, consistent with the prediction of a $\partial \delta n / \partial N$ positive region in Fig. 1.

Deep Ultra-Violet LEDs for Detection of Biological Agents

by A. J. Fischer, A. A. Allerman, D. D. Koleske, K. H. A. Bogart, K. W. Fullmer, J. J. Figiel

Motivation—Optical sources emitting in the wavelength range from 280-340 nm are essential as pump sources for fluorescence-based chemical and biological agent detection. In order to realize compact, portable, and low cost detection systems, the optical pump sources must be very small and have high optical efficiencies. Light emitting diodes (LEDs) and laser diodes based on GaN and related alloys of InGaN and AlGaN are the most promising candidates for deep ultraviolet optical emitters.

Accomplishment—Short wavelength LEDs are typically grown by metalorganic vapor phase epitaxy (MOVPE) on thick GaN layers. For LEDs emitting at wavelengths shorter than 370 nm, these GaN layers absorb a large fraction of the LED emission. In fact, more than half the light generated will be absorbed by a layer of GaN as thin as 0.5 μm. Therefore, the elimination of all absorbing GaN layers from an LED emitting in the deep UV is clearly beneficial since it allows for improved extraction of light from the LED chip.

We have fabricated an LED emitting at 320 nm which was grown without incorporating any absorbing GaN layers. As shown in Fig. 1, all epitaxial layers, except the quantum wells in the active region, are AlGaN with Al concentrations of 30% or greater which are transparent to the LED emission wavelength of 320 nm. The LED is grown using a low temperature AlN buffer layer deposited on sapphire followed by a 30 period n-type short-period-superlattice (SPSL) consisting of alternating 75 Å $Al_{0.35}Ga_{0.65}N$ wells and 25 Å $Al_{0.7}Ga_{0.3}N$ barriers. Next, a multiple quantum well active region was grown consisting of 3 periods of 10 Å $Al_{0.2}Ga_{0.8}N$ wells and 100 Å $Al_{0.8}Ga_{0.2}N$ barriers for emission at 320 nm followed by a 15 period

p-type SPSL grown with 50 Å $Al_{0.3}Ga_{0.7}N$ wells and 20 Å AlN barriers. The structure is completed by growing a second n-type SPSL identical to the first. The upper p-n junction functions as a reverse-biased, leaky junction and provides an effective method for injection of holes into the active region.

Devices were fabricated using standard lithographic techniques to define features. The n-p-n structure allowed for device fabrication using two n-type metal contacts which bypasses the issues associated with forming p-type Ohmic contacts to $Al_{0.3}Ga_{0.7}N$. Mesas were fabricated using inductively coupled plasma reactive-ion etching which exposed the lower n-type SPSL. Ti/Al contacts were then deposited by e-beam evaporation to form both the upper and lower n-type contacts.

The electroluminescence spectrum is shown in Fig. 2 (a) at room temperature for several different drive currents. The spectra show a sharp peak at 320 nm with a 15 nm full width at half maximum. Note that there is very little defect-related emission at long wavelengths which can interfere with detection of biological agents. Figure 2 (b) shows a room temperature light vs. current curve under DC current injection showing a peak output of 17.8 μW at 1.6 A/cm². With improvements in the low temperature AlN nucleation layer even higher output powers are expected.

Significance—AlGaN-based solid state LEDs and laser diodes are critical components that will be used in compact fluorescence-based biological detection systems. This research is a significant step forward towards our goal of realizing high brightness deep ultra-violet LEDs.
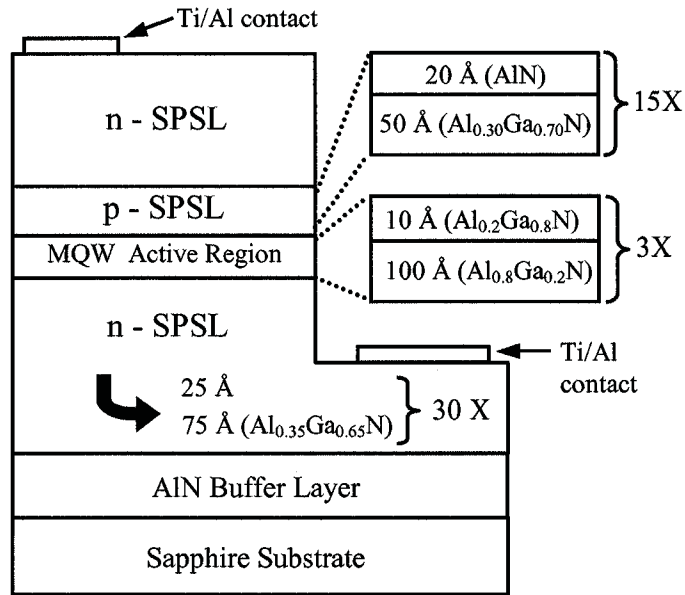
Figure 1. Schematic of n-p-n LED structure. Note that short period superlattices (SPSLs) were employed to enhance electrical conduction, and a reverse-biased, leaky p-n junction is used for hole injection.
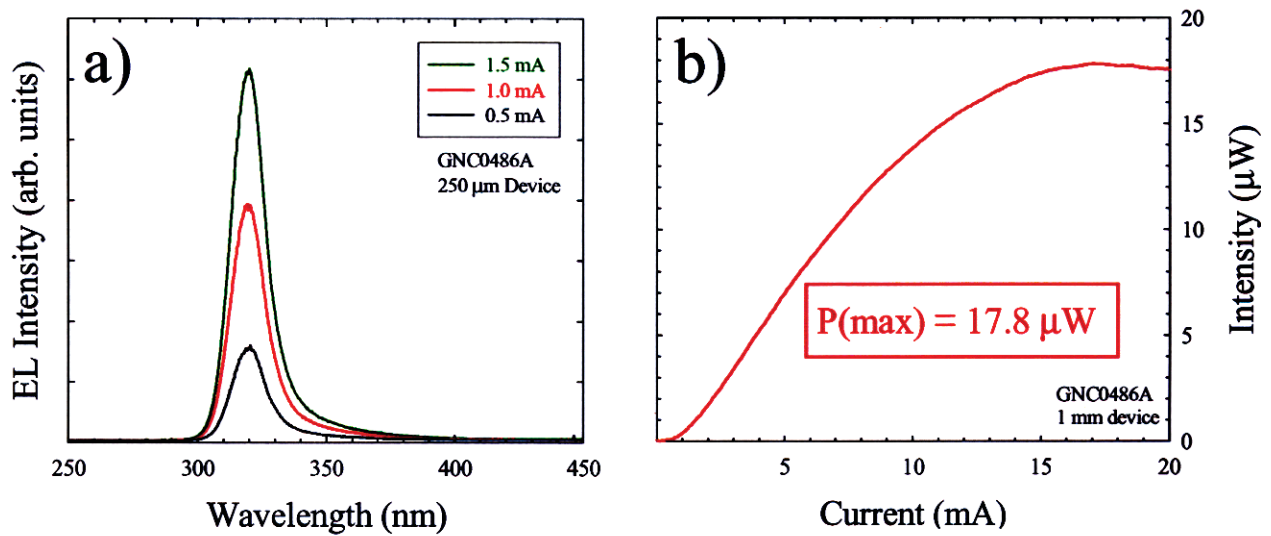
Figure 2. (a) Electroluminescence (EL) spectra at several current densities showing a single sharp peak at 320 nm. (b) Light vs. current curve at room temperature under DC operation showing a maximum of 17.8 μW of output power.

Wide Bandgap Compound Semiconductors

Cantilever Epitaxy of GaN: Further Reductions in Dislocations for Brighter LEDs

by D. M. Follstaedt, A. J. Fischer, C. C. Mitchell, D. D. Koleske, A. A. Allerman, N. A. Missert, P. P. Provencio, K. H. A. Bogart, J. J. Figiel, K. W. Fullmer, and C. I. H. Ashby

Motivation—Gallium nitride is an important semiconductor because of its wide bandgap and high-frequency and high-temperature properties. Optical emitters of GaN are being developed for portable detection of biotoxins and organic chemicals. Moreover, near-UV light-emitting diodes (LEDs) pumping phosphors have the potential to provide general illumination with 50% efficiency and reduce U.S. electricity use by 10%. Low-defect GaN is also needed for high electron mobility transistors and miniaturization of synthetic aperture radar in unmanned aircraft. The lack of a suitable substrate for epitaxial growth seriously limits applications of hexagonal GaN. Sapphire is often used, but its large lattice-mismatch (16%) leads to high areal densities of vertical threading dislocations (VTDs), 10^9-10^{10}VTD/cm^2. The VTDs directly reduce optical emission and scatter electrons, degrading device performances.

Accomplishment—To reduce VTDs, we developed cantilever epitaxy (CE), where GaN is first grown on mesas formed by etching trenches into sapphire followed by lateral growth over the trenches (see Research Briefs 2001, p.74). Mesa areas contain the usual VTD density while areas over trenches have much lower densities. CE is favored over other reduction methods because it requires only one growth sequence in the metal-organic chemical vapor deposition reactor. To reduce VTDs further, we have used narrow mesas along with a low-temperature growth step that forms a slanted facet on GaN over mesas early in the sequence, as in Fig. 1. This approach was predicted to turn VTDs from vertical to horizontal and away from device areas above. Recent improvements in etching sapphire have allowed this method to be implemented. Cross-section transmission electron microscopy (TEM) of GaN over the mesas shows that VTDs are turned to horizontal as expected; see Fig 1. The TEM results indicated that when the substrate etching and GaN growth steps are optimized to cover the entire mesa with facets, all VTDs can in principle be turned. This approach reduced the overall areal density to 5×10^7VTDs/cm^2.

In addition, we have developed a nucleation procedure for GaN on sapphire with inherently fewer VTDs. When combined with the facetting step, a very low overall dislocation density was found by plan-view TEM (Fig. 2), scanning cathodoluminescence, and atomic-force microscopy, 2–3×10^7VTDs/cm^2. Together, all our CE methods reduce VTD density by about two orders of magnitude compared to conventional planar growth of GaN on sapphire.

Significance—The low VTD density of CE-GaN makes it a superior substrate for light emitting devices. We have grown 390-nm LEDs on thick (>2 µm) Si-doped CE-GaN. The active region consisted of five 40 Å In$_{0.05}$Ga$_{0.95}$N quantum wells with GaN barriers. The LEDs were fabricated as top emitters using a semi-transparent p-contact. An initial device on CE-GaN had a power output of 1.3 mW at 20 mA, an improvement of 15 times over earlier LEDs on planar GaN. For this device, residual VTDs over mesas produced dark stripes in emission as shown in Fig. 3a. A recent LED made with improved nucleation shows uniform areas (no stripes) as in Fig. 3b. The large, darker areas are defects with lateral dislocation arrays that remain to be eliminated. Cantilever epitaxy shows promise for producing the efficient, bright LEDs needed for solid state lighting.
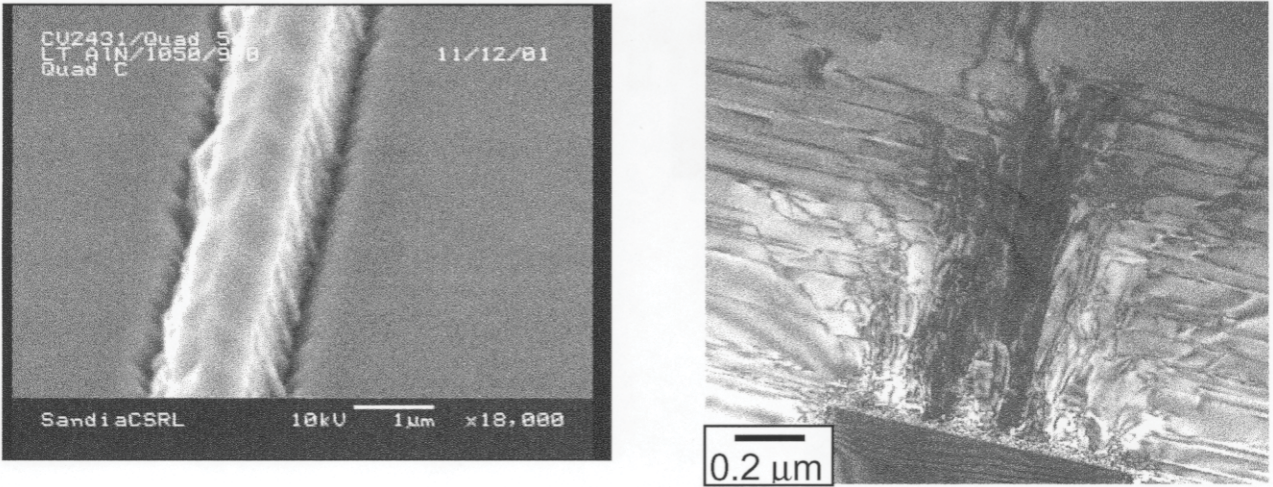
Figure 1. (Left) Scanning electron micrograph of facetted GaN over a mesa just after the low-temperature growth step. (Right) Cross-section TEM image showing that threading dislocations emerging from the mesa are turned to horizontal by the facet growth step.
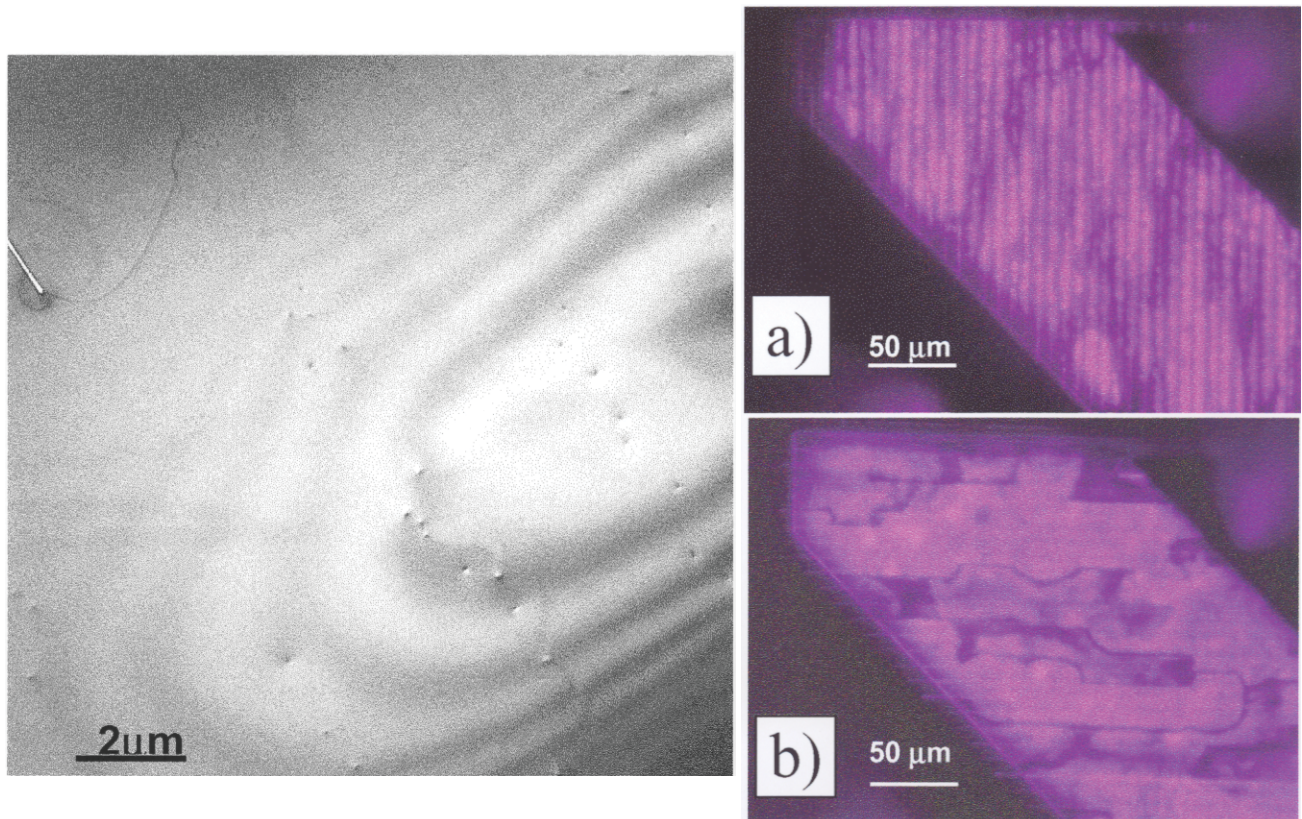
Figure 2. (Left) Plan-view TEM showing a low density of VTDs (spots) at the surface of CE-GaN grown with facetting and improved nucleation; an isolated lateral defect is also seen in the upper left. Overall density is 2-3x10^{7}VTDs/cm^2.

Figure 3. (Right) Electroluminescence from LEDs on CE-GaN. a) Initial LED with bright emission in cantilevers but dark vertical stripes from residual dislocations over mesas. b) Recent LED with improved uniformity in optimized areas, along with darker areas of lateral dislocation arrays.

Gas-phase Nanoparticle Formation during AlGaN MOCVD

by J. R. Creighton, M. E. Coltrin, W. G. Breiland, and R.P. Pawlowski

Motivation—GaN and AlGaN alloys are extremely important materials with widespread applications for optoelectronics (e.g., solid state lighting) and high power electronics. The AlGaN metalorganic chemical vapor phase deposition (MOCVD) process is often complicated by parasitic gas-phase chemical reactions that diminish the group-III deposition efficiency and make it difficult to control alloy composition. Growth rate and alloy composition are often a sensitive function of temperature and other reactor variables. Many chemical mechanisms have been proposed, usually initiated by the formation of adducts between the group-III metalorganic and ammonia, but a complete understanding of the critical reaction pathways has not yet been synthesized.

Accomplishment—Speculation that particle nucleation and growth was occurring in the thermal boundary layer led us to search for their presence using *in situ* laser light scattering. In order to improve the lateral optical access we constructed an inverted stagnation point flow reactor. A typical image of the particles formed during GaN MOCVD is shown in Fig. 1. Images of scattering from particles formed during AlN and AlGaN MOCVD are nearly identical. The overall lateral shape of the layer is very similar to an isotherm in the stagnation point flow configuration, suggesting that thermophoretic forces play a dominant role in determining the location of the particles. Along the centerline of the reactor, the layer of GaN particles is located 5.8 ± 0.2 mm from the heated surface and has a very narrow spatial distribution (FWHM ~ 0.2 mm). The particles should reside at the position at which the thermophoretic velocity (away from the heated surface) balances the bulk fluid velocity (toward the surface). The fluid dynamics of the inverted stagnation point flow reactor was calculated using the MPSalsa code. The calculated thermophoretic velocity is shown in Fig. 2, along with the calculated convective velocity. The theoretical particle position of 5.1 mm is in good agreement with the experimental result.

By measuring the angular dependence of the scattered light intensity we have extracted the particle diameter, and by calibrating the absolute scattered light intensity we have computed the particle number density. The measured scattering intensity for AlN particles is shown in Fig. 3. The solid curve in Fig. 3 is a fit from a Mie calculation, which yields a particle diameter of 48 nm. Results between 900-1020°C gave particle diameters from 35-50 nm, and particle number densities from 1-6 X 10^8 cm^{-3}. The fraction of input Al converted into nanoparticles was 0.2-0.8, which is the right magnitude needed to explain the decline in measured AlN growth rates at high temperatures. Detailed quantitative analysis of GaN particles was not possible because of their non-spherical shape, but their overall size and densities are in the same range as AlN particles.

Significance—The non-linear and non-ideal behavior of the AlGaN MOCVD has greatly impeded the growth and utilization of AlGaN material. We have now conclusively shown that gas-phase nanoparticles are formed during the MOCVD process, and that they represent the end product of the parasitic chemical processes responsible for the non-ideal behavior. The identification of this parasitic chemical mechanism will significantly aid in reactor design improvement and process optimization.
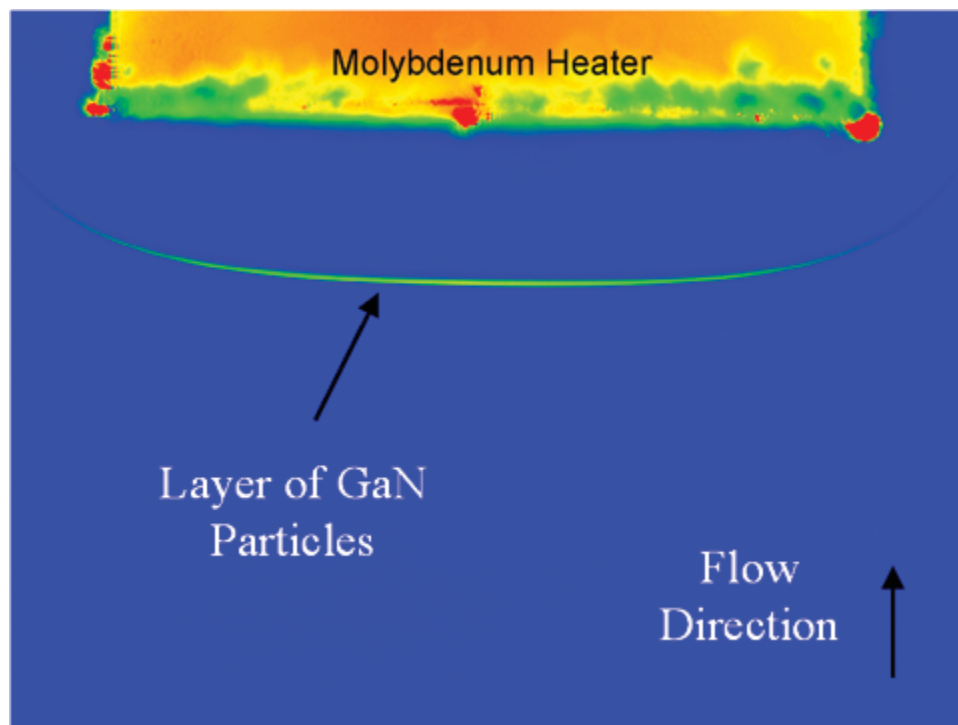
Figure 1. Laser illumination reveals a sharp layer of particles residing 5.8 mm from the heated surface during GaN MOCVD at 983°C, 140 Torr (inverted stagnation point flow geometry).
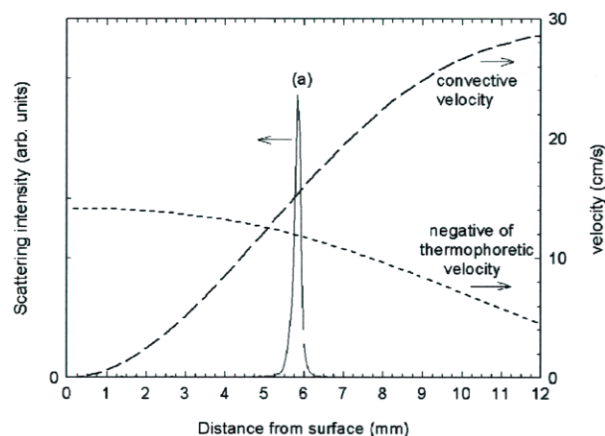
Figure 2. Scattering profile for GaN particles formed at 983°C, curve (a), along the centerline of the reactor, with the peak position at 5.8 mm. The calculated convective velocity and thermophoretic velocity sum to zero at 5.1 mm.
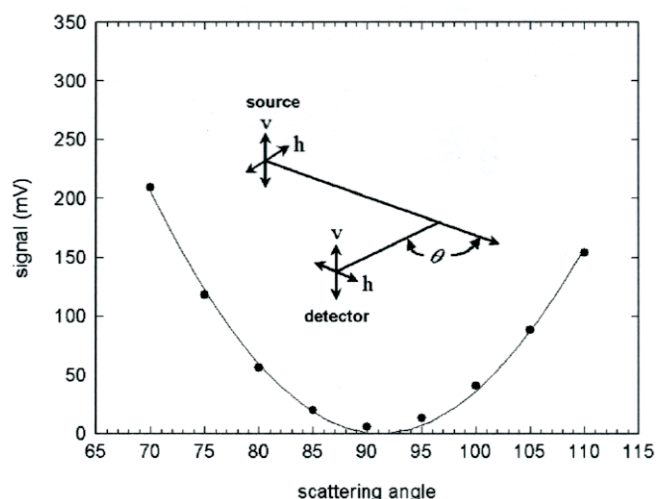
Figure 3. Measured scattering profile (circles) for AlN particles at 975°C using parallel polarization (hh). Solid line is the Mie theoretical fit for a particle diameter of 48 nm.

Optical Probes of the AlGaN/GaN Heterostructure and 2-Dimensional Electron Gas for High Power Electronics

by **Steven R. Kurtz**

Motivation—GaN-based electronics offer radical miniaturization of microwave power amplifier and radar circuitry. GaN's large bandgap, high breakdown field, high electron velocity, and excellent thermal properties have led to high electron mobility transistors (HEMT) with up to 10 times the power density of GaAs and other traditional semiconductors at frequencies up to 20 GHz.

Further contributing to the outstanding performance of GaN-based amplifiers is the highly conducting, 2-dimensional electron gas (2DEG) used for the HEMT channel. Intrinsic polarization and piezoelectric properties of GaN materials can produce a 2DEG at an AlGaN/GaN interface with a sheet carrier concentration of $10^{13}/cm^2$, well in excess of that achievable in any other III-V material system. The physics and material science of the AlGaN/GaN 2DEG are critical to the performance and future development of GaN-based electronics.

Accomplishment—Electronic properties of AlGaN/GaN heterostructures and field-effect transistors were determined using a contacted electroreflectance technique. This optical probe augments conventional electrical characterization of GaN-based field-effect transistors. By studying variations in the electroreflectance with applied electric field, spectral features associated with the AlGaN barrier, the 2DEG at the interface, and bulk GaN are clearly identified (see Fig. 1). The 2DEG produced a broad, first-derivative-like electroreflectance feature. With bias voltage, the 2DEG electroreflectance narrowed and converged with the GaN band-edge. The 2DEG Fermi energy was determined from

analysis of the line-shape. The AlGaN barrier displayed Franz-Keldysh oscillations which provided estimates of barrier-layer composition and electric field (see Fig. 2). The period of the Franz-Keldysh oscillations varied with bias voltage. Large discrepancies were observed between measured AlGaN barrier compositions and compositions projected from MOCVD growth calibrations. For heterostructures grown on sapphire, AlGaN electric fields determined from the Franz-Keldysh oscillations were anomalously larger than those predicted by AlGaN/GaN heterostructure models. Possible explanations for the large electric field values include electron trapping within the AlGaN barrier or an AlGaN composition gradient.

To further reduce dislocation densities, we have begun to evaluate alternative substrates to sapphire. Initial work has focused on the properties of the AlGaN/GaN devices grown on SiC substrates. Overall material quality and properties of the 2DEG are monitored with optical and electrical measurements. Comparing structures grown under different conditions, our optical measurements will test fundamental models of AlGaN/GaN heterostructure electronic properties.

Significance—An optical probe of AlGaN/GaN heterostructures and transistors augments conventional electrical characterization tools. This electroreflectance technique provides the first direct measurements of AlGaN barrier electric field and composition and 2DEG Fermi energy. This new information allows us to test and refine basic models of AlGaN/GaN heterostructures and transistors.
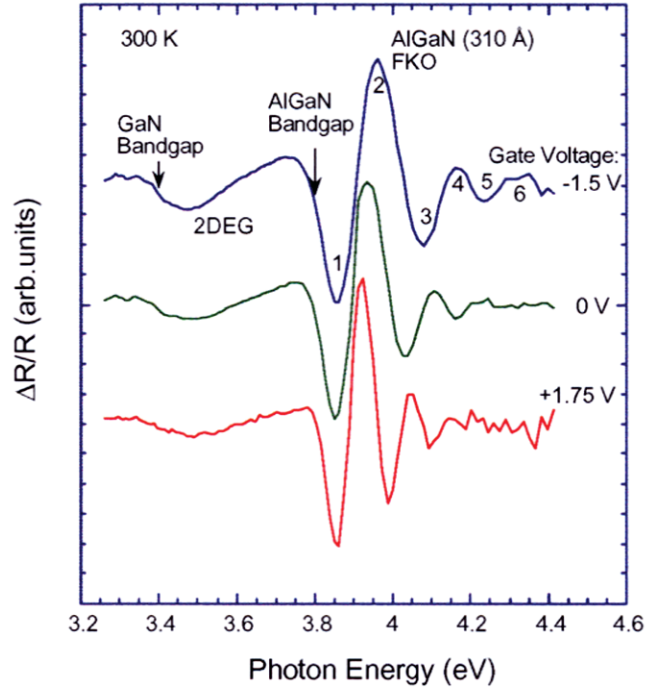
Figure 1. Electroreflectance spectra of an AlGaN/GaN HEMT for gate voltages, −1.5, 0, and +1.75 V.
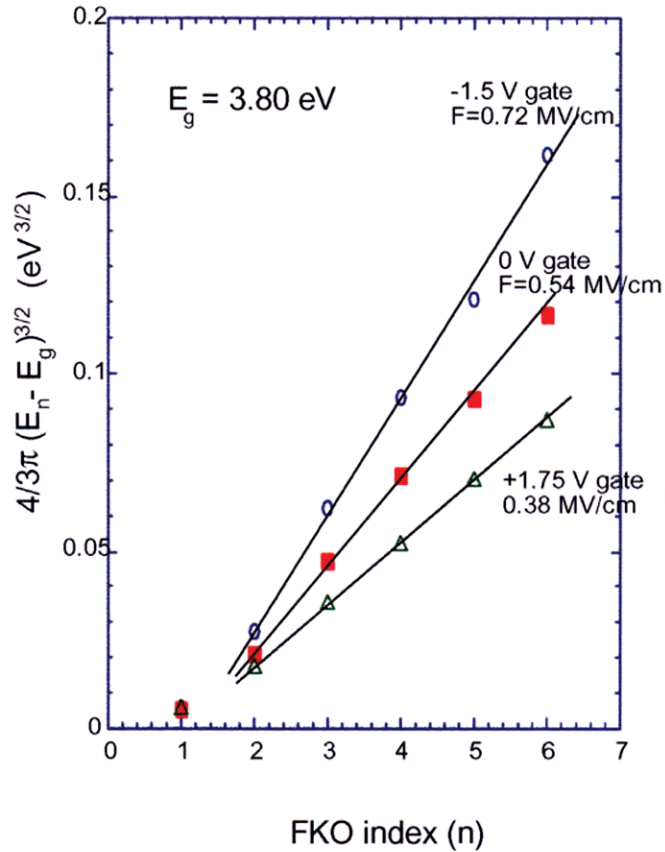
Figure 2. Determination of AlGaN barrier electric fields from Franz-Keldysh oscillation extreme energies.

Multiscale Modeling of Hydrogen in Gallium Nitride

by S. M. Myers and A. F. Wright

Motivation—Hydrogen is incorporated into p-type GaN during growth by metal-organic chemical vapor deposition. The H is strongly bound to the Mg acceptors, rendering them electrically inactive, and this impairs the efficiency of light-emitting diodes by reducing the conductivity of the p-type layer. Removal of the H by annealing entails a delicate balance between maximizing acceptor activation and minimizing thermal damage to the semiconductor. Moreover, redistribution of residual H during the operation of a device may alter its characteristics with time. To address these issues optimally, a quantitatively predictive model of H behavior in GaN p-n junctions is needed.

Accomplishment—We developed a theoretical description of H behavior in GaN p-n junctions by treating the system at three size scales, thereby allowing macroscopic properties to be formulated in terms of atomic processes. First, density-functional theory was used to 1) identify the stable states of the H, 2) calculate their energies and vibrational frequencies, and 3) predict configurational paths and activation energies for H migration through the lattice. The accuracy of these calculations was enhanced by using large super cells and incorporating refinements such as the generalized-gradient approximation for exchange and correlation. Figure 1 shows the strongly bound Mg-H complex responsible for acceptor passivation, along with predicted states of free H^+ during diffusion along the c axis of the hexagonal wurtzite lattice. At the second of the three size scales, the local migration of H^+ to and from the Mg^- reaction site was treated by solving the problem of diffusion with

electrostatic attraction to a trap and, simultaneously, drift in the linear electric field of the device. This is the classic Onsager problem, whose solution we generalized to take account of the predicted large anisotropy of H^+ diffusion in the non-cubic GaN lattice. Finally, evolution on the scale of the device was treated by solving coupled drift-diffusion-reaction equations for H^+, H^0, H^-, holes, and conduction electrons with simultaneous solution of Poisson's equation.

A stringent test of the theoretical model was provided by comparison with recent experimental results of C. H. Seager, who used capacitance-voltage (C-V) measurements to profile fixed charge in a p-n junction having H in the p-type layer. Hydrogen subtracts from the space charge produced by the Mg^-, either by forming the neutral Mg-H complex or existing as detached H^+, so that the quantity measured in the C-V profiling is the concentration difference $[Mg^-] - [H^+]$. Figure 2 shows a comparison between theory and a typical experiment where the H distribution was first equilibrated at zero bias and 350ºC and then caused to change by applying a reverse bias at 264ºC. (The Mg doping is graded, rising approximately linearly from zero at the junction.) The close agreement seen in the figure was achieved over the temperature range 212-287ºC by adjusting the diffusion prefactor together with the sum of the diffusion activation energy for H^+ and its binding energy at the Mg. The fitted sum is 1.77 eV, in good agreement with the theoretical prediction of 1.6 eV.

Significance—This work represents substantial progress toward the quantitative prediction capability needed to deal with H effects in GaN devices.
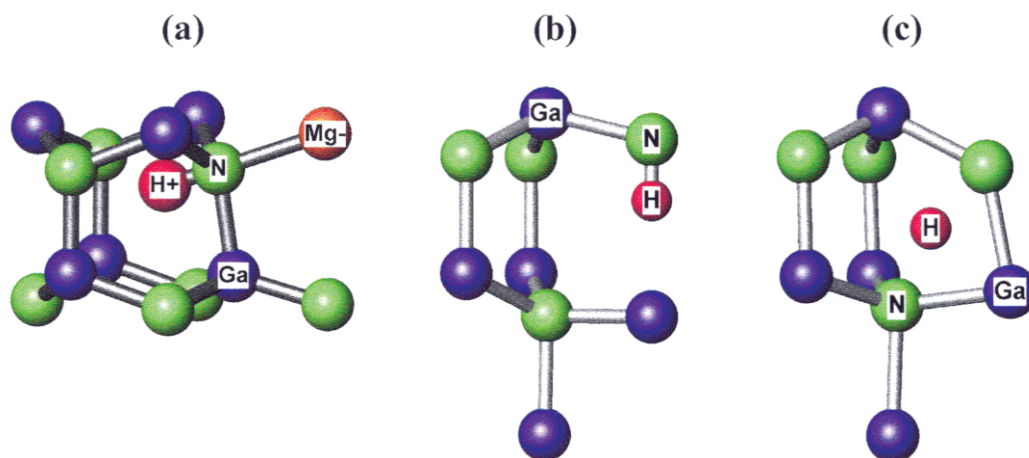
Figure 1. Hydrogen states in p-GaN from density-functional theory. (a) Neutral Mg-H complex. (b) Lowest-energy configuration of H^+ detached from the Mg. (c) Saddle point during hopping of H^+ between N atoms.
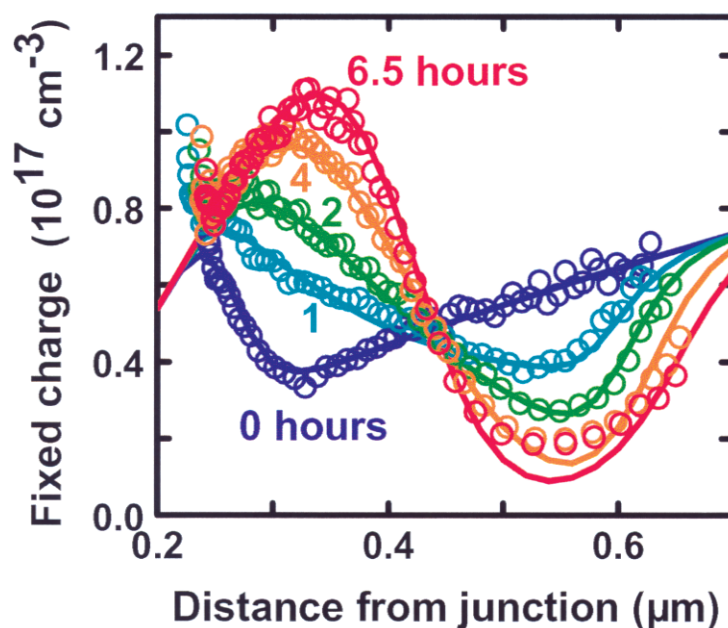
Figure 2. Hydrogen redistribution in the p-type region of a p-n junction at 264°C under a reverse bias of 12 V, as reflected in the depth profile of negative fixed charge = $[Mg^-] - [H^+]$. Lines: from the fitted theoretical model. Circles: from the experiments of C. H. Seager. The Mg-dopant concentration rises nearly linearly from zero at the junction and coincides with the initial, rising portion of the charge-density profile.

The Role of Carbon in GaN

by C. H. Seager and A. F. Wright

Motivation—GaN is an important emerging material used for the fabrication of blue and ultraviolet emitting solid state light sources. The role of carbon introduced as an impurity into GaN is an unsettled issue, despite a considerable amount of experimental effort on this system. Part of the impetus for this work has been the realization that Mg, presently the only viable *p*-type dopant in GaN, has numerous problems; C could, in principle, be an alternative *p*-type dopant in GaN when substituting on the nitrogen site (C_N). Some carbon is always present in GaN films grown from metal-organic precursors, and numerous attempts have been made to deliberately introduce this impurity as a dopant. However, the reported electrical properties of deliberately doped films have varied widely, and it is generally recognized that film growth conditions play an important role in controlling the amount of C that is actually incorporated.

Accomplishment—GaN samples were grown with varying amounts of both Si (a shallow donor) and carbon; these were characterized electrically and optically. The resulting data were compared to electronic structure calculations using Density Functional Theory (DFT). In samples where the carbon concentration is less than that of silicon, the deduced density of [donors − acceptors] is found to be close to the SIMS-measured density of Si minus that of carbon. This indicates that carbon substitutes for N, acting as an acceptor and partially compensating the material. However when carbon densities exceed those for Si, GaN becomes semi-insulating, not *p*-type. Our DFT calculations suggest that this is due to carbon occupation of both N and Ga substitutional

lattice sites. We find that the formation energies of carbon in both substitutional sites are strong functions of both the Fermi level and growth stoichiometry (see Fig. 1). This Fermi level dependence causes self-compensation when [C] > [Si] because the formation energy of the C_{Ga} configuration (the donor state) becomes equal to that of C_N, effectively pinning the Fermi level and causing semi-insulating behavior. The growth condition dependence of carbon site formation energies predicted by DFT is consistent with past literature reports that effective *p*-type doping of GaN has only been accomplished with techniques such as MBE which can achieve Ga-rich growth conditions. This means that *p*-type GaN cannot be achieved with carbon doping in MOVPE, which is the only cost-effective GaN growth method. This research also explains, for the first time, why closely compensated GaN layers for High Electron Mobility Transistors (HEMTs) can be readily fabricated with carbon doping. Figure 2 shows the luminescence band seen only in highly C-doped, semi-insulating GaN samples; it is believed that this band is due to donor-acceptor transitions from C_{Ga} to C_N.

Significance—This comparison of careful experiments with sophisticated theory in GaN has greatly increased our knowledge of the electronic behavior of carbon impurities in this technologically important semiconductor. While the small amounts of carbon usually present in MOVPE reactors will always serve as compensating acceptors in *n*-type GaN, *p*-type GaN cannot be achieved with carbon, unless some method is found to produce high quality films under gallium-rich growth conditions.
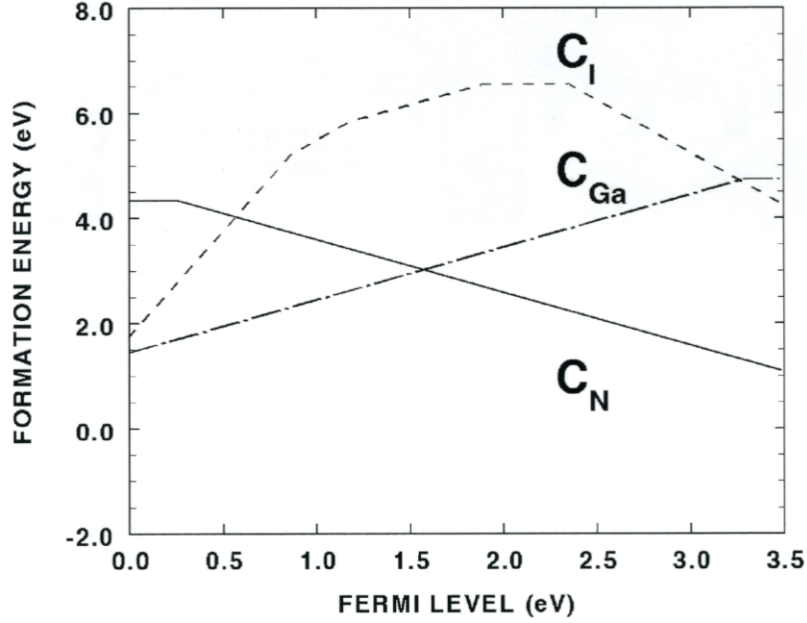
Figure 1. Formation energies of interstitial carbon (C_I), C_N, and C_{Ga} as a function of Fermi level position in the GaN bandgap calculated by DFT for the wurtzite structure. N-rich growth conditions were simulated here. As more carbon is added to *n*-type GaN, the Fermi level drops, eventually making the formation of both C_{Ga} and C_N highly probable, which leads to insulating behavior.
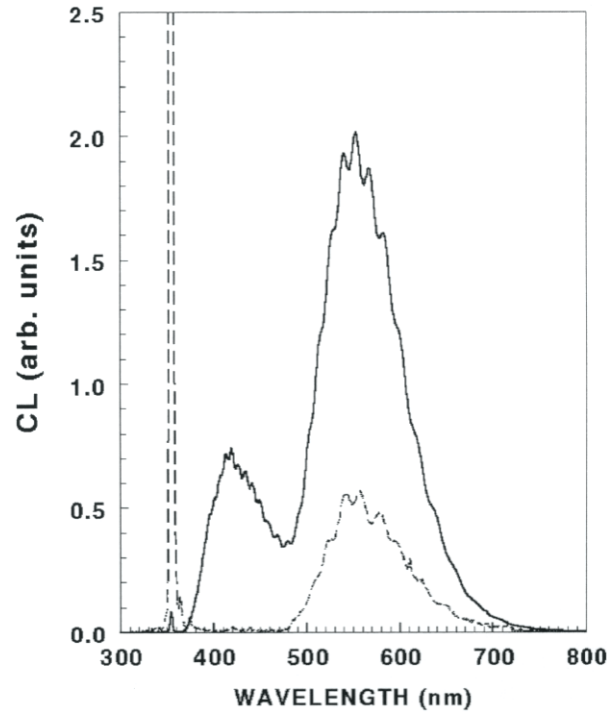
Figure 2. Cathodoluminescence spectra for two samples of C-doped GaN at 77K. The solid line is data for a semi-insulating sample where [C] > [Si]; the luminescence band near 3 eV (415 nm) is seen only for samples where carbon is the majority dopant impurity. The energy of this band coincides with the DFT-calculated energy level separation between carbon donor and acceptor sites.

Semiconductor Nanostructures

3D Surface Sculpting – Using Growth Kinetics to Tailor Nanostructures

by J. A. Floro

Motivation—Quantum dots receive considerable attention because they could revolutionize optoelectronics technologies for communications and sensing. Extraordinary improvements are also foreseen using quantum-computing architectures, realized by physical devices composed of ordered nanostructure arrays. However, the near-atomic length scale control required to build such structures is well beyond the capabilities of standard lithographic approaches to device fabrication. This severe limitation can be overcome through the directed self-assembly of materials into complex 3D nanostructures via manipulation of the natural processes occurring associated with their growth.

Accomplishment—An exciting approach to self-assembly of 3D nanostructures on surfaces uses strain-driven quantum dot formation during heteroepitaxial semiconductor film growth. Our previous work on self-assembly of strained SiGe alloy quantum dots on Si substrates elucidated the thermodynamic driving forces for dot formation and ordering. These growth experiments, summarized in Fig. 1, occur in the high-temperature, low growth rate regime labeled as "quasi-equilibrium". By moving outside of this regime, kinetically limited strain-layer growth can be used to further tailor self-assembly of surface nanostructures–a process we refer to as 3D *surface sculpting*. We have demonstrated that surprisingly complex structures may be generating by the surface sculpting approach.

The most intriguing sculpting behavior occurs in the low-temperature, high rate regime labeled as "high supersaturation" in Fig. 1. Here, operation of so-called cooperative-nucleation processes fosters the formation of quantum dot molecules–an assemblage of four quantum dots (the square ring-like structures) that are elastically bound together by the presence of a quantum "anti-dot" in the center of the molecule. These molecules have the very useful (and surprising) property that they are size-selected, that is, they all seek to achieve some specific maximum size. Stable, size-selected quantum molecules in the four-dot ring arrangement are in the exact configuration needed to serve as quantum cellular automata (QCA). QCAs are a candidate single-electron charge-switching device that would form the basic computing element in a quantum computing architecture.

We further manipulate the surface by inserting annealing steps into the overall process that drastically modify the resulting structures. This can produce, for example, either extensive arrays of serpentine quantum wires and antiwires, or dense quantum molecular arrays, depending on the order of growth and annealing (see the upper right corner of Fig. 1). These structures suggest the eventual possibility of self-assembling both the quantum cellular automata (QCA) computing elements and the wiring connections.

Significance—3D surface sculpting opens up new avenues for self-assembly of complex nanostructures. While we are still in the learning stages of manipulating nanostructure formation, this work provides a significant proof of concept on how to proceed. We anticipate achieving further control over the sculpting process by combining 3D surface sculpting with external lithographic patterning, thereby providing unprecedented capabilities to direct and tailor the self-assembly of functional complex computing structures.
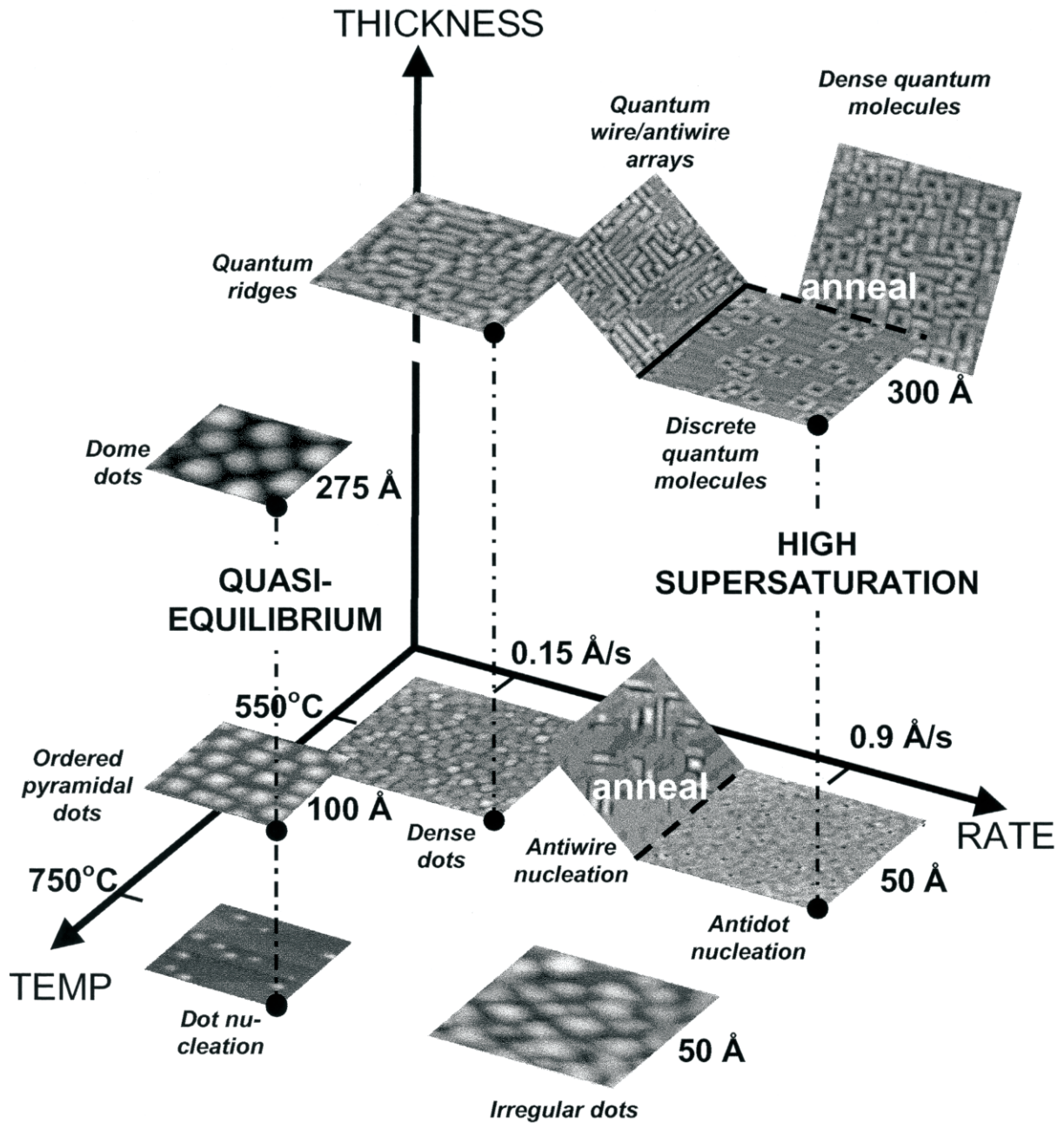
Figure 1. A portion of "processing space" for investigating and manipulating quantum dot self-assembly. The structures associated with "quasi-equilibrium" processing enable us to understand the fundamental driving forces for self-assembly. The structures associated with "high supersaturation" are tailored (sculpted) using growth kinetics.

Use of Compositionally Modulated Structures as Templates for Growth of Highly Ordered Arrays of Quantum Dots

by J. L. Reno, and D. M. Follstaedt

Motivation—Since the density of states of uniform arrays of quantum dots can be expressed theoretically as set of Dirac delta functions, quantum dots have been a subject of great interest for applications in advanced opto-electronic devices. The self-organization of InAs islands has been used as a primary method for the realization of devices based on quantum dots. However it is not physically possible to achieve a truly uniform ensemble of quantum dots by self-assembly due to the random nature of the process. The randomness of the size and position of the dots smears out the density of states and thereby minimizes the potential gains of using them.

Accomplishment—In earlier work we have demonstrated that InAs/AlAs short period superlattices (SPS) grown on InP substrates exhibit a modulation of the composition perpendicular to the growth direction, parallel to the surface of the substrate. Under appropriate growth conditions, there are two composition modulation waves running at an angle of approximately 58° to one another. Because the resulting strain is maximized at the intersections of these two waves, InAs quantum dots grown over modulated layers will preferentially nucleate at those locations. In this manner, the compositionally modulated structure serves as a nano-sized template for self-organizing the quantum dot array. The spacing between the quantum dots will be about 200Å and is nearly an order of magnitude smaller than can be achieved from standard lithographic techniques.

Several samples have been grown. Each sample began with an InAlAs buffer layer grown on InP followed by a 100-period SPS. Each period consisted of 1.90 monolayers AlAs and 1.77 monolayers of InAs. On top of the SPS, was grown an InAlAs barrier, the InAs dots layer, and finally a InAlAS cap layer. Figure 1 shows a cross-section transmission electron micrograph of a sample. The InAs quantum dots are clearly visible. Their size is approximately 10nm x 2nm, and they form over the InAs rich columns in the SPS, as predicted. Figure 2 is an AFM of an uncapped sample. The regular array of dots is visible. The pattern is as expected with an angle of 58° between the rows of dots. The quantum dot density is about 1 x 10^{11}/cm^2. We are presently investigating the optical properties of the dots.

Significance—The structures we are producing can potentially lead to novel electronic states and optical transitions. The close spacing between dots (20-30 nm) will promote strong interactions between atomic-like states in neighboring dots, such as tunneling interactions. A dense, well-ordered array of dots could even produce a "crystal" of quantum dots, with further modification of electronic levels by the imposed translational periodicity. Optical emission energies and perhaps polarizations would be similarly altered by this re-configuring of the dots with the modulated substrate. A sufficiently high degree of ordering might even produce photonic lattice behavior in multiple layers of quantum dots.
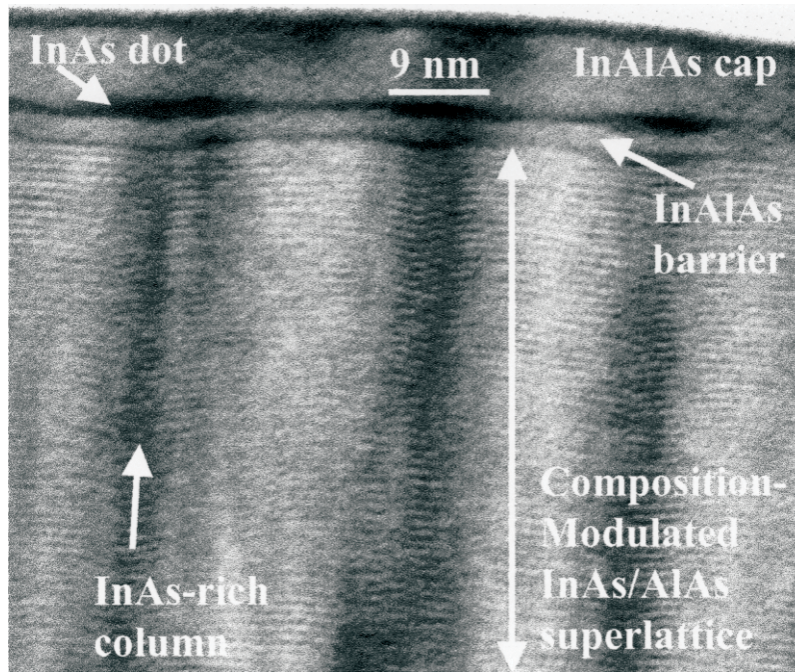
Figure 1. Cross-sectional transmission electron micrograph of a quantum dot sample showing the alignment of the dots on top of the InAs rich columns.
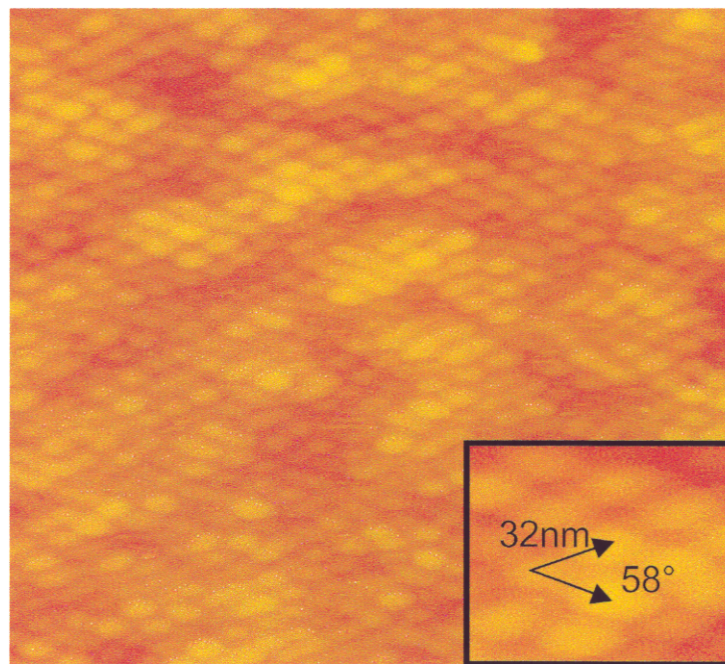
Figure 2. Atomic force microscopy image of an uncapped quantum dot sample showing the regular array of dots.

Perturbation-induced Phase Separation in Heteroepitaxial Semiconductor Alloys

by S. R. Lee and N. A. Modine

Motivation—Compound-semiconductor films defy the conventional thermodynamics of mixing by decomposing during growth at temperatures where the bulk alloy is fully miscible. The free surface required for epitaxial growth of these alloys enables thermodynamic mechanisms that may explain why these chemically miscible alloys decompose. For example, a planar surface elastically relaxes coherency strain when decomposition occurs laterally along the surface; this lowers the strain energy near the surface and raises the miscibility gap back towards the chemical spinodal. If surface morphology develops, it may couple with lateral decomposition to further reduce strain energy. In lattice-mismatched films, this raises the critical temperature for decomposition above the chemical spinodal, but a problem arises because bulk diffusion in semiconductors is very slow at the growth temperature. When sub-surface domains are immobile, these thermodynamic models may not apply.

This bulk-kinetic limitation motivates increasing interest in dynamic transport theories that focus on much faster surface-diffusion phenomena occurring during growth. An outstanding prediction of dynamic perturbation theories is instability at temperatures above the chemical spinodal–*even for planar lattice-matched films*. The role of growth in producing this surprising instability is controversial: Some authors describe the instability as a growth-induced kinetic phenomenon, while others find instability in both static and growing systems.

Accomplishment—We resolve these dissimilar views by determining the energetic ground state of a binary-alloy surface layer in the presence of a pre-existing, buried composition-perturbation. We find that the ground state of a *non-growing*

perturbed surface layer drives decomposition above the chemical spinodal that is identical to that seen in dynamic theories. Thus, transport dynamics during growth do not induce this instability; instead, the perturbed ground state is the direct cause of instability.

Special perturbation geometries and surface-strains are required for this instability to occur. Figure 1 shows that the geometry of the perturbation determines the surface-strain. As the thickness-wavelength ratio (t/λ) of the perturbation increases, elastic distortion at the perturbed surface also increases. This distorted surface interacts with the alloy composition to produce the three distinct surface-strain regimes summarized in Fig. 1. Importantly, thick perturbations actually *amplify* the magnitude of the surface strain (see region 3 in Fig. 1). This amplification produces novel strain-energy distributions that destabilize miscible films.

We also considered the stabilizing role of configurational entropy at large perturbation amplitudes. We find that entropy produces nonlinear feedback that terminates the growth of linearly unstable perturbations. Figure 2 shows that our nonlinear stability theory explains the amplitude, the composition range, and the parabolic shape of the stability boundary seen for the growth of pseudo-binary AlInAs alloys.

Significance—Alloy decomposition produces self-assembled nanostructures that are used to produce optoelectronic-device innovations. At the same time, *unintended* decomposition may harm existing device designs that require homogeneous alloys. Through improved understanding of the phase separation process, we can tailor the alloy to each case as needed.
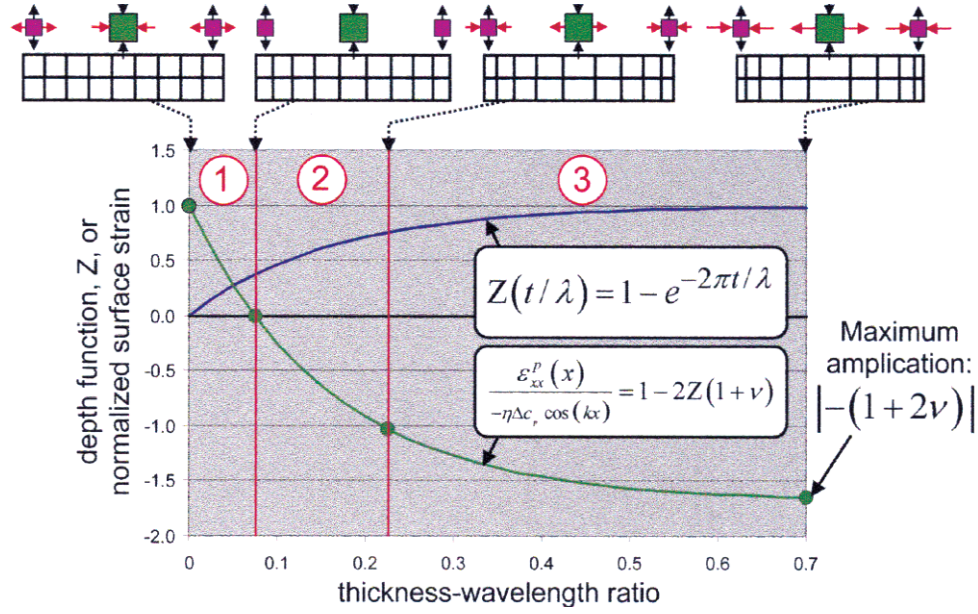
Figure 1. The buried perturbation creates a bulk-elastic response that distorts the surface-lattice (see plan views at top). The distortion amplitude is proportional to the elastic depth function, $Z(t/\lambda)$. Epitaxy of indium-rich (green squares) or aluminum-rich (pink squares) domains on the distorted surface lattice of perturbed AlInAs leads to spatial modulation of the local coherency strain (red and black arrows at top). As t/λ varies, the amplitude of the surface-strain moves through three distinct regimes: (1) partial relaxation, (2) reversal, and (3) amplification.
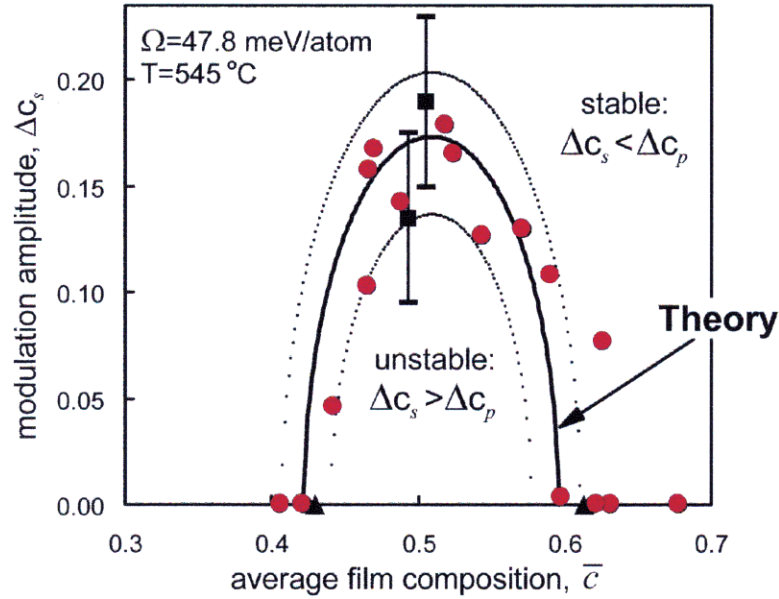
Figure 2. The large-amplitude stability diagram for AlInAs heteroepitaxial alloys, where Δc_p is the composition-modulation amplitude of the buried perturbation, and Δc_s is the composition-modulation amplitude of the mobile surface layer. The solid line is the replication condition, $\Delta c_s = \Delta c_p$, that is predicted by our non-linear theory; squares are STEM measurements of Δc_s (Twesten et al., Phys. Rev. B 60 [1999] 13619); circles and triangles are XRD measurements of Δc_s (Lee et al., J. Mat. Sci.: Electronic Mat. 10 [1999] 191).

Surfactant Effects on the Nucleation of Semiconductor Nanostructures

by R. M. Biefeld and J. G . Cederberg

Motivation—We are exploring the growth by Metal Organic Chemical Vapor Deposition (MOCVD) of semiconductor nanostructures also know as quantum dots. We are interested in this phenomenon for two reasons: first to study the nucleation of highly mismatched zincblende semiconductors and second to explore the effects of the addition of surfactants on the nucleation of these nanostructures in novel systems.

Accomplishment—We have discovered a novel surfactant effect for the formation of III-V nanostructures that dramatically changes the island size and density distributions. The addition of antimony to InAs, forming a dilute alloy InAs(Sb), results in dramatic transformations of the nanostructures formed. Similar behavior is found when As is added to InSb to form a dilute alloy In(As)Sb. The growth of semiconductor nanostructures by CVD requires understanding of the initial nucleation of deposits. Using reactor growth studies coupled with *ex situ* sample analysis by Atomic Force Microscopy (AFM), we have conducted a detailed investigation of these two different material systems: InAs on GaAs(001) and InSb on GaSb(001). These films are predicted to nucleate by the Stranski-Krastanov (SK) mechanism, forming nanometer-sized islands in a two-dimensional wetting layer. The strong surfactant effect is a surprise.

Small, dense islands or quantum dots are formed for 9 Å-thick InAs grown on GaAs(001), that are elongated towards the [-110] direction. The addition of antimony results in the coalescence of these islands into long, wire-like structures that are elongated in the perpendicular direction, i.e., in the [110] direction. Isolated islands can be formed for the InAs(Sb) alloy by decreasing the deposit thickness to 7.5 Å. The islands thus formed are larger than InAs structures, and are still elongated in the [110] direction. Looking at the complementary case of InSb on GaSb(001), we see formation of very large islands under all conditions investigated. The addition of As to form In(As)Sb produces small, dense islands similar to InAs quantum dots. The addition of antimony to an arsenic-terminated surface apparently increases the diffusion length of adatoms and decreases the surface energy. Conversely, the addition of arsenic to antimony-terminated surfaces decreases the diffusion length and increases the surface energy.

Significance—The nucleation of nanostructures by self-assembly mechanisms is governed largely by the film properties that are only controlled in a gross way via growth settings. We have shown, by the addition of small amounts of a dilute component, that this transformation can be adjusted. Species that form stronger bonds result in smaller islands, while species with weaker bonds allow faster and more facile diffusion, which results in larger islands. These observations suggest a way to manipulate the size and dimensions of nucleated islands, or force a nucleated layer to wet a substrate surface more rapidly. By adding dilute constituents to nanostructures we can change the electronic properties, not only by varying their size, but also their bandgap. This creates a new method to vary the properties of nanostructures.
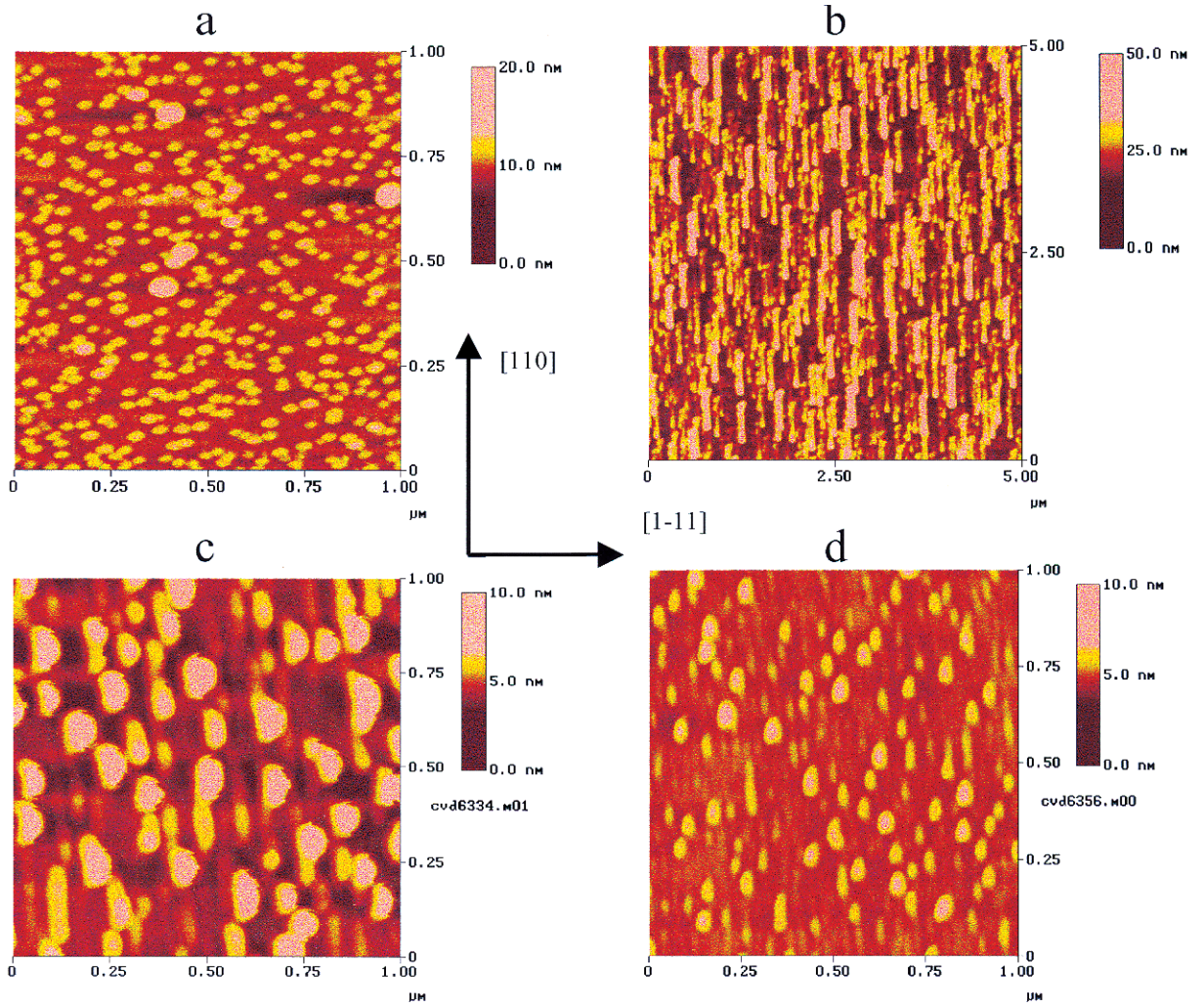
Figure 1. Atomic Force Microscope images showing the effects of Sb and As additions to InAs and InSb quantum dot structures, respectively. (a) AFM showing InAs islands on a GaAs substrate. (b) The addition of Sb during the growth of InAs on GaAs results in larger elongated islands. (c) InSb islands on a GaSb substrate are initially large with a wide size distribution. (d) The addition of As during the growth of InSb on GaSb results in smaller, more uniform islands. Not only does the addition of these group five elements alter the electronic properties of the semiconductors but also the film's nucleation properties.

Nanostructured Materials and Nanoscale Phenomena

Mechanical Properties of Nanostructured Metals

by J. A. Knapp, D. M. Follstaedt, and S. M. Myers

Motivation—We are studying the relationship of nanostructure to the mechanical properties of metals, using both pulsed laser deposition and ion implantation to manipulate nanostructure at scales from 1 to 1000 nm. We are exploring the levels of strength that can be achieved using grain size refinement or precipitate hardening and developing an understanding of how the mechanical properties of metal films are affected by porosity or a fine dispersion of high-pressure bubbles, such as the He bubbles formed in neutron tube target films as they age.

Accomplishment—Over the last few years we have used pulsed laser deposition to form poly-crystalline Ni and Cu layers with full density and uniform grain size. These layers exhibit Hall-Petch hardening to grain dimensions as small as 20 nm, giving yield strengths as high as 3 GPa with retention of substantial ductility. We have recently performed *in-situ* Transmission Electron Microscopy (TEM) of these very fine-grained films, confirming dislocation-mediated deformation. Even higher strengths are achieved using ion implantation to introduce high densities of oxide nanoparticles into Ni, producing strengths up to 6 GPa in quantitative agreement with recent formulations of the Orowan mechanism.

More recently, in extending these fundamental studies to the effects of He release in tritiated metal films, we have used ion implantation to introduce nanometer-scale bubbles. Such a nanostructure also produces strengthening, ascribed to dislocation pinning, but with increased fracture instability. The example we show is from a well-annealed Ni sample implanted with He at several energies from 10 to 180 keV to form a uniform concentration of ~5.2 at.% He to a depth of ~700 nm. Examination of the layer with TEM, as shown in Fig. 1, confirmed the uniformity and revealed a fine dispersion of He bubbles ≤1 nm in diameter. The sample was then indented both inside and outside the implanted area and the results analyzed with finite-element modeling to extract the properties of just the He-containing layer. Representative force vs. depth curves are shown in Fig. 2, with the red curve obtained from untreated Ni and the rest from the He-implanted area. The computer analysis shows that the He bubbles strengthen the Ni considerably, presumably by blocking dislocation motion in the material. The implanted layer has a hardness of 6.9 GPa vs. 1.1 GPa for the untreated Ni. However, as can be seen from the figure, the He-containing layer fractures as indentation proceeds past ~90 nm, possibly due to inter-bubble fracture.

Significance—This work has increased our understanding of how the strength of metals can be greatly enhanced through either nanoparticle dispersion hardening or grain size refinement. We are beginning to extend this understanding to the effects on mechanical properties of a fine dispersion of gas bubbles. Key aspects are the continuing development of quantitative micro-mechanical testing, based on nanoindentation combined with finite-element modeling, and the new development of *in-situ* TEM for direct observation of deformation. The fundamental knowledge that we are gaining has the potential for significantly enhancing wear resistance of micro-electromechanical system parts and for providing process improvements in neutron tube applications.
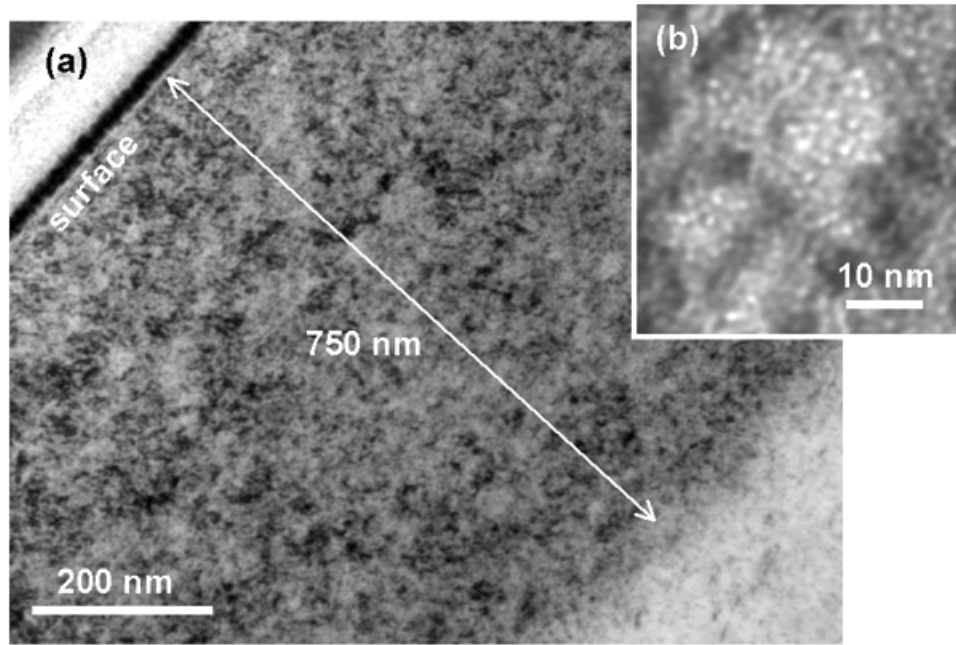
Figure 1. Bright-field, cross-section TEM views of a He-implanted Ni layer. (a) Overview of implant region, with damage extending to ~750 nm. (b) High magnification view of the central part of the layer imaged in underfocus condition, showing He bubbles ≤1 nm in diameter (light spots).
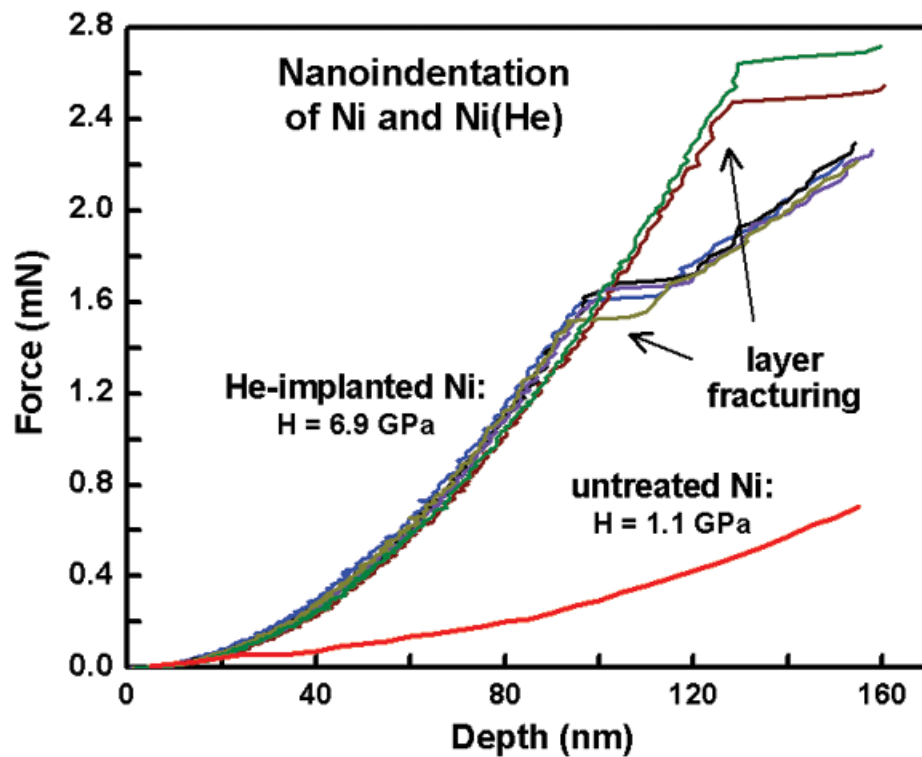
Figure 1. Experimental nanoindentation results from untreated Ni and Ni implanted with 5 at.% He to ~700 nm depth, forming 1 nm He bubbles. The Ni(He) is much harder than pure Ni, but fails catastrophically at sufficiently high shear stress.

Enhanced Magnetism in 1.8 nm Cobalt Nanoparticles

by E. L. Venturini, J. P. Wilcoxon and P. N. Provencio

Motivation—Nanoparticles reside at the crossover between bulk and atomic behavior, leading to unique physics. In particular, the confinement of electrons in metallic particles with diameters of 1-3 nm generates profound changes in technologically important properties such as optical absorption and band magnetism. The substantial fraction of surface atoms in nanoparticles provides the opportunity to manipulate these properties via interfacial interactions with surfactants or other absorbants and through the sequential growth of additional layers (shells). We are studying the structural and magnetic behavior of simple metallic nanoparticles (iron, cobalt, and nickel) to gain insight into these fundamental issues. This work is motivated by the physics and diverse applications of magnetic particles, including magnetostrictive composites, ferrofluids, data storage, refrigeration, and medicine.

Accomplishment—We have observed a saturation magnetization ~10% larger than the bulk value in 1.8 nm cobalt particles inside a surfactant inverse micelle in frozen decane. Figure 1 compares partial magnetic hysteresis loops measured at 20 K for nanoparticles stored in decane plus surfactant at room temperature in an oxygen-free argon environment. At high field the particle magnetism approaches a constant value (saturation). One day after synthesis this saturation magnetization is ~25% of that for bulk cobalt; after a month it exceeds bulk cobalt and remains stable at longer times.

Conventional "wisdom" is that magnetism in nanoparticles decreases dramatically due to interaction of surface atoms with external neighbors. Using the metallic radius of cobalt, a 1.8 nm close-packed structure contains 147 atoms, and 63% are surface atoms. Our data contradict this wisdom, suggesting that the orbital magnetism of the surface cobalt atoms is enhanced over that in bulk cobalt. A similar enhancement has been reported for cobalt nanoparticles formed in a gas stream where the surface atoms have no external neighbors. The saturation magnetization exceeds the bulk value from 4 K to at least 200 K; the magnetic anisotropy is comparable to the bulk. High-resolution transmission electron microscopy shows a lattice spacing similar to that of hexagonal-close-packed bulk cobalt.

Figure 2 compares the effects of various surfactants on the cobalt nanoparticles. The magnetism in an aged cobalt nanoparticle is not affected by surfactant with a phosphine head group or by oleic acid; a thiol lowers the saturation magnetization by over one-third. In contrast, an amine surfactant appears to attack the particles, resulting in free cobalt cations that do not show magnetic saturation in high fields.

Significance—Enhanced magnetism and bulk anisotropy for 1.8 nm cobalt particles in a solid matrix demonstrate that interfacial interaction between surface cobalt atoms and surfactants is not necessarily detrimental. Several different surfactants had little effect on the nanoparticles. Magnetic saturation independent of temperature to 200 K suggests strong exchange coupling between "interior" and surface cobalt atoms via intinerant electrons; the collective magnetism among the cobalt atoms leads each nanoparticle to act as a giant spin. These results show that practical applications utilizing macroscopic magnetic particles such as ferrofluids and data storage can be extended to nanoparticles with comparable or even superior performance.

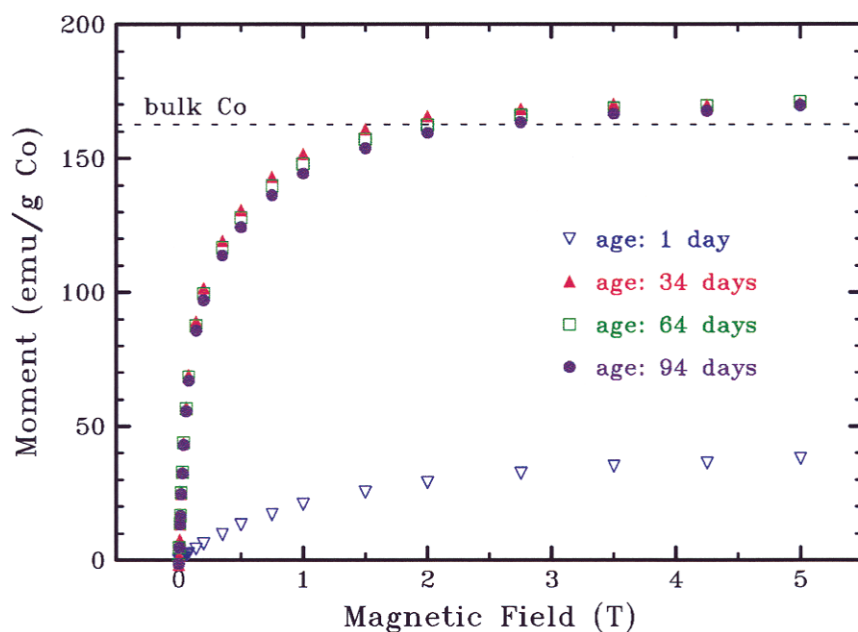**Figure 1**. Isothermal magnetism versus field at 20 K shows that 1.8 nm cobalt nanoparticles are stable after one month with high-field magnetic saturation above the value for bulk cobalt.
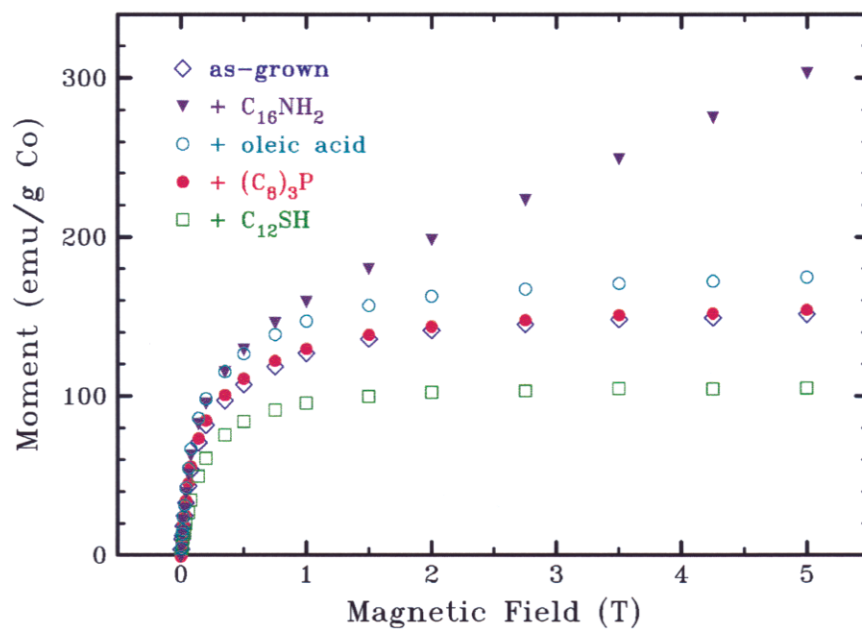

Figure 2. High-field magnetism at 20 K of 1.8 nm cobalt nanoparticles is sensitive to strongly bound surfactants such as amines and thiols but not to weakly bound oleic acid or phosphines.

Nanoporous-Carbon Films for MicroChemLab Preconcentrators

by M. P. Siegal, D. L. Overmyer, R. J. Kottenstette, W. G . Yelton, and D. R. Tallant

Motivation—Preconcentrator materials for adsorbing analyte gases for detection by the Sandia MicroChemLab sensor systems are a reliability issue. We study the use of nanoporous-carbon (NPC) films, grown using line-of-sight deposition processes. With room-temperature growth and negligible residual stress, NPC coats any substrate to any desired thickness. Controlled deposition yields precise density, morphology, and porosity, with no discernable variation in surface chemistry. We demonstrate structurally-sound NPC films 8-µm-thick with density < 10 % that of graphite. The well-controlled porosity (available surface area) is demonstrated by using NPC as a preconcentrator for a nerve gas simulant.

Accomplishment—We grow NPC films using pulsed-laser deposition. Kinetic energy of the ablated carbon species is controlled by an inert background gas chamber pressure. Figure 1 shows scanning electron microscopy images for NPC films grown using different pressures of argon gas. These films have identical carbon atom areal density, differing only in porosity, thickness and mass density. Thickness ranges from 1.2-7.8 µm, and density, shown in Fig. 2, ranges from 1.08-0.18 g/cm^3, much lower than the 2.27 g/cm^3 for crystalline graphite, demonstrating tremendous control over a wide range of porosity and surface area. Raman spectroscopy finds no differences in chemical bonding, i.e., the bonding configurations in these materials are independent of NPC density.

Low-density carbon materials, like charcoal, are used as filters and adsorbers of various gases for storage or detection, but the compositions and textures are difficult to reproduce. We show the effectiveness of NPC as a preconcentrator adsorber for detection by gas chromatography (GC). We prepared two devices by depositing 0.45 and 2.26 µm thick NPC with density ~ 1 g/cm^3 directly onto a thermally-isolated microheater, used in the Sandia MicroChemLab. This low-power device desorbs collected analyte by heating to 200 °C in less than 10 ms. We studied the GC signal for the desorption of a nerve gas simulant, dimethyl methylphosphonate (DMMP), for collection times ranging from 10-120 s. Figure 3(a) shows the GC signal height as a function of collection time for both NPC film thicknesses. The thinner film provides a stronger GC signal for short collection times and saturates by 40 s. The signal from the thicker film is linear with time for the range of this experiment; saturation was not achieved. Figure 3(b) shows the integrated intensities of GC signals; both preconcentrator thicknesses follow the same behavior for DMMP desorption for short collection times. The thinner film indeed saturates by 40 s, while the thicker film continues collecting DMMP. These results show that analyte desorbs from thinner films more quickly, providing strong, sharp GC signals. However, thicker films can adsorb more analyte, with saturation levels likely to be directly proportional to the total NPC surface area in the preconcentrator.

Significance—Nanoporous-carbon films are a new material with highly-controlled density, morphology, and surface area. These properties are ideal for use as a carbon-based chemical preconcentrator for microsensor applications. NPC can also be used on a surface acoustic wave (SAW) microsensor for detection of a wide range of analyte gases including hazardous vapors and toxic industrial chemicals. NPC may be further functionalized via doping to provide additional chemical selectivity. NPC preconcentrators may also work in aqueous systems, with applications identifying chemical and/or biological toxins in ground water.
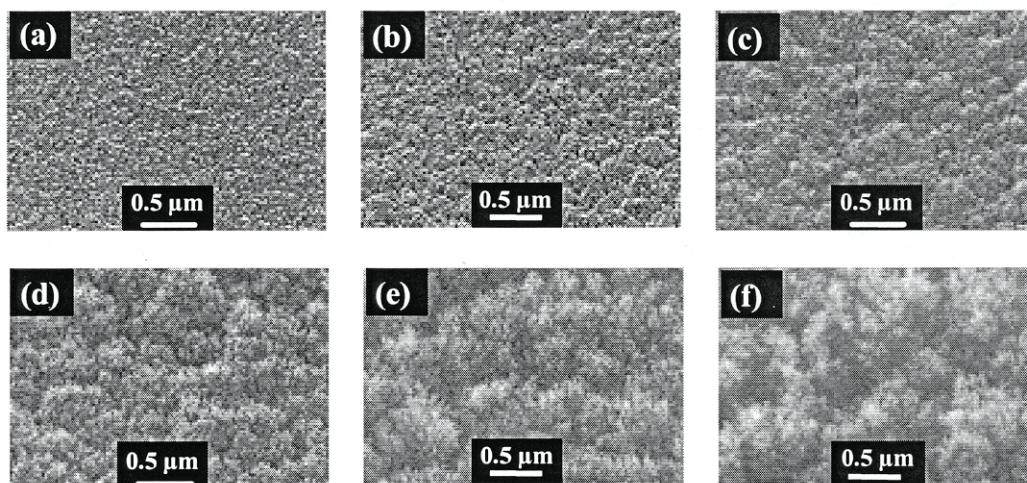
Figure 1. Scanning electron microscopy images of NPC films with constant C areal density deposited at the following p(Ar) and resulting thicknesses: (a) 175 mT, 1.2 μm; (b) 200 mT, 1.4 μm; (c) 225 mT, 1.9 μm; (d) 250 mT, 3.9 μm; (e) 275 mT, 5.9 μm; and (f) 300 mT, 7.8 μm.
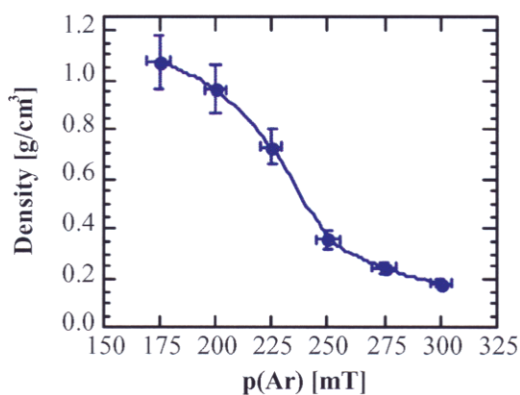
Figure 2. NPC film density as a function of p(Ar).
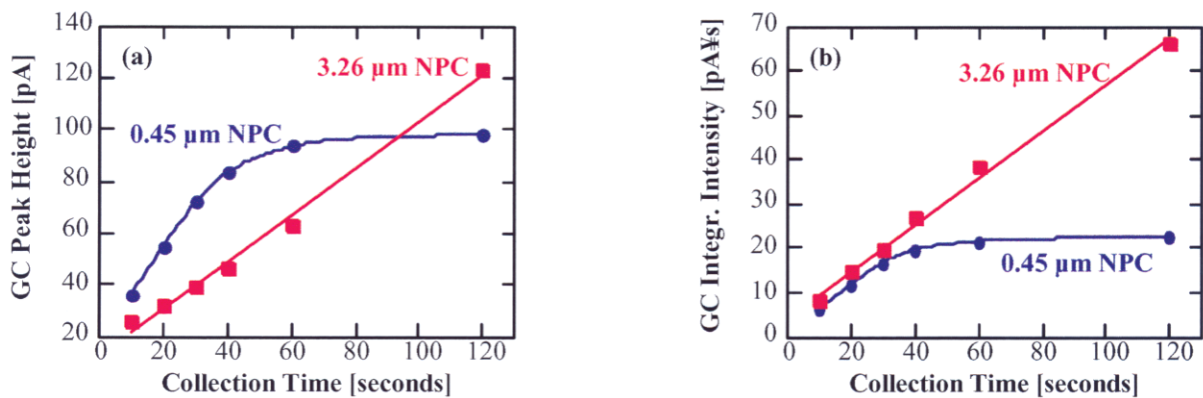
Figure 3. NPC thickness dependence for preconcentration of DMMP. (a) GC signal peakheights vs. collection time; and (b) GC signal integrated peak intensities vs. collection times.

Al Corrosion: Electronic Defects in Al Oxide

by J. P. Sullivan, R. G. Dunn, and J. C. Barbour

Motivation—Electronic defects within Al oxide determine electron transport, and this is of critical importance for a variety of tunneling-based electronic devices, such as single electron transistors or magnetic tunnel junctions. Even more importantly, these oxide defects may act as the initiation sites for the localized corrosion of Al, a significant materials aging problem. Despite the importance of electronic defects in Al oxide, their origin and nature are poorly understood. This work combines solid state electrical measurements with electrochemical treatments in order to deduce the nature of the defects within Al oxide.

Accomplishment—Using metal-insulator-metal solid state devices and electrochemical treatment, the electron transport mechanism and the nature and probable origin of the electronic defects in Al oxide films were determined. The study used three different types of Al oxide films: (1) Oxide films formed by exposure of Al to O_2 (O_2-formed); (2) exposure to an oxygen plasma (plasma-oxidized); (3) films formed by deposition of Al_2O_3 from a plasma source (plasma-deposited). The thickness and conductance of the various types of oxides were found to differ. From current-voltage and current-thickness measurements, electron transport in these films was determined to be governed by Fowler-Nordheim tunneling of electrons into a defect level in the oxide. This conduction behavior is characterized by an exponential dependence of the electron current on oxide thickness, as shown in Fig. 1. From the measured current vs. thickness dependence, the defect level in the oxide was found to be ~ 0.5 eV from the Al Fermi level.

The plasma-oxidized samples exhibited a lower concentration of electronic defects as evidenced by their lower conductance (Fig. 1). This lower defect density is related to a lower hydrogen content of the oxide, as determined using elastic recoil detection, ERD (Fig. 2). This indicates that hydrogen acts as an electronic defect in Al oxide, producing a defect level near mid-gap in the oxide.

Electrochemically polarizing the oxide films in an aqueous electrolyte either anodically (positive potential on the metal) or cathodically (negative potential) changes the defect concentration of the oxide. This process is theorized to occur by field-assisted diffusion of protons–the anodic field repelling protons from the Al/Al oxide interface and the cathodic field attracting protons. The effect of the polarization is to increase the conductance under cathodic polarization and decrease the conductance under anodic polarization (see Fig. 3).

Significance—The effect of oxide defects on the corrosion resistance of Al has been much debated. This work has shown that the defect density of the oxide is modified during the electrochemical treatment that is performed when Al is subjected to corrosion testing. Surprisingly, under anodic polarization, the electronic defect density is reduced, yet the Al is more susceptible to localized corrosion. The presence of electronic defects in the oxide alone is apparently not an initiator for corrosion. The magnitude of the electric field across the oxide does appear to be important, however. For solid state tunneling devices, the discovery of the relationship of hydrogen to electronic defects in the oxide is an important finding which should increase the ability to tailor the conductance of tunnel oxides based on Al oxide.
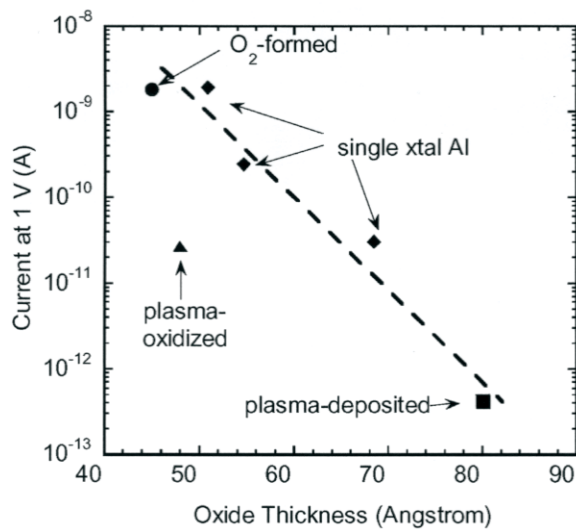
Figure 1. Current vs. oxide thickness for O$_2$-formed, plasma-oxidized, and plasma-deposited Al oxides. For comparison, naturally formed oxides on different crystallographic orientations of single crystal Al are also shown.
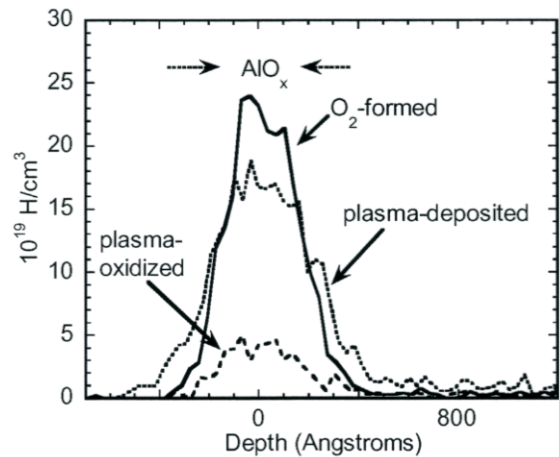
Figure 2. The H content for the three different types of Al oxides are shown, as measured using elastic recoil detection.
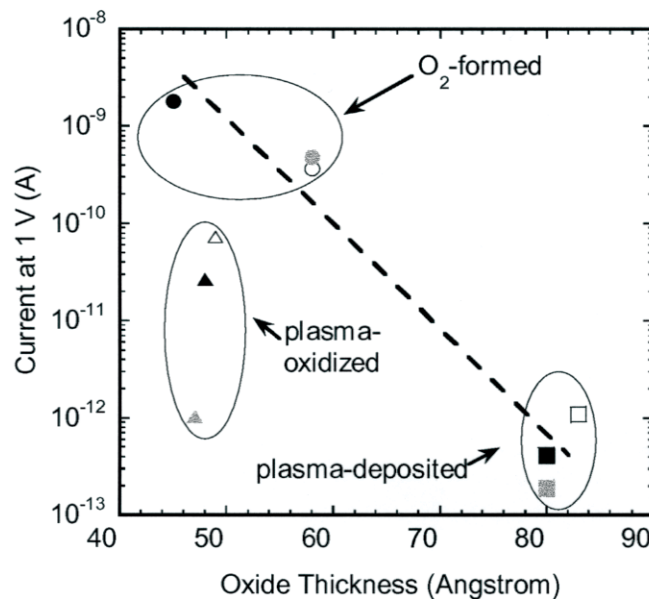
Figure 1. Current vs. oxide thickness for three types of Al oxides that were exposed to different electrochemical treatments. The filled black symbols are the untreated oxides, the filled gray symbols are for oxides exposed to anodic polarization, and the open symbols are for oxides exposed to cathodic polarization.

The Physics of Doped Quantum Paraelectrics: SrTiO$_3$ - Ca

by E. L. Venturini, G. A. Samara and W. Kleemann*

Motivation—The physics of dipolar dopants in the two incipient ferroelectrics (FEs) KTaO$_3$ and SrTiO$_3$ is of much current interest. The very high polarizability of these host lattices, associated with their soft FE modes, not only renormalizes the dipole moment of the dopant, but also functionally changes the dependence of the dipole-dipole interaction energy on the spacing between dipoles. A long-range ordered FE state occurs if the dopant concentration exceeds a critical value defined by the quantity nr_c^3, where n is the impurity concentration, and r_c is the correlation length for dipolar interactions; below this value a dipolar-glass-like (relaxor) state forms. We have shown earlier that the soft mode frequency, ω_s, increases rapidly with pressure leading to a sharp decrease in r_c ($\sim 1/\omega_s$), and this is responsible for the FE-to-Relaxor crossover in related systems. We have now investigated the effects of pressure and biasing electric field on the behavior of the model Sr$_{1-x}$Ca$_x$TiO$_3$ (SCT) system in the dilute limit (x = 0.007) where relaxor effects set in. The results provide new insights into the physics.

Accomplishment—Ca^{2+} occupies an off-center position in the lattice producing a dipole, which polarizes a small region around it forming a polar nanodomain whose size is determined by r_c. Evidence for the existence of these domains at temperatures well above the glass-like transition temperature, T$_m$, has come from Raman measurements. At 1 bar the domains grow with decreasing T as r_c increases leading to their increased correlations and culminating in a relaxor state (at T < T$_m$) whose signature is a broad, frequency-dependent peak in the susceptibility (or dielectric constant, ε') as well as dispersion below T$_m$ (Fig. 1). By increasing ω_s of the host, pressure can be expected to reduce r_c, and thereby the size of the nanodomains leading to loss of correlations and lowering of T$_m$. This is indeed

what we observe (Fig. 1), and a remarkable feature is the large magnitude of the effect, T$_m$ deceasing at 35 K/kbar. At pressures $\geq$ 0.5 kbar r_c becomes sufficiently small (Fig. 2) so that there is no overlap or correlations among domains leading to the complete suppression of the relaxor state and the evolution of a quantum paraelectric state (akin to that of pure SrTiO$_3$)–a state characterized by a large T-independent ε' over a substantial T range at low T (Fig. 1, 4 kbar).

Whereas pressure lowers T$_m$, a biasing dc electric field shifts T$_m$ higher while suppressing the magnitude of ε'. These effects result from the field stabilization of the local potential for dipolar motion (Fig. 3) requiring more energy to induce the transition, and from the alignment and field clamping of the polarization, which reduces ε'. Field bias also reduces the strength of the relaxational response, and at sufficiently high fields, a reemergence of a FE state can be expected. We see some evidence for this for E = 400 V/cm.

Significance—The results emphasize the important role of pressure in the study of soft FE mode systems. The frequency, ω_s (a long wavelength TO phonon) is determined by a delicate balance between competing short-range and long-range Coulombic forces. Near cancellation of these forces leads to the very small values of ω_s for incipient FEs, at low temperature. Because these forces depend on interatomic separation r as $1/r^n$, where n is 6-10, and $1/r^3$, respectively, pressure leads to large changes in ω_s, thereby in ε' and r_c, which provide the explanation for the observed effects in SCT (0.007). Additionally, because the transition occurs in the quantum regime, the characteristic energies of this system are small, making them very sensitive to external fields, as observed.

*Gerhard Mercator University; Duisburg, Germany

Contact: Eugene L. Venturini, Nanostructures and Device Sciences Department, 1122
    Phone: (505) 844-7055, Fax: (505) 844-4045, E-mail: elventu@sandia.gov
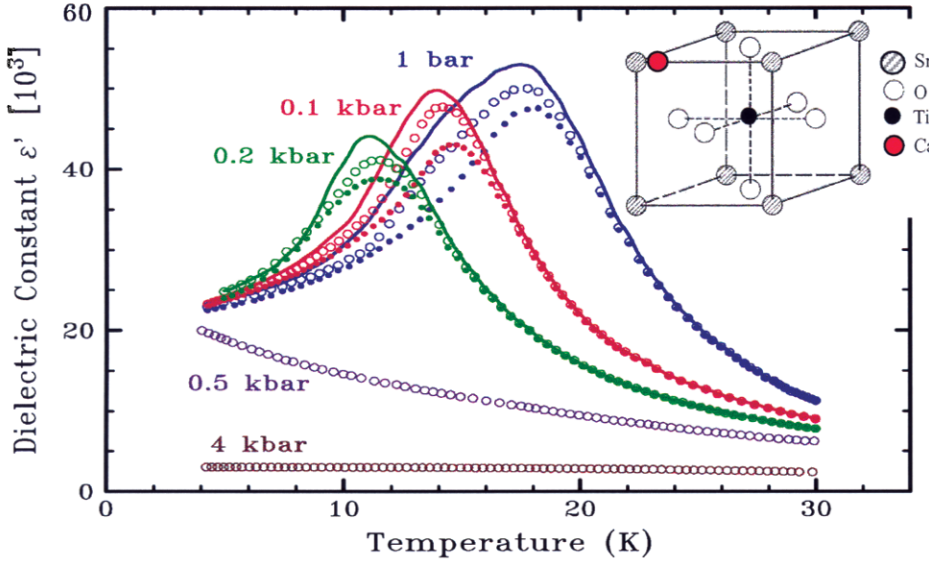
Figure 1. Influence of pressure on the dielectric response of SCT (0.007). The frequency dispersion is the signature of a relaxor state ($- = 10^3$, o = 10^4, and o = 10^5 Hz). The transition and dispersion are suppressed for pressures above 0.5 kbar. The inset shows the off-center position of the Ca^{2+} ion.

Figure 2. Temperature dependence of the correlation length (r_c), for dipolar interactions in SCT (0.007) at 1 bar and elevated pressures. The strong suppression of r_c with pressure is responsible for the vanishing of the relaxor state. The ordinate is approximately in units of nanometers.
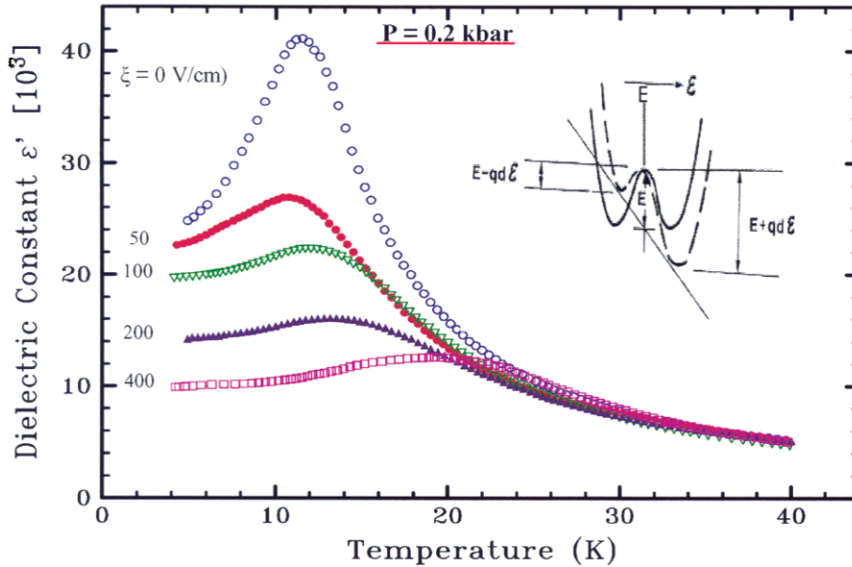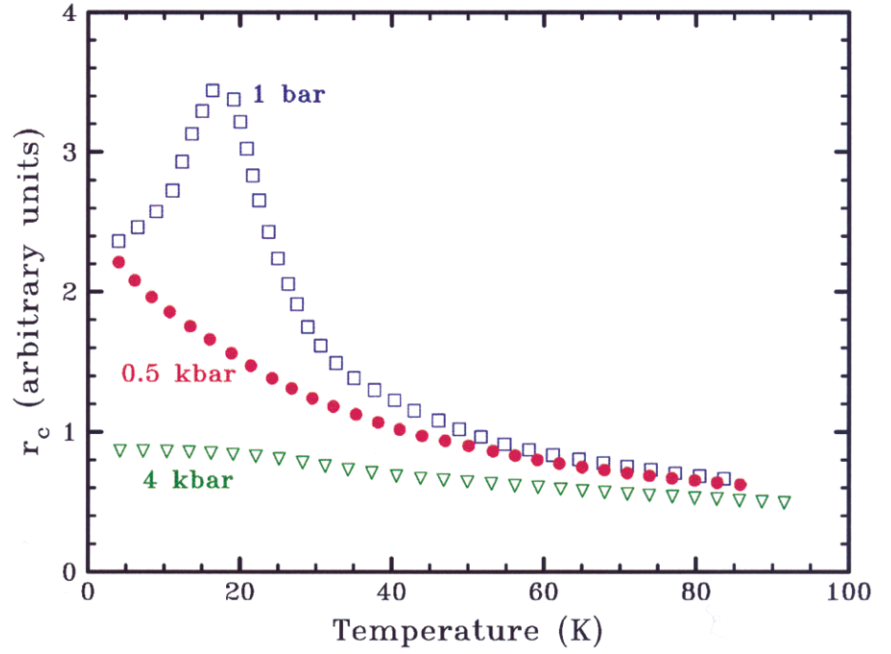
Figure 3. Very modest biasing fields have a very strong influence on the dielectric response of SCT (0.007) in the quantum regime. The inset shows the influence of bias on the potential for dipolar reorientation.

Surfaces and Interfaces

Atomistic Simulation of Capillary Evaporation of Confined Water

by K. Leung, A. Luzar, and D. Bratko

Motivation—The interaction of water with material surfaces is critical to understanding biology, corrosion, water transport in nano-channels, adhesion, and wetting of MEMS components. Water is unique in that it supports large surface tension and contact angles θ. $\theta > 90^o$ means "hydrophobic," i.e., the surface in question repels water. A dramatic manifestation of hydrophobicity is the water-vapor phase transition in water trapped between two hydrophobic surfaces below a critical distance $D_c \sim 0.1\mu m$. This evaporation or boiling occurs under ambient conditions. Experimentally, hydrophobic probe cylinders/tips of surface force apparatus (SFA), atomic force microscopes (AFM), and Sandia's interfacial force microscopes (IFM) often measure forces at distances *less* than D_c *on approach*; after bringing the surfaces into contact and pulling them apart, evaporation *is* observed. This suggests liquid water can be metastable between two such surfaces; there must be a considerable free energy barrier against this transition. Our work seeks to compute this free energy barrier which has eluded experimental measurements.

Accomplishment—We use atomistic force fields to examine the evaporation dynamics. We directly compute the free energy barrier and the dynamical prefactor. Together they yield an absolute rate of evaporation at a specific inter-surface distance D. For small enough distances, we can also directly simulate confined metastable water and measure the mean time that elapses before evaporation occurs. The two estimates are then compared. We also look at the effect of dissolved atmospheric gas molecules.

Without going into details, we stress that (a) the Grand Canonical Monte Carlo technique must be used to allow the number of water molecules in the system to change, because the free energy barrier is associated with a local decreased water density (in effect a "vapor tube"); (b) molecular dynamics calculations, initiated at the top of the free energy barrier, are used to yield the dynamical prefactor; (c) a method for measuring the size of the vapor tube is adapted from our previous work [K. Leung and A. Luzar, J. Chem. Phys. 113:5845 (2000)] and is incorporated into both (a) and (b).

Figure 1 shows that the free energy barrier is ~ 19 k_BT for D = 1.4nm and ~ 14.5 k_BT for D = 1.25nm. The absolute rates of vapor tube formation are 1.2×10^6 and 8×10^8 per nm^2 for these Ds. The predicted rate for D = 1.25nm is verified with direct molecular dynamics evaporation runs. Using a scaling argument to extrapolate to large Ds, we find that, within experimental time scale, one expects to observe evaporation at roughly D < 2nm; otherwise the water remains metastable as the probe surfaces approach each other. We further find that dissolved nitrogen gas molecules do not change this conclusion.

Significance—This work lays the foundation for studying more realistic water dynamics at surfaces, such as in the presence of surface defects or air bubbles. The predicted evaporation rate gives a guideline for experimental studies, particularly for the benefit of Sandia's advanced IFM technique which is capable of measuring forces down to small distances.
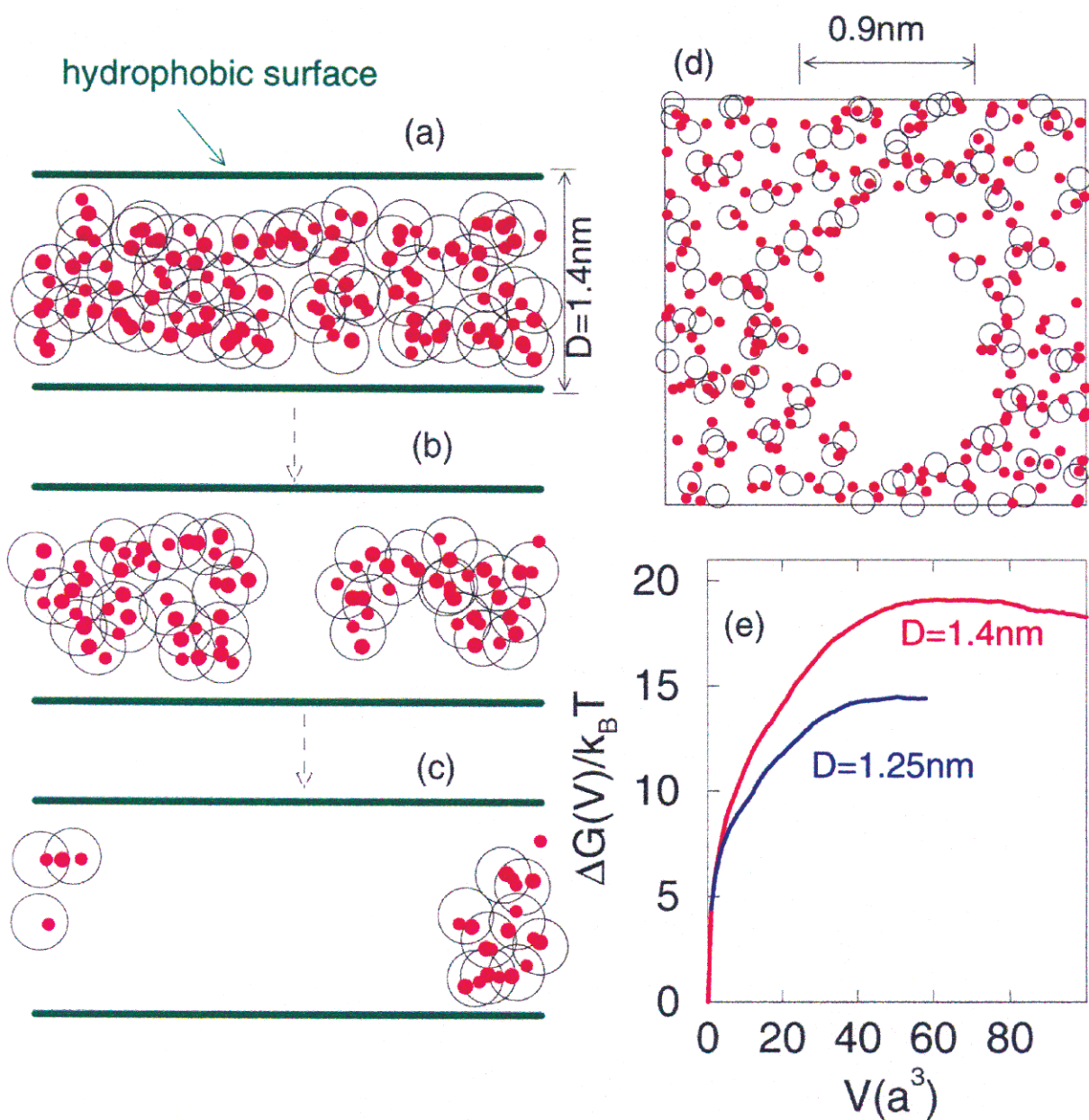
Figure 1. Panels (a)-(c): Schematic of confinement-induced evaporation pathway. Panel (b) is the transition state vapor tube, shown also in cross section parallel to confining surfaces in panel (d). Panel (e) depicts the computed free energy barrier for two intersurface separations.

The Wetting of Metal Surfaces

by Peter J. Feibelman

Motivation—Water-surface interactions govern aqueous heterogeneous chemistry, flow through nanopores, adhesion and brittle fracture in humid environments, a host of biological and geophysical phenomena, i.e., a virtually endless list of phenomena of both general scientific and Sandia interest. Yet, little is known in atomic detail about the arrangement and behavior of water molecules adjacent to solid surfaces. To see if modern first-principles electronic structure methods can help, a logical first step is to ask if they provide a reasonable interpretation of the only experimentally determined structure of a water layer immediately adjacent to a surface. This was a particularly interesting endeavor, because the published structure for heavy water on the close-packed crystal face of ruthenium ["Ru(0001)"], is unlike the expected "ice-like" adsorption layer, a fact unexplained since its publication in 1994.

Accomplishment—In a discovery with general implications, we have proven theoretically that intact water molecules bind too weakly to Ru(0001) to wet this surface, or, in other words, to form a two-dimensional layer on it. Intact water molecules should form ice-mounds on Ru(0001), not a wetting layer. Wetting requires that some of the adsorbed molecules dissociate.

Prior to the structural analysis for heavy water on Ru(0001), there was no reason to question the notion that the water molecules first deposited on the close-packed face of a precious metal crystal arrange intact in a "bilayer" (see Fig. 1) like those that stack to form the naturally occurring ice crystal ("ice-Ih,"). However, the O atoms of a water bilayer lie in two planes separated by 0.96 Å. The experimental structure had O atoms lying essentially in a single plane.

Initial calculations showed that arrangements of undissociated D_2O molecules do not optimize with nearly coplanar O atoms and also that they do not wet Ru(0001), because their heats of adsorption lie 0.15 to 0.20 eV below the binding energy of water in ice-Ih. We therefore worked backwards from the idea that near coplanarity stems from all the O atoms' being bound to the surface through similar mechanisms.

Asking why the upper water molecules of a bilayer do not approach the metal closely enough to form an O-Ru bond, we conjectured that it is because these molecules have an O-D bond oriented along the normal to the surface, which quenches the O atom's power to form bonds along this direction. If this O-D bond were broken, and the resulting free D atom were to re-bond directly to the metal (see Fig. 2) then the remaining OD fragment would move closer to the surface as it formed an O-Ru bond. *A b initio* calculations validated this reasoning, and showed that the dissociation and re-bonding was energetically profitable enough to explain the wetting of Ru(0001).

Significance—Successful interpretation of the water wetting layer on Ru(0001) suggests that current *ab initio* methods are up to the task of establishing the correct "boundary conditions" for simulations of water-mediated interactions with metals and, one hopes, with a diverse array of chemically and structurally different surfaces. This capability will enable science-based advances in nanofluidics, micromachine function, and corrosion prevention.

Figure 1. An ice-like "bilayer" adsorbed on the hexagonal surface of a ruthenium crystal. Ru atoms are represented by yellow spheres, O atoms by pink ones and H or D atoms by cyan.

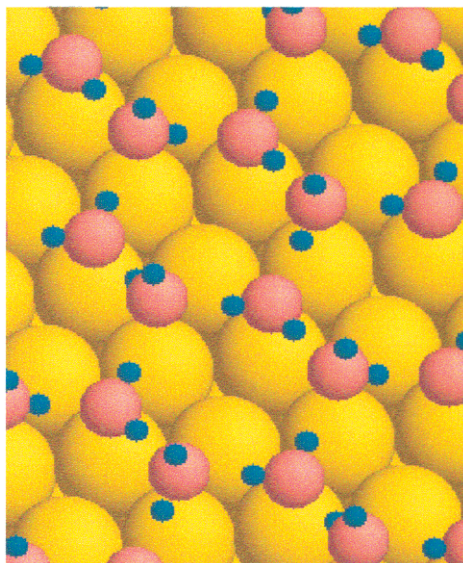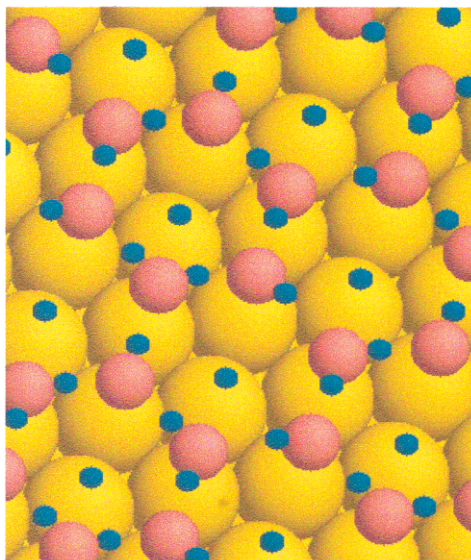**Figure 2**. A half-dissociated wetting layer on the hexagonal surface of a ruthenium crystal. D atoms (cyan) dissociated from half the heavy water molecules are bonded directly to the metal (yellow spheres).

Friction Between Self-Assembled Alkylsilane Monolayers

by M. Chandross, G . S. Grest, B. Park, M. J. Stevens, and E. B. Webb III

Motivation—Self-assembled monolayers (SAMs) offer a unique means to alter and control the chemical nature of surfaces. The alkylsilane SAMs are technologically interesting because they bond to oxide surfaces and are thus of use in silicon based micro-electromechanical systems (MEMS), which have a native oxide surface. While experimental measurements yield atomic scale force data, they do not provide the simultaneous structural information that can be deduced from molecular scale simulations. A predictive, molecular-level understanding of friction is the missing key to intelligently designing interfacial lubricants for MEMS.

Accomplishment—Molecular dynamics (MD) simulations are ideal for probing the properties of SAM coated surfaces, since they are able to produce both atomic scale force data as well as the underlying structural information. We have carried out extensive MD simulations of the adhesion and lubrication of SAM coated SiO_2 surfaces. We have studied the effects of chain length, system size, and shear velocity between pairs of SAMs covalently bonded to crystalline and amorphous SiO_2 surfaces. Snapshots of ordered SAMs before and after compression are shown in Fig. 1 for alkylsilane chains containing $n = 8$ backbone carbons. As the SAM surfaces are brought into contact, there is a small region of attraction due to the van der Waals interaction, with a magnitude of about 150MPa for all chain lengths studied ($n = 6$ to 18). Further reduction in the distance between the substrate surfaces leads to increasing SAM compression, as the interactions become strongly repulsive. The relationship between load and distance between the surfaces is monotonically dependent on the chain length. Shorter chains are stiffer and have a larger repulsion compared to longer chains. As seen in Fig. 1b, the chains tilt in order to compress beyond the all *trans* contact configuration. Tilting allows the chains to accommodate smaller substrate separations without introducing large repulsive van der Waals interactions.

Lubrication between pairs of SAMs in contact is studied by shearing the two surfaces relative to each other. The velocities that can be studied in a MD simulation are within the range of MEMS devices, typically on the order of a few cm/s, but large compared to those scanned by typical force probes. For all chain lengths and shear velocities studied, the shear stress versus time for ordered SAMs shows stick-slip dynamics (Fig. 2). Stick-slip dynamics require commensurability of the two sliding surfaces, which ensures that the hills and valleys of the potential surfaces match in such a way that one SAM pushes against the hills of the other (stick) and then overcomes the barrier to quickly slide down (slip). A small percentage of defects break up the stick-slip dynamics for low loads but not for high loads. Simulations on a range of system sizes for $n = 6$ show that larger system sizes result only in decreased noise.

Significance—MD simulations provide new insight into the atomic scale motion of SAMs, providing a picture of the molecular structure under shear and a detailed molecular level understanding of energy dissipation mechanisms. Future work with functionalized end groups, including fluorocarbons, and the introduction of water, will lead to a quantitative understanding of adhesion and friction as a function of chemical interactions and environmental exposure.
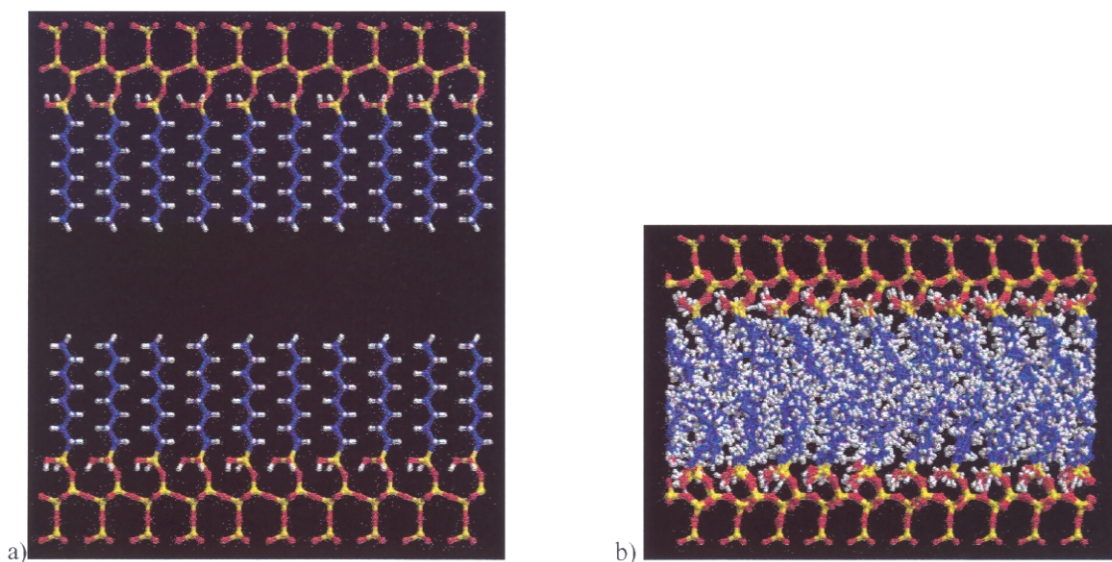
Figure 1. Snapshot of an $n = 8$ ordered alkylsilane SAM before (a) and after (b) compression. Silicon atoms are red, oxygen atoms are yellow, carbon atoms are cyan and hydrogen atoms are white.
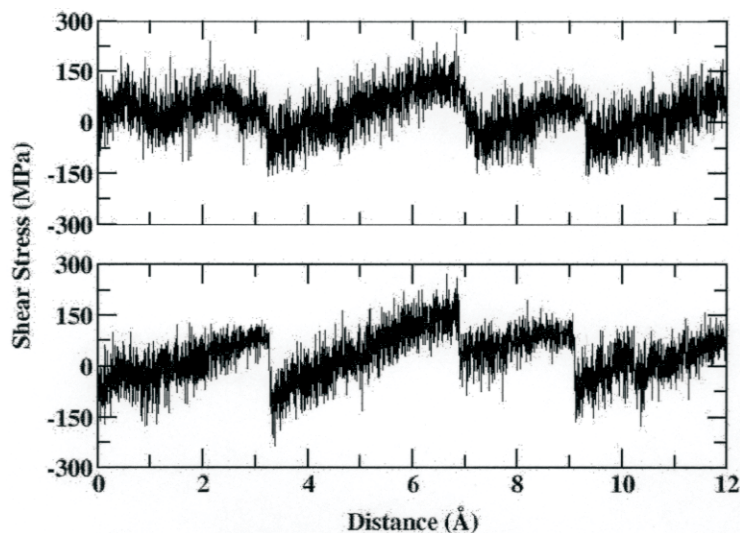
Figure 2. Shear stress ss as a function of distance sheared for $n = 12$ (top) and 18 (bottom) at a normal load of 0.2GPa and relative shear velocity $v = 0.2$ m/s. Results for 100 chains attached to each surface.

Biomimetic Materials and Biomaterials

Photocatalytic Growth of Photosynthetic Metal-Hybrid Nanoassemblies

by Yi Yang, Yujiang Song, C. Jeffery Brinker, John A. Shelnutt

Motivation—Photocatalytic processes in nature are efficient means for generating energy sources and controlled structures. A simple example is the generation of energy-rich sugar molecules through photosynthesis. The goal of this research is to understand and mimic such natural processes in order to create nanostructures for realizing novel phenomena and quantum control.

Accomplishment—As a first example of the use of this photocatalytic method for the creation of new nanostructures, we have grown spherical crystalline platinum-metal shells enclosing a micellar surfactant assembly containing a photocatalytic molecule. The Pt crystalline shell is porous and composed of 3-nm nanoparticles that are grown together to form a single crystal. The thickness of the spherical shell of Pt nanoparticles can be controlled by adjusting the photocatalyst-to-Pt ion concentration. For a single layer of Pt nanoparticles, the diameter of the nanoassembly is 12 nm (see Fig 1). At low photocatalyst/Pt ratios thick layers of the Pt nanoparticles are obtained giving nano-assemblies up to 100 nm in diameter.

The single-crystalline nature of these nanoassemblies is illustrated in Fig. 2. This structure makes them durable, even capable of surviving drying and re-suspension in water.

Platinum nanoparticles are a well known catalyst for water reduction We have demonstrated the activity of the platinized-micellar nanoassemblies in the photosynthesis of molecular hydrogen from water and a weak electron donor molecule. In this application, the photocatalytic tin porphyrin in the micelle is reduced by a weak electron donor which can be water itself. The reduced porphyrin is a strong reductant which gives its electron to the Pt nanoparticle shell at a potential negative enough to reduce water to hydrogen. An illustration of hydrogen generation in room light using the nanoassemblies alone and also in the presence of water-soluble tin porphyrin added to absorb more of the light is provided in the inset of Fig. 2.

We continue to improve and gain control over the synthesis of these platinum nanoassemblies. For example, we have found that the light intensity controls the size distribution of the nanoassemblies, with intense tungsten light giving the most uniform size.

Significance—The photocatalytic approach has been demonstrated with other metals and semiconductors including Ag, Au, Cu, Hg, U, and Se, and it is probably applicable to other metals and semiconductors. It has also been used to form metal alloy nanostructures at room temperature. The use of light to grow the nanostructures means that lithographic methods can be used to control the location at which the nanostructures are grown. The photocatalytic method shows promise for the controlled synthesis of a wide variety of nanostructures and hybrid nanoassemblies for catalysis, sensing, biomedical and other applications.
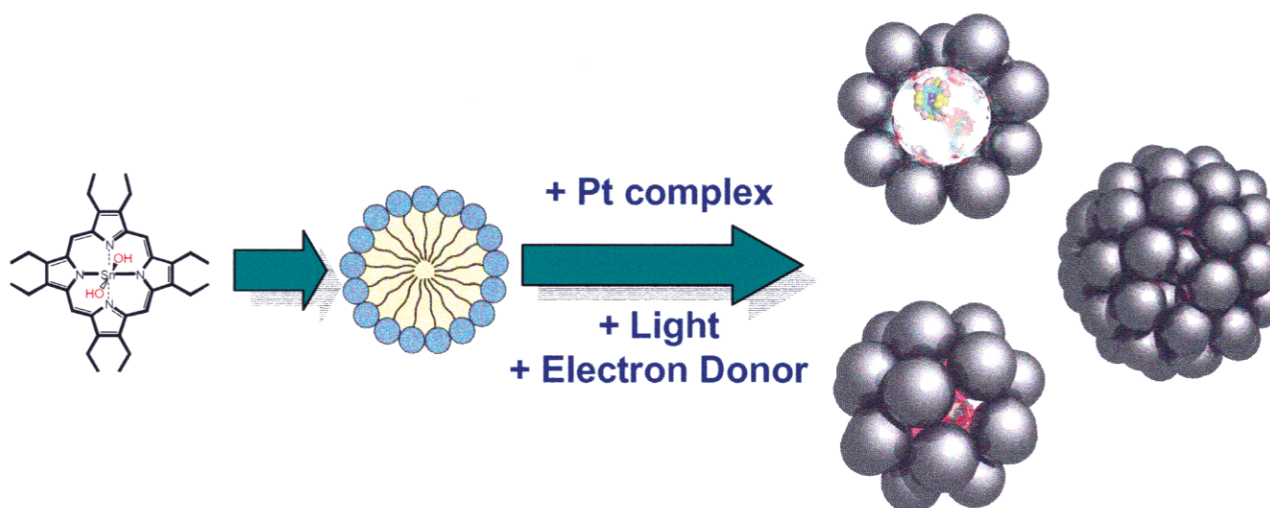
Figure 1. Synthesis of photocatalytic nanoreactor assemblies. Porphyrin photocatalyst inside the surfactant micelle reduces metal ions to form 3-nm crystalline Pt nanoparticles on the surface of a micelle. The photocatalyst remains active after the synthesis, and the Pt nanocrystals are catalytic.
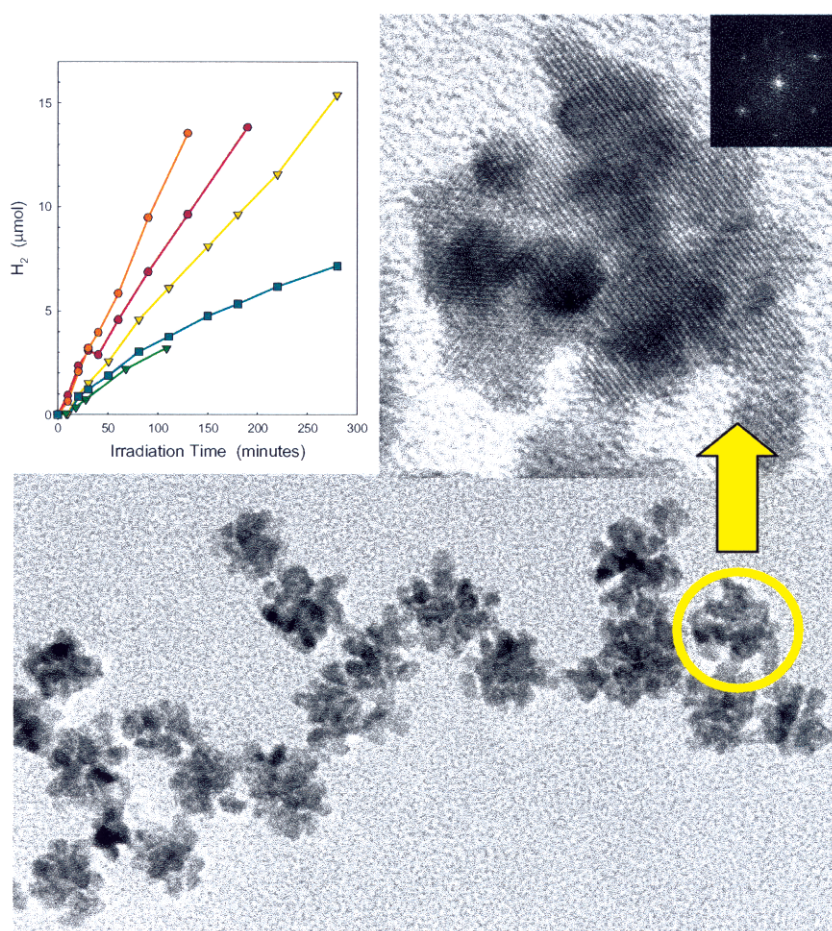
Figure 2. TEM images of the photocatalytic platinized-micellar nano-assemblies showing they are porous single crystals. The nanoassemblies photosynthesize H_2 from water. The graph shows the molecular hydrogen produced by Pt nanoassemblies as a function of time for various solution conditions, e.g., added Sn porphyrin to harvest light, different electron donor concentrations.

Self-Assembly of Extended and Oriented Nanostructures

by Zhenrong R. Tian, James A. Voigt, and Jun Liu

Motivation—Nanostructured materials have great potential for microelectronic and microfluidic devices, but many applications depend on patterning, alignment and ordering of the materials from nano to macro-length scales. Although nanostructured powders and continuous films have been widely investigated, the preparation of extended and oriented nanostructures that are useful for device applications remains a scientific and technological challenge. Our objective is to develop a generalized approach to assemble extended and oriented nanostructures based on Sandia's strength in chemical synthesis and self-assembly, and to integrate these materials with microelectronic and microfluidic systems that are relevant to DOE's mission at Sandia.

Accomplishment—We have devised a general, solution-based approach to build large self-assembled nanostructures with control of crystal size, orientation, and morphology over many length scales. Such self-assembled hierarchical ordering is Nature's way of building functional biomaterials (like seashells and diatoms) but is mostly absent in synthetic materials. The key to our new approach is a detailed understanding of a narrow region of the phase diagram, which allows control of the nucleation and growth events during the self-assembly process, and also the role of the crystalline surface chemistry, so that only desired shapes are produced. Large arrays of oriented ZnO nanorods (Fig. 1a), oriented conductive polymer nanowires (Fig. 1b), and helical ZnO nanocolumns and nanotubes (Figs. 1c and 1d) have been prepared. The morphologies of these oriented nanostructures can be predicted and systematically controlled. In addition, we have developed a self-assembly approach to build large oriented structures step-by-step. Super crystals and open structures preserving the shape and orientation of the basic structural units, or primary crystals, can then be constructed through controlled crystal stacking by repeated nucleation and growth, as shown in Fig. 2. Figure 2a is a TEM image of the self-assembled nanoporous materials. Figure 2b illustrates how we can use the octahedral crystals as the fundamental building blocks to build large structures step-by-step. Figure 2c is a SEM image of the octahedral crystals, and Figs. 2d and 2d are the secondary and high order crystals derived from the stacking of the primary crystals. Such hierarchical structures can also be patterned for microdevices (Fig. 2f).

Significance—The rich biomaterial-like morphologies and systematic control of the crystal orientation and alignment over many length scales demonstrate how phase-diagram information, coupled with self-assembly processes, can be used to produce hierarchically-ordered, synthetic crystalline materials. The new structures are based on a fundamental crystalline unit and the tailoring of the crystalline surface chemistry, and may allow rational control and prediction of the crystal morphology of ever-more-complex materials. Because the uniform crystals can also be patterned on a flat substrate, similar synthetic routes may be appropriate for the production of ordered arrays for device applications. Finally, the new solution method is scalable for large-scale production applications. The usefulness of the new materials has already been demonstrated in chemical and biosensors.
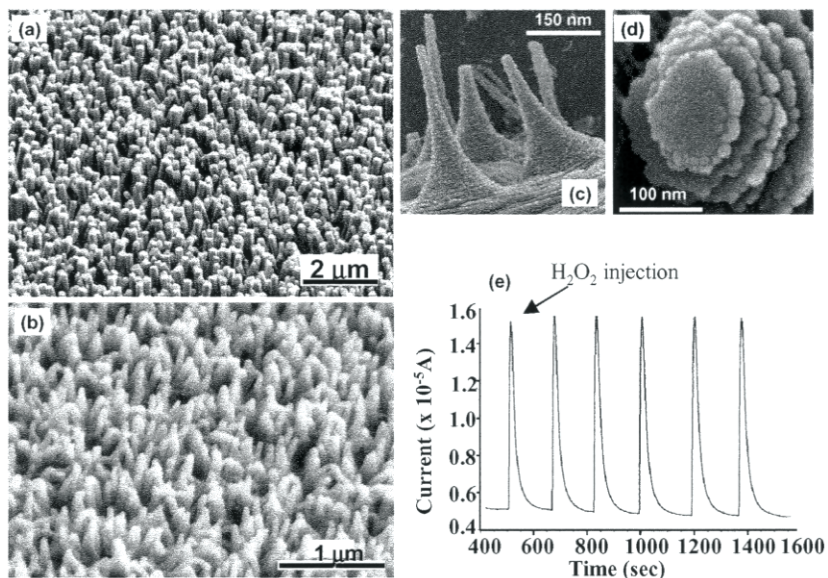
Figure 1. Self-assembled nanorod and nanowire structures and their application. (a) ZnO nanorods. (b) Conductive polymer nanowires. (c) Oriented helical ZnO nanorods. (d) Helical growth of ZnO crystals. (e) H_2O_2 sensing for glucose detection based on conductive polymer nanowires.
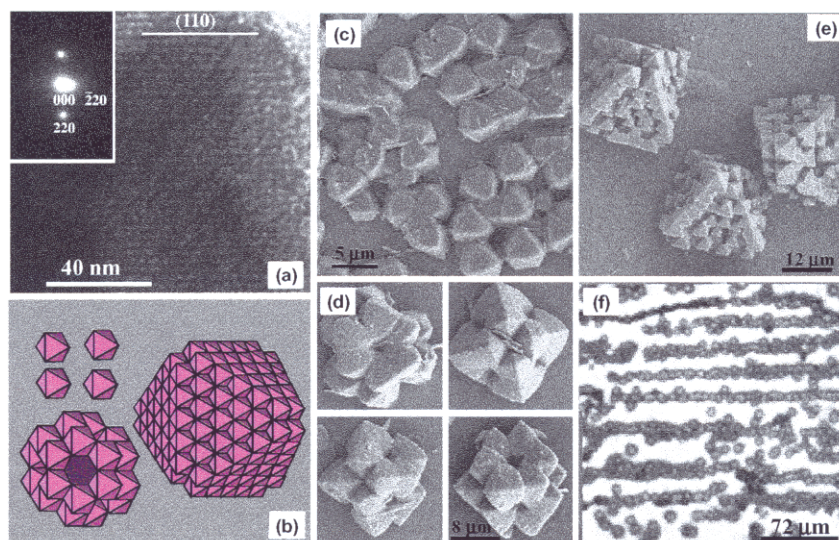
Figure 2. Step-by-step growth of large crystals. (a) TEM image of ordered self-assembled silicate crystals. (b) Schematics of crystal growth. (c) Growth of primary octahedral crystals. (d) Growth of secondary crystals. (e) Super crystal structures. (f) Aligned crystals on a patterned substrate.

Selective Adsorption of Proteins

by D. L. Huber, M. A. Samara, and B. C. Bunker

Motivation—We have extended our protein concentration capabilities to include the selective concentration of small proteins from a background of larger proteins. This is achieved through the use of a poly(N-isopropyl acrylamide) (polyNIPAM) monolayer whose surface properties are thermally switchable. Kinetics of protein adsorption onto this film (in its adsorbing state) are strongly dependent upon the size of the adsorbing protein. This is expected to be a powerful tool for collecting and concentrating small, dilute, biologically active proteins from a background of larger, more concentrated, relatively inert proteins.

Accomplishment—PolyNIPAM's ability to adsorb protein in its hydrophobic, high-temperature state has been known for a few years. However, it has been shown that bulk gels, or thick gel layers tend to adsorb proteins irreversibly. The ability to capture and release proteins efficiently rests upon the ability to synthesize defect-free polymer monolayers. This has been accomplished using a unique polymerization involving chain-transfer to a surface. To summarize the reaction: Radicals are generated in solution in the presence of NIPAM monomer and a surface bearing a self-assembled monolayer terminated with thiol groups. The radicals chain-transfer to the thiol groups where they initiate polymer chains that grow while remaining covalently bound to the surface. This reaction is capable of forming ultrathin (~ 4nm) films free of any defects that would irreversibly adsorb proteins. Proteins can be adsorbed by raising the temperature, and can then be quickly desorbed by simply lowering the temperature to below the transition at 35°C. Selectivity of protein adsorption is demonstrated by the UV-visible spectrum (Fig. 1) obtained on a hot polyNIPAM film in contact with a solution containing both albumin and myoglobin (5:1 by mass). The myoglobin forms a monolayer on the surface in about 30 seconds, however, in time (< 10 min) the larger albumin displaces the myoglobin to form a relatively pure albumin monolayer. By controlling contact times, small proteins can be adsorbed from a protein mixture then desorbed into a concentrated plug of purified low molecular weight protein (Fig. 2). While this may sound similar to other diffusion-dependent separation schemes, the kinetics of adsorption are too strongly size-dependent to be explained by differences in diffusion alone. Instead the kinetics are likely due to a combination of diffusion rates and sticking probabilities. This may allow one to increase the range of adsorption kinetics, and therefore increase the selectivity, through the careful control of temperature and pH to fine tune sticking probabilities.

Significance—Devices based on a selective, reversible protein trap could have widespread impact on the development of new miniaturized technologies to manipulate proteins and cells for biomedical applications. For example, use of several devices in series could provide a mechanism for extracting relatively dilute cytokines (small, cell-signaling proteins) from albumin-rich serum. Rapid concentration and analysis of these markers of immune response could provide powerful, nearly real-time information about the health and well-being of an organism or population of organisms. A device of this type would require years to develop, but could clearly have medical, anti-terrorism and military applications.

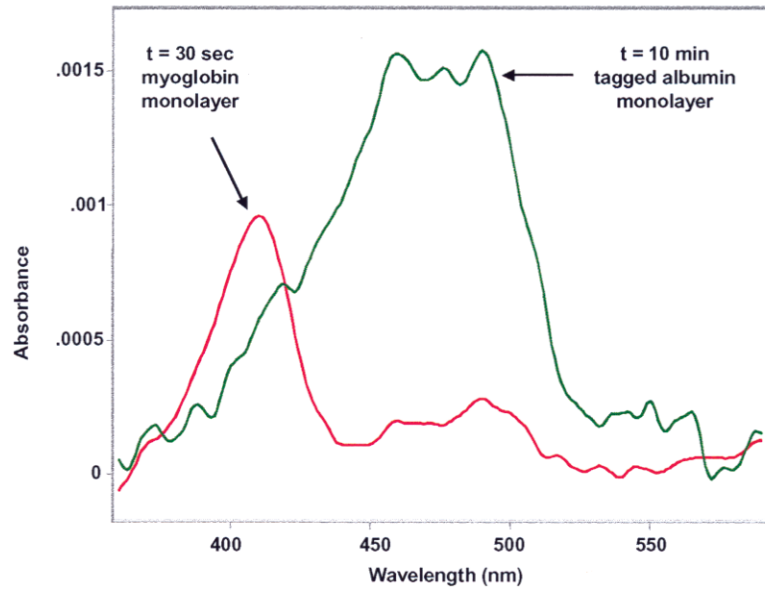**Figure 1**. A myoglobin monolayer forms on short-term exposure to a protein mixture, while the larger albumin (fluorescein labeled) displaces the myoglobin film after longer (10 min) exposure.
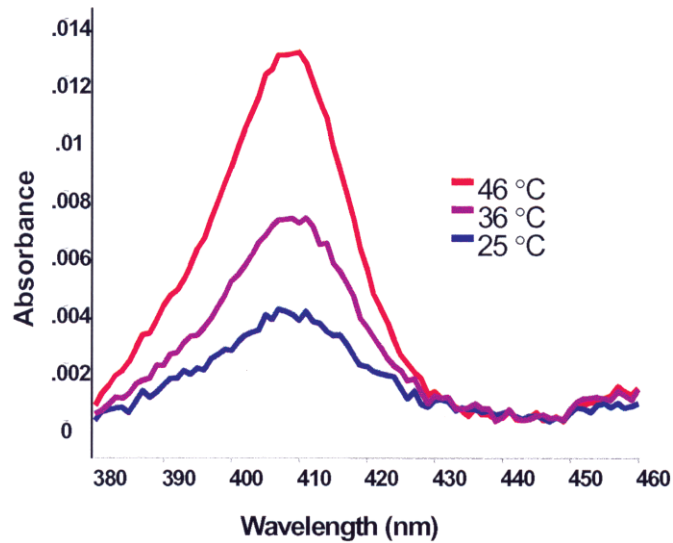

Figure 2. Desorption of a myoglobin monolayer monitored through UV-vis spectroscopy during slow cooling of a static solution (non-zero absorbance of the 25° sample is due to myoglobin dissolved in the solution).

Engineering Active Biomolecules for Use in Dynamic and Adaptive Materials

by G. D. Bachand, S. B. Rivera, B. C. Bunker, C. M. Matzke, and V. Vogel*

Motivation—The formation and nature of living materials are fundamentally different from those of synthetic materials. Synthetic materials generally have static structures and are not capable of adapting to changing environmental conditions or stimuli. In contrast, living systems utilize energy to assemble, reconfigure, and dismantle materials in a dynamic, highly non-equilibrium fashion. The overall goal of this work is to identify and learn how to exploit key strategies used by living systems to develop new types of materials whose assembly, configuration, and disassembly can be programmed or "self-regulated" in artificial environments.

Accomplishment—Our initial approach is to extract and engineer relevant, active biological molecules for integration and survival in synthetic microsystems. As a starting point, our focus has been on the enzyme kinesin (Fig. 1A), which belongs to a general class of proteins known as motor proteins. In living systems, kinesin is responsible for transporting molecular cargo along protein fibers called microtubules. Directional translation of kinesin along microtubules is rapid (e.g., ~ 1 µm/sec), and does not rely on concentration gradients, thus breaking the limitations associated with diffusion. The DNA coding sequence for kinesin was isolated from the thermophilic fungus *Thermomyces lanuginosus* (Fig. 1B) using reverse transcription and the polymerase chain reaction (RT-PCR). The DNA sequence was then cloned into a bacterial expression system, (Fig. 1C) to provide a source of thermally robust kinesin motor protein for integrating with microsystems. The kinesin coding sequence also was genetically engineered to introduce a 10x Histidine tag to the carboxylic acid terminus, which will efficiently bind to nickel chelate resins. The recombinant kinesin

motor protein was expressed in the Tuner (DE3) pLacI strain of *Escherichia coli*, and purified using Ni-NTA chelate liquid chromatography (Fig. 1D). The biochemical and biophysical properties of the kinesin are currently being characterized.

We also are collaborating with Professor Viola Vogel at the University of Washington to explore the use of microfluidic systems to guide the transport of molecular shuttles (i.e., kinesin and microtubules) at synthetic interfaces. Experiments have been performed using an inverted motility assay where microtubules are transported by kinesin motors that have been tethered to silicon surfaces. We patterned microfluidic channels on silicon wafers using photolithography, and demonstrated the efficacy of these channels to guide microtubule transport (Fig. 2). Work currently is focused on implementing chemical selectivity of the surfaces with lithographically defined patterns to localize kinesin motors to the bottom of the microfluidic channels.

Significance—The ability to actively transport cargo in nanoscale synthetic environments opens the door to mimicking the strategies that living systems use to assemble, reconfigure, and dismantle materials. A critical first step is to engineer relevant biomolecules that can function and survive in artificial environments. The thermostable kinesin enzyme that we have isolated possesses the necessary characteristics, and has been engineered to meet these criteria. Moreover, the ability to guide the transport of microtubules in a microfluidic system represents a fundamental concept that may be used to guide molecular transport at the nanoscale.

Figure 1. (A) X-ray crystallographic structure of a kinesin motor protein. (B) A culture of the thermophilic fungus *Thermomyces lanuginosus* was used to isolate and clone the DNA coding sequence (C) and subsequently express recombinant kinesin motor proteins (D).
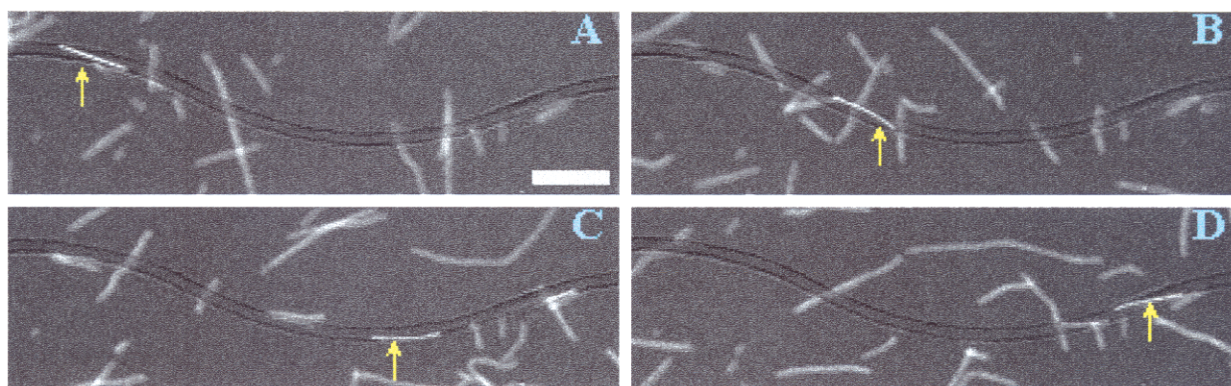
Figure 2. Image sequence of a microtubule being transported by tethered kinesin motor proteins, and guided by the physical confinement within a 1 μm wide x 1 μm deep microfluidic channel formed in SU8 on a silicon substrate (Scale bar = 5 μm).

Molecular-Scale Studies of Membrane Proteins

by A. Burns, K. Evans, J. Fleming, B. Swartzentruber, and J. Schoeniger

Motivation—With the emergence of biotechnology as a major new thrust at Sandia, it has become imperative that we develop the tools to analyze biomolecular processes at the molecular level. Insights into the mechanisms of important biomolecular processes will enable us to design better bio-sensors and to integrate biomolecular function into microsystems. As the interface between the cellular and external environments, membranes and membrane proteins are critical components of biological function. The 2-D nature of membranes makes them accessible to advanced biophysical techniques and offers excellent opportunities to study the relationship between structure and function.

Accomplishment—Using the technique of atomic force microscopy (AFM), we have been able to successfully obtain high resolution images of proteins that are imbedded in membranes. As shown in Fig. 1, we have resolved to within ±10 Å the highly ordered crystalline-like array of bacteriorhodopsin proteins in the lipid membrane of the photosynthetic *Halobacterium salinarium*. Trimers of these proteins form pores in the membrane through which pass H^+ ions. Upon exposure to light, the pores open and pump the protons out of the cell to form a concentration gradient that is later used to phosphorylate adenosine diphosphate, the ubiquitous currency of chemical energy in biosystems.

In addition to imaging, AFM can be used to manipulate individual molecules. We have been able to position the AFM probe over a membrane protein and bond to it under a slightly heavier load that that used for imaging. The protein can then be pulled out of the membrane, unraveling the folds that determine its structure. The forces involved in protein folding and packing in the membrane can then be correlated with other structural data.

The activity of single membrane protein pores can be characterized in real time by monitoring pA ion currents through the pores when the membrane forms part of an electrophysiological cell (Fig. 2). We have been able to establish stable pores created by the self-assembly of heptamers of the bacterial protein α-hemolysin. The pore is large enough (25 Å diameter) to allow the translocation of large biomolecules from one side of the membrane to the other. We detect these individual events by observing blockages in the ion current. So far we have been able to detect the translocation of signal stranded DNA molecules and show that the blockages correlate with the DNA oligimer length. In future studies we plan to work with pores that open and close with pH or voltage modulation.

Significance—We have shown that biomolecular structure and function can be examined at the single molecule level by using biophysical methods. As these methods become increasingly sophisticated we will continue to improve our understanding of membranes and membrane proteins. Outstanding problems that lie ahead include cell signaling and protein complexes in membranes. Furthermore we will be able to use these methods and insights to characterize and manipulate biomolecules or biomimetic systems that are integrated into microdevices.

AFM topograph

175×175 Å

Protein unfolding
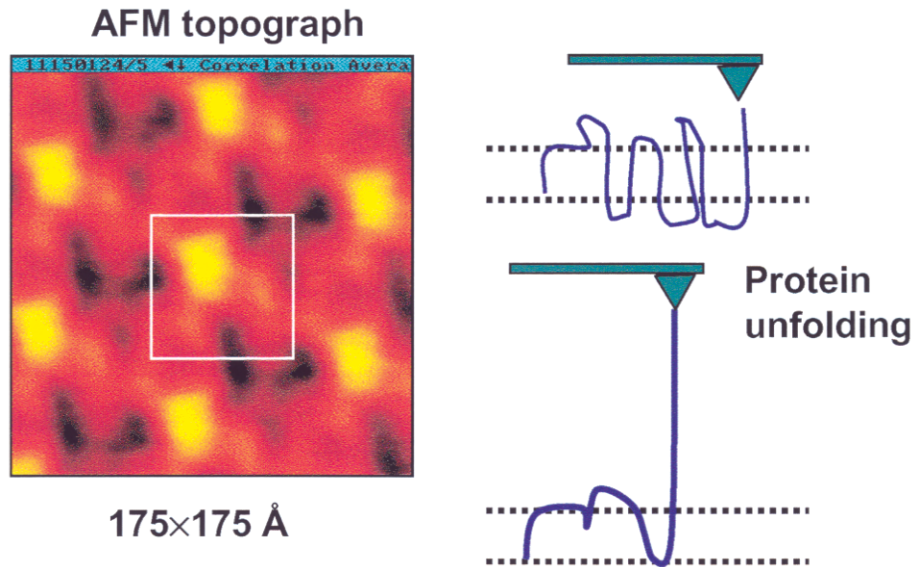
Figure 1. <u>Left</u>: Atomic force microscope (AFM) image of ordered proteins in a bacterial membrane bound to mica. In the white box, one can discern a trimer of proteins that make up the membrane pore. <u>Right</u>: The AFM cantilever can be used to grab and unfold individual membrane proteins.

α-hemolysin, poly-dA$_{100}$ blockages

Translocation
$I_B < 0.3\ I_A$
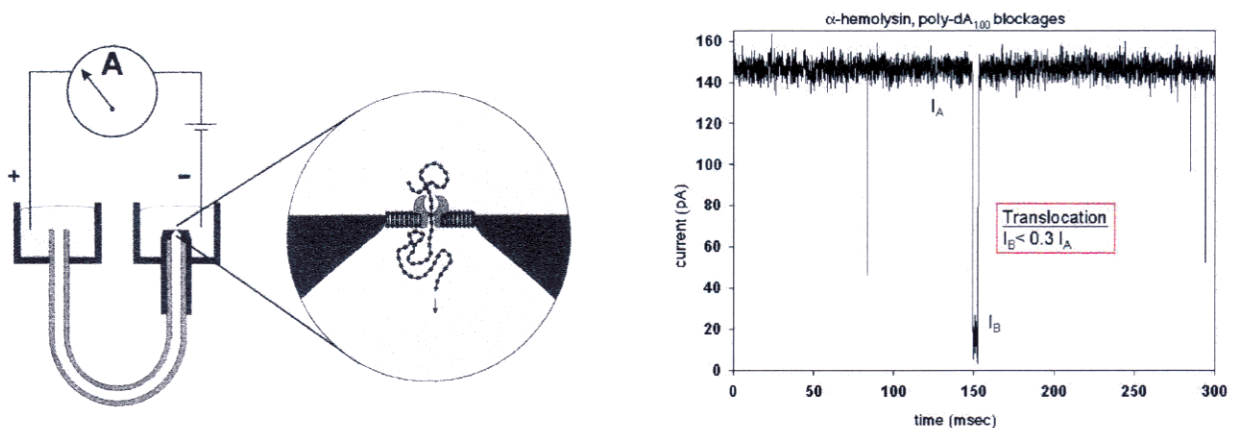
Figure 2. <u>Left</u>: Apparatus for detecting ion currents through protein pores imbedded in free-standing membranes. Also, a representation of blockage of the pore by the translocation of individual DNA molecules. <u>Right</u>: Actual ion current blockages by DNA translocation through a protein pore.

Complex and Collective Phenomena

Attractive Interactions Between Negatively Charged Plasma Crystal Particles

by G . A. Hebner, M. E. Riley and A. D. Boone

Motivation—Plasma crystals are a newly discovered phenomenon whereby particles in an electrical plasma self-assemble into orderly arrangements due to long range and collective interactions. Dusty plasmas occur everywhere from interstellar space to semiconductor processing reactors. Scientific interest is high not only because of astronomy and the semiconductor industry but also because the crystals are a macroscopic platform on which to test and develop theories of many physical phenomena related to collective interactions in many-body assemblies and long range particle interactions. Examples include wave propagation in ionic solids, phase transitions in Coulomb and shielded-Coulomb crystals, lattice stability dynamics of crystallization, charging mechanisms within plasmas, and the physics of the surrounding plasma and sheaths. For this program, we are combining experimental and theoretical studies to develop a mature understanding of the fundamental long-range interactions and multi-particle dynamic behavior within macroion crystals.

Accomplishment—We have developed new techniques to measure both the magnitude and shape of the attractive interaction between two negatively charged particles immersed in a charge neutral plasma. In previous work, we demonstrated that the dominant force between particles in a stable 2D planar plasma dust crystal is repulsive. For the case of 3D plasma crystals, additional forces appear to influence the crystal stability. We hypothesize that in 3D assemblies, the structure of the crystals is due to the delicate balance between repulsive Coulomb interactions and attractive forces produced by the motion of positively charged ions around the particles. Our calculations of ion flow past the particles, shown in Fig. 1, demonstrated the presence of a significant positive charge region below the particles. That positive space charge region provides the potential for an attractive force between the two negatively charged particles.

To characterize the attractive interaction, we developed a new technique to determine the forces present during very low energy head-on particle collisions. By manipulating the electric fields within the plasma using a parabolic, grooved electrode (Fig. 2), a well-defined potential trough is formed. A single particle injected into the trough collides with a second particle sitting stationary in the center of the well. The collision trajectories of the particles are quite complicated and show a number of previously unobserved interactions. An analysis of the particle trajectories as a function of time yields the time dependent forces on the particles. An example of the measured attractive potential and a fit to the functional form predicted by our first principles model is shown in Fig. 3. The force is on the order of 100 fN (femtonewtons), comparable to the forces applied by laser tweezers. While the magnitude of the attractive force is similar to the repulsive force, the shape is significantly different from a screened Coulomb repulsive potential.

Significance—Our measurements of the magnitude and shape of the attractive potential provide new information about the forces present in 3D, charged particle assemblies. When coupled with our first principles model, we now have critical tools to assess the stability of charged particle assemblies.
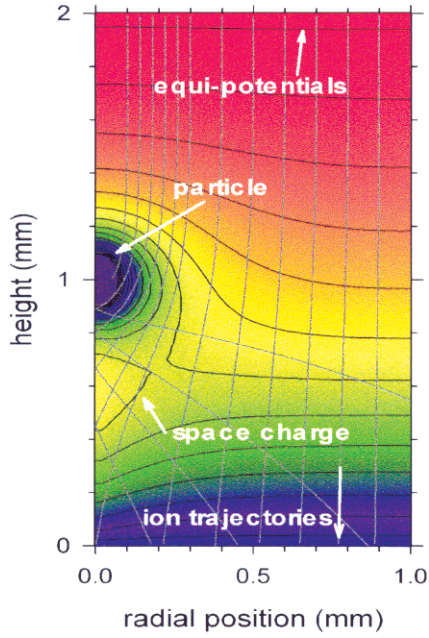
Figure 1. Self-consistent calculations of Argon ion trajectories flowing past a charged particle, top to bottom. The particle has a charge of 20,000 electrons and is suspended at the plasma's sheath boundary by a time average electric field of 16 V/cm. Dimensions are in millimeters. The ion bunching due to focusing produces a positive space charge region that is the source of the attractive interaction.
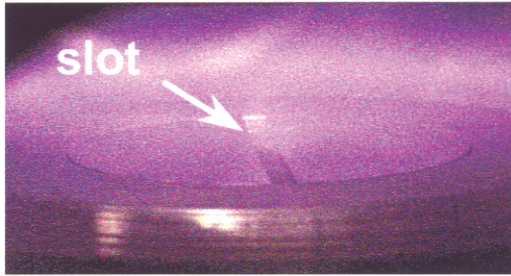
Figure 2. Side view of the lower electrode assembly and the Argon plasma glow. The arrow is pointing to the slot in the lower electrode that produces the electrostatic trough in which the particles collide.
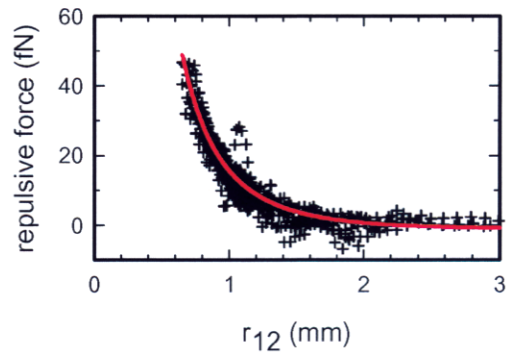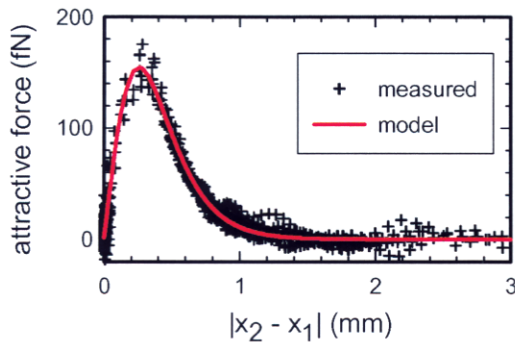
Figure 2. Measured attractive and repulsive particle interaction potentials. The solid line is fit to the data using a form predicted by our models.

Generating Strange Magnetic Interactions

by J. E. Martin, R. A. Anderson, and R. L. Williamson

Motivation—We have been developing field-structured magnetic particle/polymer composites to use as highly sensitive chemical sensors. The resistance of these materials can change by 10 orders of magnitude when exposed to chemical vapors that are absorbed by the polymeric phase, the resultant swelling evidently breaking ohmic particle contacts. Although the sensitivity of these sensors is promising, they have proven difficult to fabricate reproducibly. We decided that feedback might be useful to control the properties of these sensors within narrow bounds.

Accomplishment—In pursuing feedback control of sensor properties we have discovered a way to generate strange, *isotropic* magnetic interactions in particle suspensions that lead to a variety of particle structures unachievable by any other means, and enable us to make particle composites with highly optimized properties. To understand these interactions, recall that magnetic particles, such as iron filings, chain along magnetic field lines due to "positive" induced dipolar interactions. If such a magnetic field is rotated, the particle chains will also rotate unless the rotation frequency is so high that the chains can't keep up. In this case, the rotating dipole moments experience an average interaction that is exactly a "negative" dipole potential. This causes the particles to form sheet-like structures in the plane of the rotating field. What will happen if a particle suspension is simultaneously exposed to a rotating magnetic field *and* a constant field perpendicular to the rotating field plane (a *triaxial* field)? It is easily shown that the positive and negative effects

should cancel, leaving no interactions, an ideal situation for feedback control of structure. Experimental work has demonstrated that in reality a subtle magnetic interaction remains that draws the particles into complex foam-like structures.

Why do interactions remain in a balanced triaxial field? Triaxial interactions exhibit dominant many-body effects. Pairwise additivity of interactions, which leads to familiar phenomena such as molecules forming liquids and solids, phase transitions, et cetera, breaks down completely. Instead, particles can form stable molecular-like configurations, giving triaxial interactions some of the flavor of quantum chemistry. Experiments and simulations (Figs. 1 & 2) show the evolution of complex particle foam structures from random particle suspensions. All manner of complex triaxial fields can be created by modulating the phase between field components or the component amplitudes. These allow us to create remarkable collective particle dynamics that lead to a rich variety of composite structures.

Significance—Triaxial magnetic interactions enable the synthesis of novel particle composites with optimized and controllable magnetic, dielectric and transport properties. Numerous applications are possible, such as metal filter membrane formation, particle patterning, deflocculation, microfluidics stirring, and developing optimal resistance-based sensors. Scientific interest is also high, because these many-body interactions lead to a "foam" state of matter that is neither solid, liquid, nor gas.
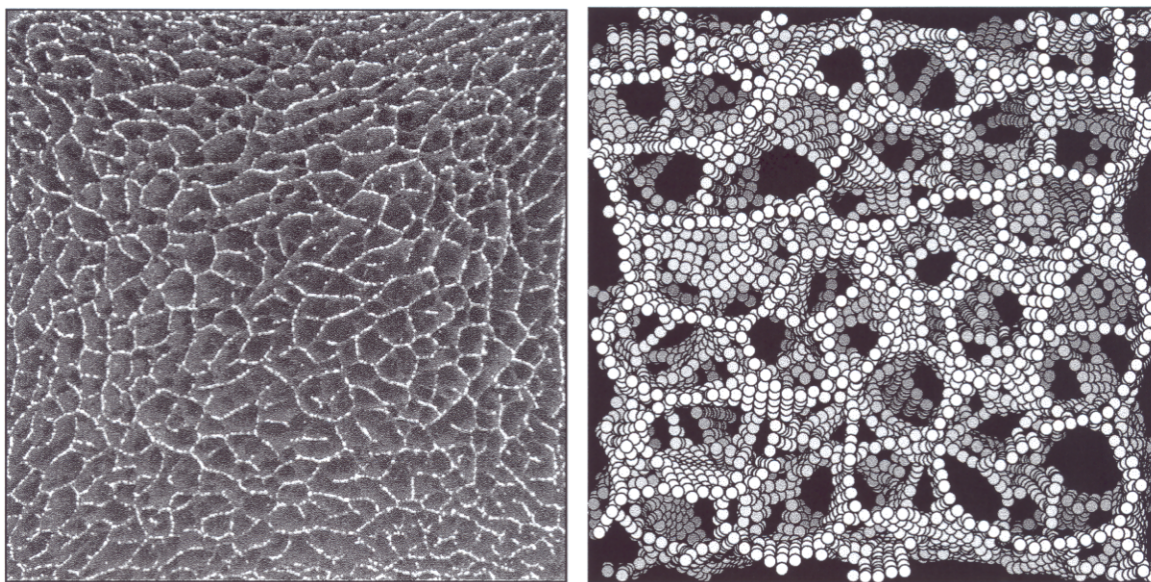
Figure 1. <u>Left</u>: A particle composite synthesized in a triaxial field during polymer gelation. The particles form roughly randomly oriented sheets. <u>Right</u>: Simulation.
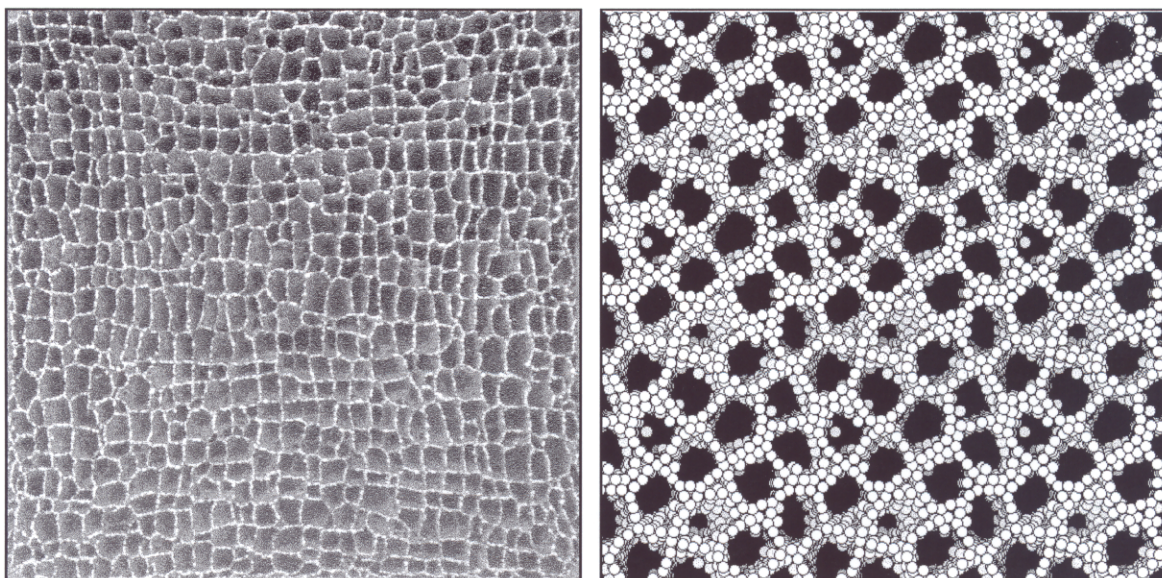
Figure 1. <u>Left</u>: A particle composite synthesized in a phase modulated triaxial field during polymer gelation. The particles form deep pores. <u>Right</u>: Simulation.

Recent Awards
and Prizes

Recent Awards and Prizes

National and International Awards

2002 — **Plasma Prize for Science and Technology** presented by the American Vacuum Society, Plasma Science and Technology Division, for innovative development of diagnostics and insightful fundamental studies of low temperature plasmas and their successful application to the advancement of plasma technologies. (Greg Hebner)

2000 — **IEEE Third Millennium Medal** for Outstanding Achievements and Contributions (Paul V. Dressendorfer)

    — **R&D 100 Award** for the Ion Electron Emission Microscope (IEEM) [Barney Doyle, George Vizkelethy, Robert Weller (Vanderbilt University), and Berthold Senftinger (Staib Instruments, Inc., in Germany)]

1999 — **American Chemical Society Earle B. Barnes Award** for outstanding leadership in chemical research management: "For visionary leadership in managing laboratory and inter-laboratory research in the National interest at the frontiers of materials science." (George A. Samara)

DOE Basic Energy Sciences, Material Science Awards

2002 — **BES "Chunky Bullet Shootout":** Winner for "Ultrasensitive Chemical Sensors for Counter Terrorism Applications (Jim Martin and Bob Anderson)

2000 — **DOE Energy@23 Award** (top 23 DOE innovations from 1977-2000 contributing to American consumers) for the Strained-Layer Semiconductor. (Gordon Osbourn)

    — **Energy 100 Awards** (top one hundred discoveries and innovations from the Department of Energy that have resulted in improvements for American consumers from 1977-2000) for the Biological Microcavity Laser. (Paul Gourley)

1999 — **BES "Chunky Bullet Shootout":** Winner for "Detecting Cancer Quickly and Accurately" (Paul Gourley, et al.)

Other Awards

2002 — **AAAS Fellow Appointment**: Elected Fellow of the American Association for the Advancement of Science (AAAS) for her "seminal research on growth and properties of magnetic, superconducting, and optical thin films and for leadership in the management of interdisciplinary research." (Julia Phillips)

— **APS Fellow Appointments**: Elected Fellows of the American Physical Society (APS) for:
  — contributions to the fundamental understanding of the gas-phase and surface chemical processes in the chemical vapor deposition of semiconductor materials. (Michael E. Coltrin)
  — outstanding contributions to the physics of tunneling in two dimensional electronic materials, including fractional quantum Hall and double quantum well systems. (Jerry A. Simmons, Jr.)
  — pioneering studies of atomic-scale, kinetic, and thermodynamic aspects of the morphology of Si surfaces and significant innovations in scanning tunneling microscopy. (Brian S. Swartzentruber)
— **Horizon Award** presented by the New Mexico Commission on the Status of Women and the U. S. Department of Labor Women's Bureau: The recipient of this award must be a New Mexico resident who has contributed significantly to the acceptance and advancement of women in Science, Math, Engineering, and Technology (SMET). (Julia Phillips)
— **Federal Laboratory Consortium (FLC) Excellence in Technology Transfer Award** for the development of instrumentation and software analysis to measure, *in situ*, thin film growth rates and wafer temperature during the fabrication of compound semiconductor optoelectronic device structures. (Bill Breiland)
— **Publication in "All Star" collection** of 25 significant and most cited articles that appeared in ECS journals since 1940: As part of its Centennial celebration, the Electrochemical Society (ECS) has published an "All Star" collection containing articles that are "representative of the leading role ECS has played in advancing the theory and practice of electrochemical and solid state science." Among the 25 All-Stars is the publication, "A Mathematical Model of the Coupled Fluid Mechanics and Chemical Kinetics in a Chemical Vapor Deposition Reactor" that was based on BES-supported research and which was published in ECS's Journal. (M. E. Coltrin, R. J. Kee, and J. A. Miller)
— **Sandia Fellow Appointment**: By distinguishing himself and Sandia through his technical innovations in several very important fields, among which are: (1) strained-layer technology, in which his contributions were fundamental in establishing Sandia's world-class compound semiconductor R&D program; (2) the application of biological vision and pattern recognition systems to computer-based sensor systems; and (3) collective intelligence and self-organizing systems. (Gordon Osbourn)
— **Weapon Award of Excellence**: The CY 2001 Weapons Award of Excellence winners included two teams at Sandia Laboratories led by Center 1100:
  — (1) **The Neutron Tube Production R&D Team** for applying scientific tools and methods to improve yield and reliability of Neutron Tubes. Scientific analysis of critical components in the sub-assembly stages saves tens of thousands of dollars for each faulty component identified. (Paul A. Miller, Team Lead, et al.)
  — (2) **The Photonic Driver Team** for developing a Photonic Driver capability for microscale shock wave physics research. The capability uses laser acceleration, or photonic driving, of small metal discs ("flyers") that can generate controlled, planar shock waves in test materials upon impact. Developed to achieve a significant reduction in experimental length and time scales, this new capability addresses both the high

per-experiment costs of current shock methods and the inability of these methods to characterize materials having very small dimensions, as will be needed as technology moves more and more into the micro and nanoscales. (Bob Setchell, Team Lead, et al.)

2001 — **The Lockheed Martin NOVA Award**: The annual NOVA Awards honor 50 Lockheed/Martin individuals/teams "who have made outstanding contributions to Mission Success." A Sandia/industry team has developed the first 1.3-micron electrically pumped vertical cavity surface emitting laser (VCSEL) grown on a GaAs substrate using InGaAsN as the active material for ultra-high bandwidth datacomm and integration with silicon microsystems. [1.3-Micron Vertical Cavity Surface Emitting Laser (VCSEL) Team: John Klem, Andy Allerman, Kent Choquette, et al.]

2000 — **APS Fellow Appointment**: Elected Fellow of the American Physical Society (APS) for the invention of numerous Micro-Ion Beam Analysis techniques and their innovative application to solid state physics, fusion energy, materials science and radiation effects of semiconductors. (Barney Doyle)

1999 — **AAAS Fellow Appointment**: Elected to the rank of AAAS Fellow by the American Association for the Advancement of Science for his "national leadership in materials science and for pioneering contributions to ion beam analysis and modification of materials". Researchers are "elevated to this rank because of their efforts toward advancing science or fostering applications that are deemed scientifically or socially distinguished". (Tom Picraux)

Patents Awarded

2002
— **Patent 6,304,675**
Title: A New Cluster Analysis Method
Originators: Gordon C. Osbourn, Org.1001; Rubel F Martinez, Org.1118
— **Patent 6,393,038**
Title: Frequency-doubled Vertical External Cavity Surface Emitting Laser
Originators: William J. Alford, Org. 1118; Mary H. Crawford, Org.1123; Andrew A. Allerman, 1126; Thomas D. Raymond, 1118
— **Patent 6,375,759**
Title: Batch Fabrication of Precision Miniature Permanent Magnets
Originators: Terry J. Garino, Org. 1843; Eugene L. Venturini, 1122; Todd R. Christenson, Org.1743
— **Patent 6,391,393**
Title: Nonvolatile, Dual Level, Magnetic Storage Media
Originators: James E. Martin, Org. 1122; Chris P. Tigges, Org. 1742; Robert A. Anderson, Org. 1843; Eugene L. Venturini. Org. 1122

— **Patent 6,368,775**
Title: 3-D Photo-Patterning of Refractive Index Structures in Photosensitive Thin Films
Originators: Barrett G. Potter, Jr., Org. 1846; Kelly Simmons Potter, Org. 1118
— **Patent 6,406,931**
Title: Conductivity Control of GaN Using LT AIN Buffer Layers
Originators: Jeffrey J. Figiel, Org. 1126; Jung Han
— **Patent 6,365,428**
Title: Buried Distributed Bragg Reflector for Planar Waveguide Applications
Originators: Walter J. Zubrzycki, and Gregory A. Vawter, Org. 1742; Andrew A. Allerman, Org. 1126

2001
— **Patent 6,258,615**
Title: Multiple Wavelength Vertical Cavity Resonance Devices Fabricated by Selective Area Epitaxy in MOVPE
Originators: Michael E. Coltrin, Org. 1126; Hong Q. Hou and Kent D. Choquette, Org. 1742
— **Patent 6,187,592**
Title: Method for Determining Hemoglobin Concentration in Individual Red Blood Cells
Originator: Paul L. Gourley, Org. 1140
— **Patent 6,245,200**
Title: Visible Light Photooxidation of Toxic Organic Chemicals Using Nanoscale MoS2
Originator: Jess P. Wilcoxon, Org. 1122
— **Patent 6,252,287**
Title: Heterojunction InGaAsN Solar Cells
Originators: Steven R. Kurtz, Org. 1123; Eric Daniel Jones, Org. 1741; Andrew A. Allerman, Org. 1126; John F. Klem, Org. 1742
— **Patent 6,194,769**
Title: Sensor Devices Based on Field-structured Composites
Originators: Robert C. Hughes, Org. 1744; James E. Martin, Org. 1122; Robert A. Anderson, Org. 1846
— **Patent 6,248,992**
Title: Tailored Doping Profile for Photoconductive Semiconductor Switch
Originators: Guillermo M. Loubriel, Darwin James Brown, Fred J. Zutavern, Wesley D. Helgeson, Martin W. O'Malley, and Gary J. Denison, Org. 15333; Charles T. Sullivan, Hong Q. Hou, and Albert G. Baca, Org. 1742; Thomas E. Zipperian, Org. 1740; Andrew A. Allerman, Org. 1126; Harold P. Hjalmarson, Org. 9235
— **Patent 6,290,868**
Title: Field-structured Chemical Sensor
Originators: Robert C. Hughes, Org. 1744; James E. Martin, Org. 1122; Robert A. Anderson, Org. 1846

2000

— **Patent 6,147,793**

Title: Short-Cavity, Pulsed Optical Parametric Oscillators

Originators: Arlee V. Smith and William J. Alford, Org. 1118

— **Patent 6,110,390**

Title: A Double Electron Layer Tunneling Transistor (DELTT)

Originators: Timothy J. Drummond, Org. 5911; Marc E. Sherwin, Org. 1322; Jerry A. Simmons, Org. 1123

— **Patent 6,035,246**

Title: Chemical Recognition Software

Originators: John S. Wagner, Org. 15311; Gary Carmen Tisone, Org. 15334; Philip J. Hargis, Jr., Org. 1118

— **Patent 6,048,546**

Title: Lipid Bilayer Entrapment in Sol-gel Materials

Originators: Douglas A. Loy, Org. 6245; Darryl Y. Sasaki, Org. 1140; Stacey A. Yamanaka, Org. 1812

— **Patent 6,103,305**

Title: Zero Stress Amorphous Diamond

Originators: Thomas A. Friedmann and John P. Sullivan, Org. 1112

— **Patent 6,057,377**

Title: Molecular Receptors in Functionalized Sol-gel Materials Generated through Molecular Imprinting

Originators: Carol S. Ashley and C. Jeffrey Brinker, Org. 1841; Darryl Y. Sasaki, Org. 1140

— **Patent 6,022,748**

Title: Immobilization of Colorimetric Liposomes into Sol-gel Matrices for Direct Colormetric Detection

Originators: Darryl Y. Sasaki, Org. 1140; Stacey A. Yamanaka, Org. 1812

— **Patent 6,085,581**

Title: 3 Dimensional 2 Location Positioner with Reverse Referencing

Originators: Gary D. Jones, Org. 1812; Jack E. Houston, Org. 1114; Kenneth T. Gillen, Org. 1811

— **Patent 6,071,109**

Title: The Preparation of AllnSb by Metal-Organic Chemical Vapor Deposition

Originators: Kevin C. Baucom and Robert M. Biefeld, Org. 1126; Andrew A. Allerman, Org. 1126

— **Patent 6,117,369**

Title: Improved Molecular Optical Switch Based on Nickel Porphyrins

Originator: John A. Shelnutt

— **Patent 6,083,360**

Title: Use of Supplemental Heating for Deposition Tooling Shields

Originators: John A. Hunter, Org. 1114; Diane E. Peebles, James A. Ohlhausen, and Kenneth Hall Eckelmeyer, Org. 1822

1999

— Patent 5,965,271 (Continuation patent based on Patent 5,736,245)
Title: Chemical Treatment for Silica Containing Glass Surfaces
Originators: William L. Smith and Alexis Grabbe, Org. 1114; Terry A. Michalske, Org. 1140

— Patent 5,995,529
Title: Mid-infrared, InGaAsSb-based LEDs and Lasers with Semi-metal Electron Injection
Originators: Steven R. Kurtz, Org. 1742; Robert M. Biefeld and Andrew A. Allerman, Org. 1126

— Patent 5,858,559
Title: Method for Altering the Luminescence of a Semiconductor
Originators: Duane Dimos, Org. 1831; J. Charles Barbour, Org. 1111

— Patent 5,864,381
Title: Automated Pupil Remapping with Binary Optics
Originator: Dan Neal, Org. 1128

— Patent 5,901,247
Title: A New Cluster Analysis Method
Originators: Gordon Osbourn and R. Martinez, Jr., Org. 1155

— Patent 5,902,636 (Divisional of Patent 5,736,245)
Title: Method for Chemical Surface Modification of Fumed Silica Particles
Originators: A. Grabbe and W. L. Smith, Org. 1114; T. Michalske, Org. 1115

— Patent 5,926,773
Title: Chemical Recognition Software
Originator: J. Wagner, Org. 15334

— Patent 5,912,738
Title: Wafer Curvature Measurement Using Parallel Laser Beams
Originators: E. Chason and J. Floro, Org. 1112; C. Seager, Org. 1111; M. Sinclair, Org. 1812

— Patent 5,939,716
Title: A Three-dimensional Light Trap for Reflective Particles
Originator: Daniel R. Neal, Org. 1128

— Patent 5,936,739
Title: Frequency-converting Short-pulse Image Intensifier Based on Optical Parametric Amplification for the Detection of Phase
Originators: Mark W. Kimmel and Daniel R. Neal, Org. 1128; David E. Bliss, Org. 15333; Stewart M. Cameron, Org. 15336

— Patent 5,936,720
Title: Amplitude & Phase Beam Characterization Using a Two-dimensional Wavefront Sensor
Originators: William J. Alford, Org. 1118; Daniel R. Neal, Org. 1128; James K. Gruetzner, Org. 15333

Government Advisory Boards and Professional Societies/International Committees/Journals

Government Advisory Boards

Argonne National Laboratory
— Materials Science Division External Review Committtee; Julia Phillips, member; 1995-2000

National Research Council
— National Materials Advisory Board; Julia Phillips, Chair; 2002-2004
— Board on Astronomy and Physics; Julia Phillips, member; 2000-2003
— U. S. Liaison Committee for the International Union of Pure and Applied Physics; Julia Phillips, member; 2000-2002
— Committee on Materials Research for the Defense-After-Next; Julia Phillips, member; 1999-2002
— National Materials Advisory Board; Julia Phillips, member; 1999-2001
— Solid State Sciences Committee; Julia Phillips, Vice Chairman; 1998-2001

National Science Foundation
— Advisory Committee, Mathematics and Physical Sciences Directorate; Julia Phillips, member; 2000-2003

Professional Societies/International Committees/Journals

American Association for the Advancement of Science
— Council; Julia Phillips, member; 2003-2005
— Physics Section Nominating Committee; Julia Phillips, member; 2003-2005

American Association for Crystal Growth
— 15th American Conference on Crystal Growth and Epitaxy; Bob Biefeld, Co-chair; 2002

American Physical Society
— Maria Goeppert Mayer Award Committee; Julia Phillips, Chair; 2002
— Maria Goeppert Mayer Award Committee; Julia Phillips, member; 2001
— APS Division of Materials Physics (DMP) Executive Committee; Julia Phillips, Member at Large; 1997-2000

American Vacuum Society
— AVS Surface Science Division; Neal Shinn, Chair; 2001-2002
— AVS Surface Science Division; Neal Shinn, Program Chair; 2000

BES Materials Council
— Issues in Nanomechanics; Charles Barbour, Panel Chair; 2003

Institute of Electrical and Electronics Engineers
— IEEE Nuclear and Plasma Sciences Society (NPSS); Paul Dressendorfer, Editor-in-Chief; 2002-present

Professional Societies/International Committees/Journals (continued)

— IEEE NPSS Radiation Instrumentation Steering Committee; Paul Dressendorfer, member; 1997-present
— IEEE Nuclear and Plasma Science Society (NPSS) Administrative Committee; Paul Dressendorfer, member; 1993-present
— IEEE Transactions on Nuclear Science; Paul Dressendorfer, Editor; 1993-present
— IEEE NPSS Radiation Effects Steering Group (RESG); Paul Dressendorfer, member; 1988-present

International Union for Vacuum Science, Technique, and Applications (IUVSTA)
— IUVSTA Surface Science Electoral College; Neal Shinn, United States Representative; 2001-2004
— Surface Science Division; Neal Shinn, Secretary; 2001-2004
— Surface Science Program, 15th International Vacuum Congress; Neal Shinn, Chair; 2001

Ion Beam Modification of Materials Conference
— Charles Barbour, International Committee member; 1996-present

Materials Research Society
— MRS Board of Directors; Jerry Floro, member; 2002-2004
— MRS Task Force on Government Agencies Committee; Charles Barbour, member; 2002
— MRS Symposium: Sean Hearne, Organizer, Fall 2002; Tom Friedmann, Organizer, 2001; Eric Jones, Organizer, 2000; Materials Engineering for Solid-State Lighting Committee, Alan Wright, Co-organizer, Fall 2001
— MRS Membership Committee; Charles Barbour, Chairman; 2001-present
— MRS Meetings; Jerry Floro, Chair; 2001
— MRS Task Force 2020 Committee; Charles Barbour, member; 2000

Optical Society of America
— OSA-Committees for 2000 Awards; Arlee Smith, Max Born Award Member; 2000

Radiation Effects in Insulators Conference
— Charles Barbour, International Committee member; 1997-present

The Physical Review E
— Gary Grest, Senior Editor; 2002

The Minerals, Metals, and Materials Society (TMS)
— Electronic Materials Committee; Bob Biefeld, member; 2002

Professional Societies/International Committees/Journals (continued)

<u>Twelfth International Conference on Metal-Organic Vapour Phase Epitaxy</u>
— Bob Biefeld, Organizing Committee member; 2002

<u>US-Organometallic Vapor Phase Epitaxy Workshop</u>
— Bob Biefeld, Organizing Committee member; 2002

Resources and Capabilities

Resources and Capabilities
Physical and Chemical Sciences Center

— **Diagnostics and Characterization** —

Atomic-Level Imaging and Spectroscopy

We have developed technical capabilities in:

- Scanning Tunneling Microscopy (STM) with the ability to track the diffusion of single atoms on surfaces,
- Low Energy Electron Microscopy (LEEM) with nanometer spatial resolution and real-time spectroscopic imaging capability at sample temperatures from 300K to over 1000K,
- Field Ion Microscopy (FIM) with single atom resolution and accurate temperature control to 1 Kelvin,
- Atom Probe Microscopy (APM) with pulsed laser desorption capability,
- Interfacial Force Microscopy (IFM) with feedback for accurate, simultaneous normal and frictional force profile measurements for the quantitative study of adhesion, tribology, and nanomechanics, and
- Atomic force microscopy (AFM) for imaging, force profiling, and manipulation of individual biomolecules in fluid environments with simultaneous fluorescence detection.

Scanning Probe Metrology

We have developed a unique wide-field scanning Interfacial Force Microscope with calibrated force detection for the dynamic measurement of normal and lateral forces of micro-electrical-mechanical system components in operation.

Simultaneous Measurement of H, D, and T in Materials

We have designed and implemented a new ion beam analysis (IBA) system to simultaneously measure the absolute quantities of H, D, and T in materials using an elastic recoil detection (ERD) technique. The technique uses an E-dE detector arrangement, or particle telescope, to provide for accurate separation of the H, D, and T signals.

The system can also simultaneously acquire information about medium and high Z elements in the sample using Rutherford backscattering spectrometry (RBS). Measurement of other light elements is possible using the nuclear reaction analysis (NRA) technique, which is isotope specific. The system will have an accuracy of < 2% for measuring the composition of solids.

Ion Accelerator Nuclear Microprobe

We have facilities for nuclear microscopy and radiation effects microscopy based on a 6 MV tandem Van de Graaff ion accelerator. We generate ion species from hydrogen to gold for both radiation effects research and quantitative high-energy ion beam analysis of materials containing light elements (hydrogen to fluorine) using heavy ion elastic recoil detection (ERD) and heavy elements using high-energy backscattering spectrometry, and Heavy Ion Backscattering (HIBS). (Includes Patent #5,059,785 issued October, 1991.) An external Micro Ion Beam Analysis (X-MIBA) capability enables multi-elemental analysis and ion irradiation of samples, which are vacuum incompatible or extraordinarily large. The Sandia Nuclear Microprobe with micrometer size high-energy ion beams is used to study materials and devices. Special emphasis is given to the evaluation of the radiation hardness of microelectronic devices using three new advanced diagnostic techniques invented at Sandia: Single-Event-Upset Imaging, Ion-Beam-Induced-Charge-Collection Imaging (IBICC), and time-resolved IBICC. A recent development is the Ion Electron Emission Microscope (U. S. Patent No. 6,291,823 and 2001 R & D-100 Award winner), which can perform radiation microscopy using very highly ionizing particles without focusing the ion beam.

Materials Microcharacterization

Our capabilities in this area include optical microscopy, scanning, electron microscopy, analytical transmission electron microscopy, double crystal x-ray diffraction, ion beam analysis of materials (RBS, channeling, ERD, PIXE, NRA), Hall measurements, microcalorimetry, photoluminescence, light scattering, electronic transport, deep level spectroscopy, magnetization, and dielectric and magnetic susceptibilities.

Surface and Interface Spectroscopies

We maintain capabilities in Auger electron spectroscopy (AES), x-ray photoelectron spectroscopy (XPS), low energy electron diffraction (LEED), thermal desorption spectroscopy (TDS), and infrared reflectance-absorption spectroscopy (IRAS) for quantitative determination of materials structure and chemical composition.

Vision-Science Laboratory

The vision science laboratory consists of state-of-the-art hardware and software capabilities for carrying out video inspection, multi-spectral image analysis, and sensor-based pattern recognition. (Includes Imaging Processing System, Patent #5,495,536.) These capabilities are used in applications ranging from microsensor-based chemical detection and recognition to automated video/SEM inspection of semiconductor materials and circuits (Patent #5,901,247). This is a new approach to pattern recognition, coupling perception-oriented research with machine algorithms.

Chemical Vapor Deposition (CVD)

Our experimental tools for investigating CVD include optical probes (such as reflectance-difference spectroscopy and emissivity correcting pyrometry) for gas-phase and surface processes, a range of surface analytic techniques, molecular beam methods for gas/surface kinetics, and flow visualization techniques. These tools are integrated in a unique manner with research CVD reactors and with advanced chemistry and fluid models.

Growth Science Laboratory

Capabilities for in situ characterization of materials during thin film deposition, molecular beam epitaxial growth, and low energy ion beam simulated growth, include intensity profile sensitive reflection high energy electron diffraction (RHEED) for surface structure, energy dispersive x-ray reflectometry for in situ surface and interface structure, multibeam wafer curvature for strain (Patent #5,912,738), and Auger electron spectroscopy for surface composition.

KMAP X-ray Diffractometer

Based on double crystal x-ray diffractometry in combination with position sensitive x-ray detection, our KMAP x-ray diffraction analysis is used to determine the lattice constant, strain relaxation, composition, layer orientation, and mosaic spread for a large variety of advanced epitaxial semiconductor material systems.

Nanoelectronics Laboratory

We have the capabilities for fabrication of nanoscale quantum device structures, together with capabilities for ultra-low-noise measurement of transport from 0.3 Kelvin to ambient at high magnetic fields.

Lasers and Optics

We provide characterization and advanced understanding in the area of solid-state lasers and non-linear optics, especially as coherent sources of broadly tunable light in rugged, compact geometries. We also have established expertise in long-term and transient radiation effects characterization of optical materials. (Includes patented Wavefront Sensor Patent #5,493,391, and Monolithic Optical Amplification Devices Patent #5,463,649.) Capabilities include the widely used (approximately 2000 users worldwide) SNLO (Sandia

Non-Linear Optics) code, which is a lab-tested code for predicting the performance of non-linear optical components. In the area of integrated optical materials, our laboratories produce new types of photosensitive materials (processing patent applied for) for directly-writeable waveguides and reconfigurable optical interconnects.

Laser and Optical Spectroscopies

Our capabilities in characterizing semiconductor materials by photoluminescence and magnetoluminescence extend down to low temperatures by optical laser imaging and laser microscopy, by laser excitation spectroscopy, and by the time-resolved measurements of optical emission. We also have developed a high lateral resolution, near-field scanning optical microscopy (NSOM) capability with time and frequency resolution.

Low-Temperature Plasma Analysis

We have state-of-the-art capabilities for the analysis of low-temperature plasmas as found in commercial processing reactors. These include emission spectroscopy, electrical characterization, laser and microwave-based measurements of species concentrations, in situ electric field measurements, and others. Sandia is the only lab that combines new diagnostics, relevant process chemistries (complex mixtures), and massively parallel (MP) computer models for simulation of continuous and transient plasmas.

— **Synthesis and Processing** —

Synthetic Organic Laboratory

Novel lipids, surfactants, and other small molecules are prepared in this laboratory via synthetic organic techniques. The laboratory is also capable or forming and characterizing self-organized structures (e.g., liposomes, micelles, self-assembled monolayers, LB films) generated with the newly synthesized molecules in pure or mixed molecular systems.

Biomaterials Laboratory

The Biomaterials Laboratory possesses equipment to perform numerous molecular biology and biochemistry research including genomic DNA, RNA, and plasmid isolation from a variety of sources (e.g., bacteria, viruses, and eukaryotic tissues and ells). DNA sequences can be cloned into a variety of organisms, permitting the manipulation and modification of DNA and protein sequences, structure, and function. Cloned DNA sequences can be genetically engineered using reverse transcription, the polymerase chain reaction and site-directed mutagenesis. Native and recombinant proteins also can be expressed, purified, characterized, and functionalized in this laboratory.

Monolayer Deposition of Organic Films

We have a Langmuir-Blodgett facility for controlled deposition of mono- and multi-layer organic films. The facility includes two computer-controlled troughs, in situ fluorescence microscopy, vibration isolation, and a dust-free down flow work area.

Nanocluster Laboratory

We have developed and patented a process based on the use of inverse micelles for the synthesis of large quantities of monodisperse clusters of metals, semiconductors, and oxides.

Electron Cyclotron Resonance (ECR)

This plasma facility has been built for studying fundamental processes governing the growth of oxide and nitride dielectric films used in optoelectronics and used as hard coatings. This is the only system in the U.S., which combines ECR plus e-beam evaporation.

Molecular Beam Epitaxy (MBE)

We have research semiconductor growth laboratories for ultra-pure and ultra-flexible MBE growth of III-V materials. In addition, we have

research systems for Group IV semiconductor growth.

Metal-Organic Chemical Vapor Deposition (MOCVD)

We maintain research facilities with capabilities in MOCVD of III-V compound semiconductor materials including GaN-based materials and self-assembled quantum dots. These capabilities include research reactors designed specifically for studies of CVD chemistry, fluid dynamics, the development of advanced in situ diagnostics, and the development of advanced semiconductor heterostructures and devices.

Crystal and Thin Film Growth

Capabilities in this area include pulsed laser deposition chambers, a high vacuum metal deposition chamber, a thin film oxide deposition chamber, a diamond-like carbon deposition chamber, a hot filament chemical vapor deposition chamber, and various apparatus for single crystal growth. Our capabilities for stress relief of diamond-like carbon films and structures produced by pulsed laser deposition are not available elsewhere.

400 kV and 180 keV Ion Implanters

These systems are equipped with a variety of sources (gas, sputter, and metal vapor). This facility provides ion species from hydrogen to bismuth that can be used for studying fundamental irradiation mechanisms and selective chemical doping in semiconductors, metals, ferroelectrics, and superconductors.

High Pressure and Shock Wave Physics and Chemistry Laboratories

Our capabilities in this area include large volume static high pressure apparatus which can be operated at temperatures ranging from 2 to 700 K and in magnetic fields, as well as gas gun and explosive loading facilities with state-of-the-art, time-resolved diagnostics. Recovery fixtures have been developed for use with the gas gun and explosive shock loading facilities that allow unique material synthesis over broad ranges of shock pressures and temperatures. -art, time-resolved diagnostics. Recovery fixtures have been developed for use with the gas gun and explosive shock loading facilities that allow unique material synthesis over broad ranges of shock pressures and temperatures.

— **Theory and Simulation** —

Electronic Structure and Linear Scaling

We have developed state-of-the-art massively parallel electronic structure algorithms, based on *ab initio* pseudopotentials and plane-wave/Gaussian basis functions. These codes are used to develop a fundamental understanding of physical phenomena and materials, including compound semiconductor band structure, diffusion of point defects, dopants and impurities, optoelectronic properties of extended defects, adsorbate interactions on surfaces, bonding at metal-oxide interfaces, and enhanced reactivity of nanoparticles. To allow the investigation of more complex systems and phenomena, we have developed new computationally efficient algorithms, e.g., self-consistent linear scaling density functional theory and variable and real-space gridding.

Molecular Dynamics Simulation

Large scale, classical molecular dynamics simulations using the massively-parallel code LAMMPS (Large-scale Atomic/Molecular Massively Parallel Simulator) are being used to model a wide variety of systems. These classical simulations cover the length and time scale intermediate between quantum and continuum calculations. Systems of current interest include adhesion and friction in self-assembled monolayers, degradation of polymer adhesives, wetting and spreading of multi-component fluids and transport in polymer membranes for fuel cells. Modifications of the algorithm to include particle rotation and friction have been implemented to study granular materials.

Chemical Processes

We have extensive capabilities, including massively-parallel computation, to model complex chemically reacting flows such as occur in chemical vapor deposition manufacturing processes. Our numerical simulations can include the coupled gas-phase and gas-surface chemistry, fluid dynamics, heat, and mass transfer to provide predictive models of a chemical process.

Low-Temperature Plasmas

We have extensive capabilities in massively parallel codes to simulate the time and space evolution of low-temperature plasmas, focusing on new theoretical techniques for achieving rapid convergence and on direct comparisons with experimental results.
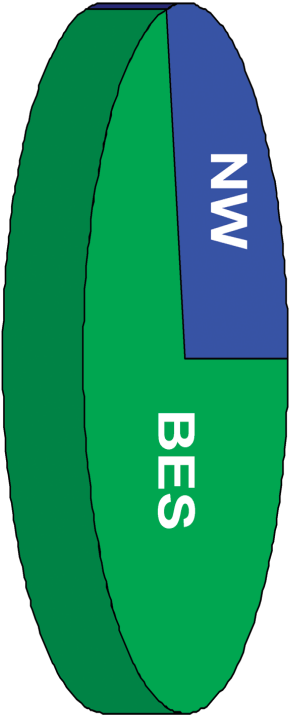
Optical and Wave Propagation

We have developed advanced simulation codes for understanding wave propagation in optical parametric oscillators and amplifiers for the purpose of designing highly efficient, tunable laser sources. We also have capabilities in novel optical designs, including resonators for compact laser geometries. These capabilities are coupled to in-house micro-optics construction facilities and state-of-the-art optics testing.

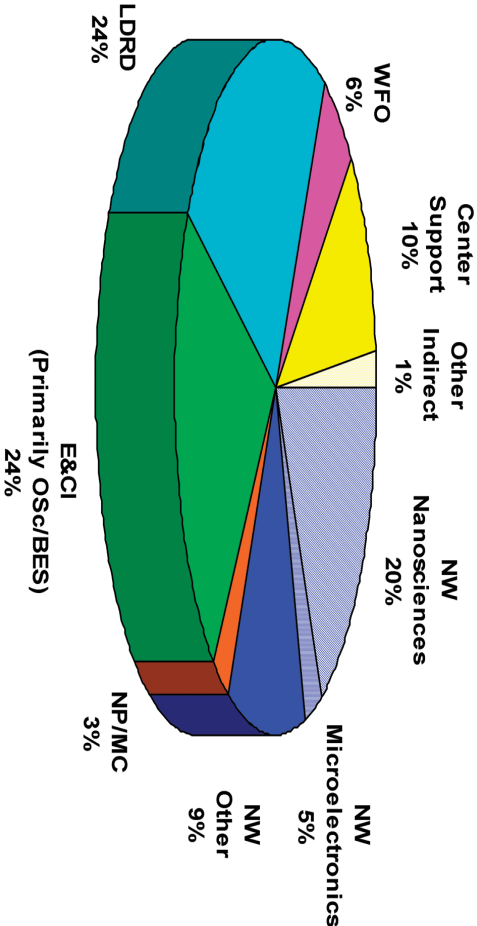# Physical and Chemical Sciences Center FY02 Budget - By Customer

Physical and Chemical Sciences Center
FY02 Budget - By Customer

Capital ($1M)

NW

BES

Operating ($35M)

LDRD
24%

WFO
6%

Center
Support
10%

Other
Indirect
1%

NW
Nanosciences
20%

NW
Microelectronics
5%

NW
Other
9%

NP/MC
3%

E&CI
(Primarily OSc/BES)
24%

| NW | Nuclear Weapons | NP/MC | Nonproliferation & Materials Control | E&CI | Energy & Critical Infrastructure | OSc | Office of Science |
| BES | Basic Energy Sciences | LDRD | Laboratory Directed Research & Development | WFO | Work for Others | | |

82